



# VCU

Virginia Commonwealth University  
VCU Scholars Compass

---

Theses and Dissertations

Graduate School


---

2021

## A Mechanism Behind the Mechanotransduction of Surface Characteristics in Osteoblasts

Otto J. Juhl IV  
*Virginia Commonwealth University*

Follow this and additional works at: <https://scholarscompass.vcu.edu/etd>

 Part of the [Biomaterials Commons](#), [Cell Biology Commons](#), [Molecular Biology Commons](#), and the [Molecular, Cellular, and Tissue Engineering Commons](#)

© Otto J. Juhl IV

---

Downloaded from

<https://scholarscompass.vcu.edu/etd/6643>

This Dissertation is brought to you for free and open access by the Graduate School at VCU Scholars Compass. It has been accepted for inclusion in Theses and Dissertations by an authorized administrator of VCU Scholars Compass. For more information, please contact [libcompass@vcu.edu](mailto:libcompass@vcu.edu).

# **A Mechanism Behind the Mechanotransduction of Surface Characteristics in Osteoblasts**

By

Otto John Juhl IV

A dissertation submitted in partial fulfillment of the requirements for the degree of  
Doctor of Philosophy in Biomedical Engineering at Virginia Commonwealth University.

Approved on by:

Advisor

Henry J. Donahue, Ph.D.

Alice T. and William H. Goodwin Jr. Professor and Distinguished Chair, Biomedical  
Engineering, College of Engineering

Virginia Commonwealth University  
Advisory Committee

<sup>1</sup>Christopher A. Lemmon, Ph.D.; <sup>1</sup>René Olivares-Navarrete, D.M.D., Ph.D.;

<sup>2</sup>Mohamed S. El-Shall, Ph.D.; <sup>3</sup>Robert W. Downs, M.D.

*<sup>1</sup>Department of Biomedical Engineering, VCU College of Engineering; <sup>2</sup>Department of  
Chemistry, VCU College of Humanities and Sciences; <sup>3</sup>Department of Internal Medicine,  
VCU School of Medicine*

© Otto J. Juhl IV 2021  
All Rights Reserved

## **Acknowledgments**

First, I would like to thank my advisor, Dr. Henry J. Donahue. I had the privilege of being Dr. Donahue's first graduate student here at VCU. This afforded me the opportunity to grow here at VCU with Dr. Donahue as we both learned the ins and outs of a new university. It is amazing how quickly these past five years have gone and how much has changed, but throughout all the change Dr. Donahue was steadfast. He could always be counted on to provide valuable insight and wisdom regarding research, school, and life as a whole. I would not be the researcher and man I am today without his guidance. Dr. Donahue could always be counted on to inject excitement and entertainment into any situation with a timely pun or some well needed advice. My favorite two examples were the following: The first is "No one cares how you feel", incredibly valuable advice in scientific research, and as I have learned as I have gotten older, in life as well. The second being "Dress for the job you want, not the job you have", as he wore one of his vibrant Hawaiian shirts and explained his desire to be the director of entertainment on a cruise ship once his scientific career concludes. I would also like to thank Dr. Donahue for providing me with and trusting me with so many opportunities here at VCU. Without his support I would not have been able to mentor so many exceptional undergraduates, pursue new opportunities at the Innovation Gateway, and be able to work on building the graduate program and community through BGSC. Dr. Donahue helped make our lab feel like a family, and is the reason we are, without a doubt, the BEST Lab at VCU. Moving forward from VCU will be challenging, but I am confident that the mentorship and guidance Dr. Donahue has given me will allow me to succeed regardless of my next steps.

Next, I would like to thank Dr. Yue Zhang. Dr. Zhang was always there to assist me when I had questions, my research was falling apart, or I just needed extra support. The positive attitude Dr. Zhang always had kept my spirit high and kept me pushing forward regardless of how the science was going. I learned so much from him. He taught me how to tackle tough questions, how to troubleshoot the various issues that arise, and how to mentor younger students and bring out their scientific skills. Dr. Zhang was an integral reason for my successes, and I am incredibly thankful for his guidance and mentorship.



I am incredibly thankful for my thesis committee. Dr. Rene Olivares-Navarrete who constantly challenged to think outside the box and stand firm in my beliefs. Whether it be class or research Dr. Olivares always pushed me to be inquisitive and question my current understanding of the science, allowing me to develop a confidence in myself that I was unaware I had. I will always be grateful for these lessons and his mentorship, despite his love for the Dallas Cowboys. Dr. Christopher Lemmon, who provided me a unique view on cell mechanotransduction. His unique perspective encouraged me to expand my viewpoint on my proposed mechanism. Dr. Lemmon also provided me with valuable insight into MATLAB, without which I would not have been able to complete my thesis. He also provided a lighthearted approach that made a fantastic mentor for scientific research. Dr. Mohamed Samy El-Shall, who provided a much-needed voice for the material science side of my thesis. The balance he injected into the cellular heavy focus of my thesis was greatly appreciated and reminded me to consider all aspects of my thesis. Lastly, Dr. Robert Downs, who provided a clinical insight and unique mechanistic views that were integral to the success of my research.

Finally, I would like to thank my family and friends. To all the friends I have made in Richmond, thank you for helping me understand my own research more clearly and for giving me a family to lean on when I needed it. To all of my friends scattered around the country, thank you for trekking to Richmond or letting me come visit when I needed a break. To my grandparents, Ralph and Margaret Juhl and Anthony and Maria Sauchelli, who always checked in on me and asked questions about my research and my life. You all provided me with a continual reminder of how far I have come. To my brother, Tyler, who was always a quick phone call away. He provided me with much-needed entertainment and a good laugh whenever I needed it the most. His passion and drive to succeed in all aspects of life is a trait I try to mimic myself and is a big reason I am where I am today. I cannot express enough my gratitude for everything he has helped me with in life. I consider myself one of the most privileged people in the world to be able to call him my brother. To my fiancée, Allison, who has supported me through all the ups and downs of my Ph.D., thank you. We have lived hours away for the past 5 years and she

took countless trips to Richmond to come visit, bringing with her a positive outlook on our futures that I could not have completed my work without. She has been instrumental in continually pushing me forward and helping to maintain my motivation, while also reminding me that I have to take small breaks and enjoy life now and again. I could not have done any of this without her and this degree is as much her achievement as it is mine. Lastly, I would also like to thank my parents, Otto and Lisa, who are my heroes, and two individuals that I continually look up to and aspire to be like every day. My dad has always stood by me and supported me in all of my pursuits in life, and as he will tell you I have him to thank for my intelligence. He also helped to foster my competitive spirit and dedication to my passions, something I learned from a young age watching him on a golf course and at home with our family. He taught me that failures will happen, it is being able to learn from those failures and move forward that lets you excel, a lesson that has helped me tremendously in my scientific career and in life. I am proud to share a name with such an inspirational man, and I could not be more thankful for everything he has done for me. My mom has been a constant pillar of support throughout my life. She is always there help me navigate challenges I have faced, whether it be editing a paper, moving to new cities, or making sure I knew how to cook something so I could bring some tastes of home to Richmond. I am similar to her in many ways, and for that reason I am always able to turn to her guidance regardless of the situation. She has instilled in me a strong work ethic and has shown me how to take pride in my work, both skills I have learned from watching her as she grew in her career and with our family. These skills have carried me so far, and I know I can continue to rely on them and her to carry me through all future challenges I will face. They have both supported me through so much, and for that I am forever grateful.

To everyone I mentioned or may have missed, my family, friends, lab-mates, mentees, and mentors, thank you for helping me during the stressful times and sharing my problems with me, the support system I have had over the past 5 years has been indispensable.

## Table of Contents

<b>ACKNOWLEDGMENTS .....</b>	<b>3</b>
<b>LIST OF SYMBOLS AND ABBREVIATIONS .....</b>	<b>8</b>
<b>THESIS ABSTRACT .....</b>	<b>10</b>
<b>CHAPTER 1. INTRODUCTION.....</b>	<b>11</b>
SPECIFIC AIMS .....	12
SIGNIFICANCE .....	16
<b>CHAPTER 2. BACKGROUND INFORMATION .....</b>	<b>18</b>
BONE OVERVIEW .....	19
THE OSTEOINTEGRATION PROCESS .....	20
BIOMATERIALS IN BONE REPAIR .....	22
CELL TRANSDUCTION OF SUBSTRATES.....	25
<b>CHAPTER 3. APTAMER-FUNCTIONALIZED FIBRIN HYDROGEL IMPROVES VASCULAR ENDOTHELIAL GROWTH FACTOR RELEASE KINETICS AND ENHANCES ANGIOGENESIS AND OSTEOGENESIS IN CRITICALLY SIZED CRANIAL DEFECTS.....</b>	<b>28</b>
ABSTRACT .....	29
INTRODUCTION .....	29
MATERIALS AND METHODS .....	31
RESULTS .....	39
DISCUSSION .....	45
CONCLUSION.....	49
<b>CHAPTER 4. EFFECT OF CARBONATED HYDROXYAPATITE SUBMICRON PARTICLE SIZE ON OSTEOBLASTIC DIFFERENTIATION.....</b>	<b>50</b>
ABSTRACT .....	51
INTRODUCTION .....	51
MATERIALS AND METHODS .....	54
RESULTS .....	62
DISCUSSION .....	69
CONCLUSION.....	71

<b>CHAPTER 5. HYDROXYAPATITE PARTICLE DENSITY REGULATES OSTEOLASTIC DIFFERENTIATION THROUGH B-CATENIN TRANSLOCATION .....</b>	<b>72</b>
ABSTRACT .....	73
INTRODUCTION .....	74
MATERIALS AND METHODS .....	78
RESULTS .....	89
DISCUSSION .....	98
CONCLUSION.....	106
<b>CHAPTER 6. INHIBITION OF FOCAL ADHESION TURNOVER PREVENTS OSTEOLASTIC DIFFERENTIATION THROUGH B-CATENIN MEDIATED TRANSDUCTION OF PRO-OSTEOGENIC SUBSTRATE.....</b>	<b>109</b>
ABSTRACT .....	110
INTRODUCTION .....	110
MATERIALS AND METHODS .....	113
RESULTS .....	118
DISCUSSION .....	129
CONCLUSION.....	135
<b>CHAPTER 7. CONCLUSIONS AND FUTURE PERSPECTIVES.....</b>	<b>136</b>
CONCLUSION.....	137
FUTURE PERSPECTIVES.....	139
<b>VITA .....</b>	<b>143</b>
<b>REFERNCES .....</b>	<b>144</b>
<b>APPENDIX .....</b>	<b>160</b>
SUPPLEMENTAL FIGURES .....	160

## List of Symbols and Abbreviations

4',6'-diamindino-2-phenylindole – **DAPI**  
Adenomatous polyposis coli – **APC**  
Ak strain transforming – **AKT**  
Alkaline phosphatase – **AP**\*enzymatic activity/**ALPL**\*gene/**ALPL**\*protein  
Aptamer-functionalized fibrin hydrogel loaded with 10/mL of vascular endothelial growth factor – **10AFH**  
Aptamer-functionalized fibrin hydrogel loaded with 2.5ug/mL of vascular endothelial growth factor – **2.5AFH**  
Aptamer-functionalized fibrin hydrogel(s) – **AFH**  
Atomic force microscopy – **AFM**  
Bone morphogenic protein-2 – **BMP2**  
Bone morphogenic protein-4 – **BMP4**  
Bone volume to total volume – **BV/TV**  
Carbonated hydroxyapatite – **CHA**  
Collagen1-a1 – **COL1A1**\*gene/**COL1A1**\*protein  
Deoxyribonucleic acid – **DNA**  
Dimethyl sulfoxide – **DMSO**  
Dulbecco's phosphate buffered saline – **DPBS**  
Dynamic light scattering – **DLS**  
Enzyme-linked immunosorbent assay – **ELISA**  
Extracellular matrix – **ECM**  
Fetal bovine serum – **FBS**  
Fibrin hydrogel loaded with 10ug/mL of vascular endothelial growth factor – **10FH**  
Fibrin hydrogel loaded with 2.5ug/mL of vascular endothelial growth factor – **2.5FH**  
Fibrin hydrogel(s) – **FH**  
Fibroblast growth factor – **FGF**  
Focal adhesion kinase – **FAK**  
Fourier transform infrared spectroscopy – **FTIR**  
Glyceraldehyde-3-phosphate dehydrogenase – **GAPDH**\*gene  
Glycogen synthase kinase-3 $\beta$  – **GSK-3 $\beta$**   
Green fluorescent protein positive – **GFP+**  
Human fetal pre-osteoblastic cell 1.19 – **hFOB 1.19**  
Human mesenchymal stem cell(s) – **hMSCs**  
Hydroxyapatite particle – **HAp**  
Lymphoid enhancer factor – **LEF**  
Microcomputer tomography – **microCT**  
Mammalian mechanistic target of rapamycin – **mTORC**  
N-hydroxy succinimide – **NHS**  
Neuropilin-1 – **NRP1**\*protein  
Non-hydrogel loaded control – **E**  
Osteocalcin – **BGLAP**\*gene/**OCN**\*protein  
Osteopontin – **OPN**\*protein  
Parathyroid hormone – **PTH**  
Phosphate buffered saline – **PBS**

Platelet rich plasma – **PRP**  
Poly(lactic-co-glycolic acid) – **PLGA**  
Polycaprolactone – **PCL**  
proline rich-tyrosine kinase 2 – **PYK2**  
Pro-osteogenic substrate – **POS**  
Quantitative real-time polymerase chain reaction – **qRT-PCR**  
Radioimmunoprecipitation assay buffer – **RIPA**  
Revolutions per minute – **RPM**  
Ribonucleic acid – **RNA**  
Runt related transcription factor-2 – **RUNX2\*gene/RUNX2\*protein**  
Scanning electron microscopy – **SEM**  
Semaphorin-3A – **SEMA3A\*protein**  
Sp7/Osterix – **SP7\*gene/OSX\*protein**  
Standard deviation – **SD**  
Standard error mean – **SEM**  
T-cell factor – **TCF**  
Tissue culture polystyrene – **TCPS**  
Vascular endothelial growth factor – **VEGF**  
Vascular endothelial growth factor receptor-2 – **VEGFR2**  
Volume of interest – **VOI**  
X-ray diffraction – **XRD**

## **Thesis Abstract**

Biomaterials for use in bone regeneration and healing range from metal and metal alloy implants to hydrogel-based solutions. These materials can be optimized to increase bone healing and integration by improving the mechanical and biological properties. Regardless of the material itself, the cell-substrate interaction is key to the success of the biomaterial once implanted. Substrate surface characteristics such as roughness, wettability and particle density are well-known contributors of a substrate's overall osteogenic potential, and therefore the substrates overall success. Unfortunately, it is still unknown how these substrate surface characteristics are transduced into intracellular signals by cells, preventing specific tailoring of biomaterial characteristics to maximize osteogenesis. One theory that has been postulated is that substrate characteristics modulate cytoskeletal changes which in turn differentially regulate numerous cell pathways. Specifically, the canonical Wnt signaling pathway, relies on  $\beta$ -catenin translocation to the nucleus to regulate transcription factors, which in the case of osteoblastic cells, regulate pro-osteogenic genes. Another role of  $\beta$ -catenin is its contribution to the formation and stabilization of cell adhesions such as focal adhesions and cadherins. Furthermore, previous studies have suggested that the  $\beta$ -catenin pool that stabilizes adhesions and cadherins may also be the same  $\beta$ -catenin pool that functions to induce osteogenesis. Evaluating the link between substrate surface characteristics, focal adhesions, and  $\beta$ -catenin could reveal how cells transduce substrate surface characteristics into intracellular signals and enable greater optimization of biomaterials for bone regeneration.

## **Chapter 1. Introduction**



## **SPECIFIC AIMS**

Numerous attempts at optimizing biomaterials for use in bone implants and bone tissue engineering have been made over the past decades. Three approaches have been utilized in an attempt to improve materials: optimization of current material properties, utilization of osteoinductive factors, or development of novel biomaterials with enhanced osteogenic properties<sup>1</sup>. The development of novel biomaterials provides an attractive avenue, as it provides the researcher with the greatest flexibility and affords them numerous options for producing a pro-osteogenic material. Combination polymers, incorporation of growth factors and small molecules, and advanced hydrogels have all yielded positive results and their successes have been reviewed in numerous studies<sup>1-3</sup>.

Despite the successes of biomaterials for bone implants and bone substitutes, it is still unknown how biomaterial substrate surface characteristics are transduced by bone cells and their precursors into intracellular signals. Further, it is unknown how this transduction then mediates cellular response and therefore a materials overall osteogenic potential. Literature has shown substrate surface characteristics such as roughness, wettability, and surface height may enhance osteogenesis<sup>4-6</sup>. However, these studies provide conflicting results as to which substrate surface characteristic is inducing the observed changes specifically<sup>4-9</sup>. This conflict reveals how specific materials, surface characteristics, cell type, and culture conditions can vary the observed results and cell response. It also highlights one of the largest knowledge gaps that affects the field of biomaterials, which is that the mechanism by which substrate surface characteristics modulate and are transduced by the cell into intracellular signals, is largely unknown.

Literature has suggested numerous mechanisms by which substrates are transduced by cells<sup>10-13</sup>. One proposed mechanism suggests that substrates may be transduced through cytoskeletal adhesion complexes, such as focal adhesions and cadherins, to the actin cytoskeleton. As the actin cytoskeleton remodels in response to changing tension generated by the focal adhesions, it can then alter nuclear morphology and gene expression, differentially regulating the cells in response to the substrate<sup>11,14</sup>. While this

model has garnered significant interest, it has also given rise to another proposed mechanism. This mechanism suggests that  $\beta$ -catenin may play a key role in the transduction of substrate surface characteristics. It has been observed that  $\beta$ -catenin stabilizes adhesion junctions by binding  $\alpha$ -catenin, though it is unclear whether it actively binds  $\alpha$ -catenin at focal adhesion complexes<sup>12,15</sup>. It has also been determined that  $\beta$ -catenin contributes to osteogenic regulation via the Wnt signaling pathway<sup>16</sup>. It has been hypothesized that  $\beta$ -catenin bound at focal adhesions may contribute to substrate surface transduction once liberated from focal adhesions<sup>11,17</sup>. Unfortunately, it has yet to be determined whether  $\beta$ -catenin bound at focal adhesions also translocates to the nucleus in response to changes in substrate surface characteristics.

The goal of this research is two-fold. The first is to evaluate a novel aptamer-functionalized fibrin hydrogel and the effect aptamer functionalization has on the induction of osteogenesis and angiogenesis. The second goal is to determine the mechanism by which biomaterial substrate characteristics are transduced enabling for the design and optimization of biomaterials with enhanced osteogenic properties. The overall hypothesis is that cellular transduction of a carbonated hydroxyapatite substrate occurs through a focal adhesion initiated  $\beta$ -catenin mediated mechanism. Specifically, as focal adhesion turnover and maturation occurs,  $\beta$ -catenin that is localized to the focal adhesion complex, is released when the complex disassembles. This release of  $\beta$ -catenin then allows for an increase in  $\beta$ -catenin concentration in the cytoplasm, and in turn an increase in nuclear translocation. Once  $\beta$ -catenin translocates, it is then able to regulate osteogenesis. Additionally, we hypothesize that formation of focal adhesions on the substrate is an accurate predictor of osteogenesis. Examination of the proposed mechanism and how it regulates osteoblastic differentiation will bridge a gap in our understanding of how substrate characteristics are transduced into the cell and evaluate focal adhesions correlation with osteogenesis.

**Aim 1. Evaluate the effects of VEGF loaded aptamer-functionalized fibrin hydrogel on angiogenesis and osteogenesis in a critical size cranial bone defect.**

A novel VEGF specific aptamer-functionalized fibrin hydrogel (AFH) will be evaluated for morphological and physical properties as well as VEGF release kinetics compared to fibrin hydrogel (FH) alone. After evaluation of AFH release kinetics we will examine AFH *in vivo* in a murine critically sized cranial bone defect model to determine the effect aptamer functionalization of the fibrin hydrogel has on the induction of angiogenesis and osteogenesis. We will load both FH and AFH with 2.5ug/mL and 10ug/mL of VEGF and implant it into a critically sized cranial defect. We will also have a non-treatment group, a non-loaded FH group, and a non-loaded AFH group to serve as controls. We will evaluate all groups for angiogenesis using MICROFIL perfusion followed by microcomputed tomography (microCT). We will also evaluate all groups for osteogenesis using microCT to examine bone formation within the defect site. Our sub-hypothesis is that the use of AFH with a greater concentration of VEGF will result in significantly greater angiogenesis and osteogenesis due to the improved release kinetics associated with aptamer functionalization.

**Aim 2. Determine how modification of an emulsion synthesis technique allows for the controlled synthesis of carbonated hydroxyapatite particles for use in the synthesis of substrates with various surface characteristics.**

We will engineer carbonated hydroxyapatite particles (CHA) of various sizes to develop substrates with various surface characteristics. Using an emulsion technique described by Zhou *et al.*<sup>18</sup>, we will manipulate temperature, pH, and homogenization speed (RPM) during the emulsion synthesis in order to evaluate how these variables control particle size. Particles will then be characterized for morphology and chemical composition. After CHA synthesis we will engineer a polycaprolactone (PCL) and CHA substratum in which particle size and density are varied independently. CHA of 200nm, 500nm, and 900nm will be suspended in 2.5% PCL solution as well as 500nm CHA at 5%, 30%, and 50 wt/wt CHA to PCL. Each substrate will be evaluated for particle density, roughness, wettability and height. Our sub-hypothesis is that modification of the emulsion process through variations in pH will enable tailored control over CHA particle size. In addition, incorporation of CHA particles at various concentrations will allow the generation of PCL/CHA substrates with various substrate characteristics.

**Aim 3. Determine which substrate composition and surface characteristic induces the greatest osteoblastic differentiation and examine how focal adhesion maturation and  $\beta$ -catenin localization are affected.**

We will use the substrates engineered in Aim 2 to characterize the cell response to each substrate. hFOB 1.19 cells, a preosteoblastic cell line, cultured on tissue culture polystyrene (TCPS) and the various substrate will be evaluated using alkaline phosphatase activity, gene expression, and protein expression for key osteoblastic markers to determine overall osteogenic potential of the substrate. Examination of focal adhesion formation, turnover, and maturation will be performed using immunofluorescent imaging and enzyme-linked immunosorbent assay (ELISA) to determine focal adhesion activity over time.  $\beta$ -catenin localization and translocation will be evaluated using cell fractionation to isolate  $\beta$ -catenin within the various cell compartments over time and quantified with ELISA.  $\beta$ -catenin translocation and activity will be further assessed using a luciferase-based reporter assay. Our sub-hypothesis is that the substrate that induces the greatest osteoblastic differentiation will also induce the greatest focal adhesion turnover and maturation. In addition,  $\beta$ -catenin translocation will be more rapid on this pro-osteogenic substrate as it translocates from the membrane where it is bound at focal adhesions, to the nucleus where it can regulate pro-osteogenic pathways.

**Aim 4. Determine how inhibition of focal adhesion turnover affects  $\beta$ -catenin localization and translocation on pro-osteogenic substrate.**

Using the pro-osteogenic substrate determined in Aim 2 we will evaluate osteoblastic cell response in the presence and absence of an inhibitor of focal adhesion kinase, PF-573228. We will evaluate osteoblastic differentiation using alkaline phosphatase activity, gene expression, and protein expression for key osteoblastic markers. Examination of focal adhesion formation, turnover, and maturation will be performed using immunofluorescent imaging and ELISA to determine focal adhesion activity over time.  $\beta$ -catenin localization and translocation will be evaluated using cell fractionation to isolate  $\beta$ -catenin within the various cell compartments over time and quantified with ELISA.  $\beta$ -catenin translocation and activity will be further assessed using a luciferase-based reporter assay. Our sub-hypothesis is that by inhibiting focal adhesion turnover and therefore focal adhesion disassembly, we will prevent the release of  $\beta$ -catenin from focal

adhesions and its translocation to the nucleus, mitigating the observed increase in osteoblastic differentiation in response to the pro-osteogenic substrate.

## **SIGNIFICANCE**

As our population continues to increase in average age, has more musculoskeletal injuries, and trends towards a more sedentary lifestyle the comorbidities associated with these factors also increase. In 2019 roughly 700 million persons worldwide were age 65 and older, with this number estimated to double to 1.5 billion persons by 2050. With a rise in population age also comes a rise in comorbidities associated with increased age, including an increase in bone diseases such as osteoporosis. As a result, injuries like hip fractures, associated with such diseases are also estimated to double, and possibly triple, increasing to 21 million hip fractures each year, with many necessitating a partial or total hip arthroplasty (replacement). In addition to injuries in the elderly population, significant musculoskeletal injuries are also becoming more prevalent in the younger population as well, with a roughly 150% increase in the number of injuries that occur in the United States each year. After injury, those who receive ACL reconstruction are seven times more likely to require a total knee arthroplasty. Lastly, with the increases in technology, the average sedentary time increased from 26 hours a week in 1965 to 38 hours a week in 2009, with this number only expected to rise. This lack of physical activity also contributes to bone diseases like osteoporosis, with the lack of activity resulting in bone resorption and a greater propensity for bone injury. This results in the need for improved biomaterials for use in bone implants and bone grafts.

Biomaterials that are used today in bone implants and grafts function well, yet they still are not ideal. For example, cementless titanium implants having a roughly 30% failure rate 15 years after implantation. The majority of these failures, approximately 75%, are caused by aseptic loosening, or the failure of bone implants to osseointegrate. Failure necessitates revision surgeries, which are technically demanding, have a high complication rate, are expensive, and are strenuous on the patients. Consequently, this creates a significant clinical need to improve the overall osteogenic potential of these implants, reducing the overall failure rate.

Numerous research efforts have focused on the improvement of current, and development of, new biomaterials. Despite these efforts, significant improvements have not been made. One reason for this is because we do not fully understand how bone cells and their precursors, specifically mesenchymal stem cells and osteoblasts, transduce the substrate surface characteristics of implants and how this transduction contributes to the regulation osteogenesis. Without this foundational understanding of the cell-substrate interaction, optimization of biomaterials will remain difficult. Gaining a foundational understanding of the cell-substrate interaction will allow biomaterials to be tailored to both the nano and macro scale, improving their overall osteogenic potential. This study focuses on evaluating the cell-substrate interaction on it most fundamental level rather than designing an osteogenic biomaterial itself. Knowledge gathered from this study will allow us to address the clinical need for implants that are capable of greater osseointegration and improved success.

## **Chapter 2. Background Information**

## **BONE OVERVIEW**

Bone is a complex tissue that provides structural support to the body, protects vital organs, acts as a reservoir for various factors and cells, and maintains homeostatic balance for certain minerals<sup>19</sup>. Bone is classified as either cortical or trabecular bone. Cortical bone is dense bone tissue that surrounds the marrow cavities, providing rigid structural support along the shaft or diaphysis<sup>20</sup>. Trabecular bone is a honeycomb like bone tissue that is within the marrow cavity and concentrated at the ends of most long bones in the metaphysis and epiphysis<sup>20</sup>. Trabecular bone gives bone the ability to withstand repeated loading and absorb greater forces than just cortical bone alone. Typically, the collagen fibrils of bone tissue are deposited in a lamellar, or interwoven pattern<sup>21</sup>. This pattern provides greater mechanical strength to the bone tissue allowing it to withstand physiological loads. In contrast, the collagen fibrils of woven bone are deposited in a random manner, generating bone tissue with significantly weaker mechanical properties than lamellar bone<sup>21</sup>. Woven bone is most often seen early in the bone development process and during bone healing<sup>19</sup>.

Bone is composed of a mineral phase, primarily hydroxyapatite, and an organic phase, primarily type I collagen. Bone hydroxyapatite crystals are roughly 200nm in size, with a crystallinity ranging from 60-70%<sup>22</sup>. In addition, physiological hydroxyapatite is often carbonate substituted, allowing for greater solubility<sup>23</sup>. The mineral component of bone provides the rigidity and mechanical strength to the bone tissue, allowing the tissues to withstand greater compressive loading.

Bone is constantly remodeled, undergoing a process of resorption and formation in response to mechanical loads. Bone resorption is primarily the results of osteoclasts cells, which differentiate from hematopoietic stem cells in a process known as osteoclastogenesis<sup>24</sup>. Osteoclasts form bone resorbing compartments in response to mechanical cues and signals from other bone cells. Resorption is achieved by creating an acidic environment within the bone resorbing compartment, allowing the mineralized bone matrix to be degraded and mobilized<sup>24</sup>. Bone formation is primarily the result of



osteoblastic cells, which differentiate from mesenchymal stem cells in a process known as osteoblastogenesis<sup>24</sup>. Osteoblasts deposit collagen matrix in response to mechanical cues and signals from other bone cells. Osteoblasts then induce collagen mineralization by releasing calcium and phosphate locally, triggering mineralization of the collagen fibrils<sup>20</sup>. Osteoblasts also line the outer surface of bone, and once entrapped in bone matrix differentiate into osteocytes. Osteocytes are the most abundant cell in bone tissue, comprising roughly 80% of the total cell volume<sup>25</sup>. These cells are known mechanosensors, regulating bone homeostasis through signaling to both osteoclasts and osteoblasts<sup>21</sup>.

## **THE OSTEOINTEGRATION PROCESS**

Osseointegration is defined as a time dependent healing process whereby clinically asymptomatic rigid fixation of alloplastic materials is achieved, and maintained, in bone during functional loading<sup>26</sup>. It is necessary for implant success, as lack of osseointegration often results in micromotion of the implant resulting in inflammation, osteolysis, and implant failure<sup>21,27</sup>. The osseointegration process is complex and depends heavily on both the bone formation and remodeling process as well as the implant itself for successful integration.

Osseointegration starts with the initial trauma during implant placement into the bone tissue. This trauma causes localized hemorrhage from damaged blood vessels. This results in hematoma formation that bridges the region between the existing healthy bone tissue and the implant surface (Figure 1a)<sup>21</sup>. The hematoma, composed largely of fibrin, provides an initial matrix for local immune cells to adhere and begin to release cytokines to recruit a host of immune cells<sup>21,28</sup>. The recruited immune cells provide debridement of the injured site and damaged tissue. They also secrete various cytokines that recruit other immune, endothelial progenitor, and mesenchymal progenitor cells to the injury site (Figure 1b).

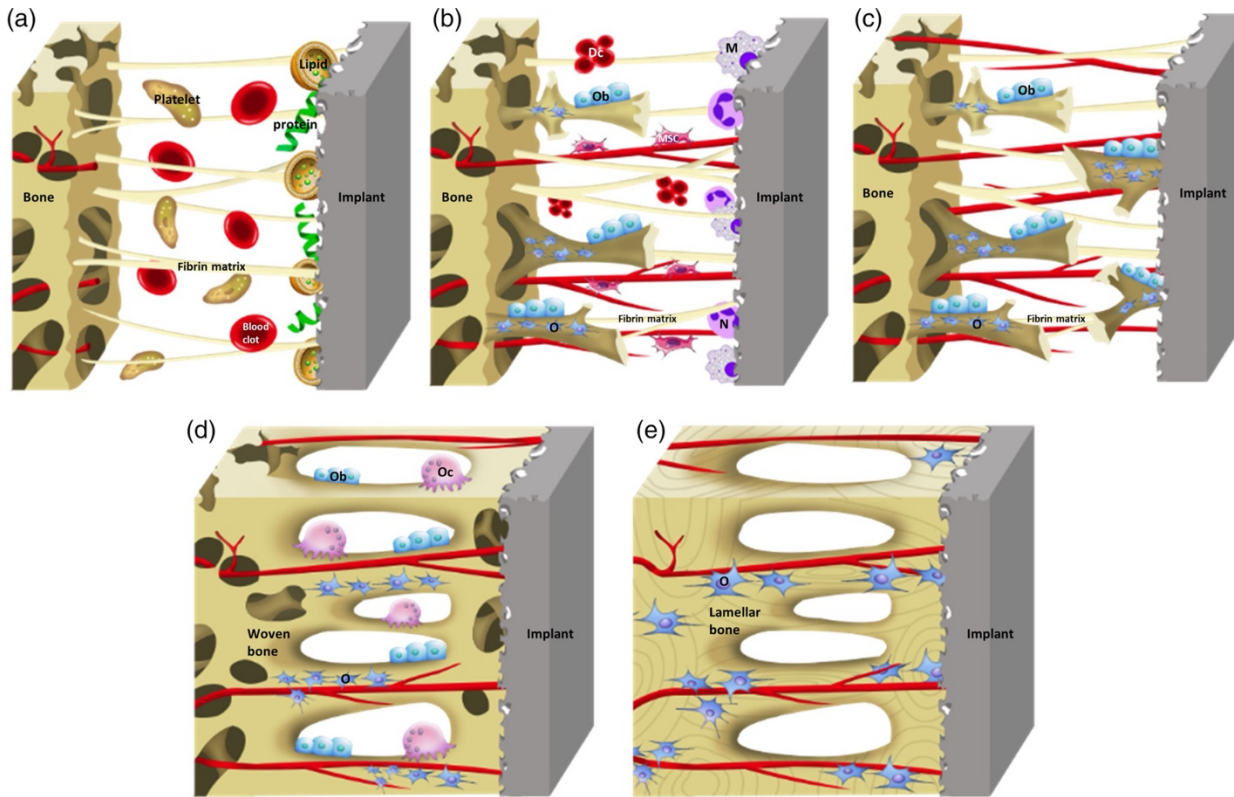


**Figure 1.** Schematic of the process of implant osteointegration. The process begins with the formation of a blood clot and fibrin bridge between implant and healthy bone tissue (a). Immune cell debridement and recruitment of various cells to the injury site (b). Differentiation of progenitor cells resulting in angiogenesis, woven, and intramembranous bone formation (c). Osteogenesis occurs bridging the gap between the healthy bone tissue and the implant surface (d). Woven bone is transformed into lamellar bone tissue. (e) Clot decomposition and bone homeostasis. Dc, decomposed clot; M, macrophage; MSC, mesenchymal stem cell; N, neutrophil; O, osteocyte; Ob, osteoblast; Oc, osteoclast. Reproduced with permission from Liu *et al.* Role of Implants Surface Modification in Osseointegration: A Systematic Review. © 2019 Journal of Biomedical Materials Research Part A. John Wiley & Sons, Inc.

After hematoma formation, inflammation, and the recruitment of immune and progenitor cells the fibrovascular phase begins. During this phase both existing epithelial and differentiated progenitor cells revascularize the injury site through either angiogenesis or vasculogenesis (Figure 1c)<sup>21</sup>. During this time mesenchymal progenitor cells begin to differentiate into either chondrocytes or osteoblastic cells, with commitment to the chondrogenic lineage caused by an increase in *SOX9* and a decrease in Runt related transcription factor-2 (*RUNX2*) and a commitment to osteoblastic lineage caused by an increase in *RUNX2* and a decrease in *SOX9*<sup>21,27</sup>.

Following the fibrovascular phase bone formation begins. Mature osteoblasts begin to deposit collagenous matrix and various ions to induce matrix mineralization forming intramembranous bone tissue (Figure 1d). Conversion of chondrocytes to a hypertrophic state results in the conversion of these collagenous callus to mineral forming endochondral bone. It is important to note that implant motion has been shown to cause greater endochondral ossification, whereas greater implant stability results in greater intramembranous ossification<sup>21</sup>. Because of this, intramembranous ossification primarily occurs directly along the healthy bone tissue surface, whereas endochondral ossification occurs in the gap between the implant and healthy bone tissue<sup>28</sup>. This process occurs until primary bone formation has been completed.

Finally, after primary bone formation, osteoclast-mediated remodeling of the bone occurs. Provisional bone, known as woven bone, initially deposited during primary formation is resorbed and replaced with mature lamellar bone (Figure 1e)<sup>26,29,30</sup>. This process continues over the next 6 to 12 months, remodeling the deposited bone in response to mechanical stimuli. Once complete, the ingrowth of healthy bone tissue into the implant surface allows for full integration.

## **BIOMATERIALS IN BONE REPAIR**

Both bone formation and resorption play a critical role in the bone healing process and are required for successful bone healing over time. However, certain defects and injuries necessitate the use of bone implants. These implants are typically composed of a combination of metals that favored for their biocompatibility, ease of use, and mechanical strength. However, cementless titanium implants, such as the ones commonly used for dental and hip procedures have a roughly 15% to 30% failure rate 15 years after implantation<sup>26</sup>. The majority of these failures, approximately 75%, are caused by aseptic loosening<sup>26</sup>. This loosening can be caused by stress shielding and poor osteointegration, which results in motion of the implant causing osteolysis and implant failure<sup>1</sup>. This highlights the need for improved or novel biomaterials with enhanced osteogenic

properties. Three approaches have been utilized in an attempt to improve materials: optimization of current material properties, utilization of osteoinductive factors, or development of novel biomaterials with enhanced osteogenic properties<sup>30,31</sup>.

Optimization of current biomaterials has focused on increasing the osteoconductive nature of the material itself to promote osteointegration. This has primarily been done through modification of the substrate surface characteristics, specifically increasing the macro and nano roughness. Surface modifications that are typically performed include grit blasting, acid etching, anodization, and plasma spraying with either a metal or osteoconductive materials such as hydroxyapatite<sup>30</sup>. The intent of increasing surface roughness is two-fold. First it is meant to increase the surface area of the implant, therefore increasing the total area with which the bone can integrate. Second, previous studies have shown that increasing the surface roughness of the implant can facilitate biological changes such as bone cell migration, proliferation, differentiation, and protein absorption. In addition, more recent studies have also suggested that the methods used for the modification of the surface roughness varies the chemical composition of the implant. Modification of surface roughness can also cause changes in other surface characteristics. Variations in the height and wettability of substrate surfaces have been shown to be important in regulating cell adherence and differentiation, although these results are heavily dependent on the material, cell type, and other biological conditions. Aside from increasing surface roughness, enhancing the surface bioactivity has also yielded positive results for increasing implants osteogenic potential. Functionalization of ions and organic molecules onto the implant surface allow for binding of both cells and proteins onto the implant surface while also promoting osteogenesis<sup>32</sup>.

Incorporation of osteoinductive factors into the biomaterial or onto the biomaterial surface has also allowed for significant improvements in implant osteointegration. One approach currently utilizes osteoinductive materials, such as hydroxyapatite, and bioinorganic ions, such as magnesium and zinc<sup>33</sup>. These osteoinductive materials are incorporated directly onto the implant surface. This has both the advantage of increasing the surface roughness of the implant itself while also providing pro-osteogenic chemical cues to

promote bone formation and implant integration. Another approach that has been utilized is the incorporation of biologics such as bone morphogenic protein-2 (BMP2), parathyroid hormone (PTH), platelet rich plasma (PRP), fibroblast growth factors (FGF), and vascular endothelial growth factor (VEGF)<sup>33</sup>. These agents positively regulate bone formation by encouraging angiogenesis and/or the maturation of osteoblast progenitors<sup>26</sup>. Unfortunately, use of biological factors is a temporary solution, designed to provide an initial increase in osteogenic and angiogenic potential. And as previously mentioned, implants perform well during initial implantation, with most failures occurring after an extended duration<sup>1</sup>. Without continued osteogenic promotion, successful osteointegration over time may not be successful.

Development of novel biomaterials with enhanced osteogenic and angiogenic properties for use as orthopedic implants has garnered significant interest in the past few decades. New materials often utilize one or more osteoinductive material. Polymers, typically polycaprolactone (PCL) or poly(lactic-co-glycolic acid) (PLGA) provide sufficient mechanical strength while also exhibiting good biocompatibility<sup>1,34</sup>. Novel ceramics, such as porous bioactive glass and alumina-based implants have also shown significant osteoconductive properties<sup>35,36</sup>. Hydrogels provide a highly conducive environment for cell integration and differentiation, mimicking the extracellular matrix more closely than other materials<sup>37,38</sup>. Additionally, hydrogels are easily loaded with osteoinductive factors allowing them to be modified to be optimally osteogenic and angiogenic<sup>1,39,40</sup>. Development of materials that utilize a combination of polymers, ceramics, and hydrogels have been studied and summarized in numerous reviews<sup>41,42</sup>. Through the combination of these materials the mechanical, angiogenic, and osteogenic properties can be tuned to create an implant that is optimally osteogenic while also providing the mechanical properties required to prevent loosening and induce osteointegration.

Despite the significant advances in biomaterial design and development, engineering bone implants with low failure rates that integrate fully has been difficult<sup>10</sup>. This is in large part due to a lack of understanding of how substrates are transduced by bone cells and their progenitors<sup>10,43,44</sup>. While we understand that increasing roughness and optimizing

other substrate characteristics provides a more osteogenic implant overall, the mechanism by which the implant induces osteogenic differentiation and therefore bone formation is still unknown, preventing greater optimization of implant characteristics.

## **CELL TRANSDUCTION OF SUBSTRATES**

Cell transduction of substrate surfaces is a highly complex process and the mechanism by which this occurs is largely unknown<sup>11</sup>. Mechanotransduction is traditionally thought of as an extracellular mechanical signal that is converted into intracellular chemical signals<sup>11,12,45</sup>. The relationship between substrate surface characteristics and the response by the cells is heavily reliant on the material, surface modifications, cell type, and culture conditions. Attempts at discerning a mechanism by which the cell translates substrate surface characteristics into intracellular signals have not yielded a definitive result. Despite this, researchers have concluded that the cytoskeleton plays an integral role in the transduction process<sup>46,47</sup>.

The cytoskeleton is a dynamic structure that connects the regions of the cell and provides structure and tension and transmits mechanical forces throughout the cell. Inhibition of cytoskeleton formation and attachment prevents transduction of loading and fluid shear<sup>48,49</sup>. This evidence highlights that importance of the cytoskeleton in the transduction of mechanical signals. Numerous theories as to how this transmission of force through the cytoskeleton regulates intracellular signaling pathways have been hypothesized. One theory is the model of tensegrity<sup>48-50</sup>. In this model, increased tension on the cytoskeleton allows for the deformation of various cellular structures, including the nucleus. This deformation of the nucleus then differentially regulates various intracellular pathways and can explain various features of living cells<sup>51</sup>. However, this theory has not explained the observed changes in intracellular protein levels and localization.

The cytoskeleton is regulated heavily through the Rho-family of guanosine triphosphate enzymes (GTPases), which includes RhoA, Rac1, Cdc42. The cytoskeleton is connected to the extracellular matrix through the focal adhesion complex<sup>52</sup>. These adhesions create

traction forces that generate tension within the cell and help to regulated cytoskeletal organization<sup>53</sup>. In addition, these focal adhesions regulate various cell functions including migration, proliferation, differentiation, and apoptosis<sup>54–56</sup>. The transmembrane portion of the focal adhesions, the integrins, bind the extracellular matrix. They have been observed interacting differently based on the substrate surface characteristics that are presented<sup>7,57</sup>. On pro-osteogenic substrates it has been noted that focal adhesion maturation and formation is also increased<sup>58</sup>. With turnover of the adhesions occurring more rapidly on pro-osteogenic substrates, it also suggests that focal adhesions may be a key initiator of cell mechanotransduction, with the focal adhesion acting to initiate cell transduction of the substrate surface<sup>59</sup>.

Focal adhesions share many components to cadherins and bind the actin cytoskeleton in a similar manner<sup>12</sup>. It is reasonable to hypothesize that focal adhesions use  $\beta$ -catenin to bind the actin cytoskeleton in the same manner that E-cadherins do. In this manner,  $\beta$ -catenin binds and is stabilized by  $\alpha$ -catenin<sup>12</sup>.  $\alpha$ -catenin then binds actin directly or indirectly after binding vinculin<sup>60,61</sup>. Studies have also suggested that  $\beta$ -catenin may also bind vinculin directly and that this complex formation allows for the adhesion to be capable of supporting mechanical tension<sup>62</sup>.

$\beta$ -catenin is part of the Wnt signaling pathway and is a key regulator of osteogenesis. As the main transcription factor,  $\beta$ -catenin, upon translocation to the nucleus, binds TCF/LEF. Once binding occurs this interaction acts to upregulate various genes associated with osteogenesis, including *RUNX2*<sup>63</sup>.  $\beta$ -catenin is typically phosphorylated by a complex, that includes glycogen synthase kinase-3 $\beta$  (GSK-3 $\beta$ ), Axin, and adenomatous polyposis coli (APC), which results in the degradation of  $\beta$ -catenin. Inhibition of  $\beta$ -catenin results in an osteopenic bone phenotype as a result of poor osteoblastic differentiation and increased osteoclastogenesis<sup>64,65</sup>. Conversely, stabilization of  $\beta$ -catenin causes higher bone mass, increased osteoblastogenesis, and greater ossification resulting in greater bone formation overall<sup>66</sup>. This highlights the integral role of  $\beta$ -catenin in regulating and directing osteogenesis.

Interestingly, it is unknown whether there are two separate pools of  $\beta$ -catenin, the one involved in adhesion stabilization and the one involved in intracellular signaling, overlap<sup>66,67</sup>. Current research suggests that these pools interact, with changes in  $\beta$ -catenin phosphorylation occurring to allow the transition of  $\beta$ -catenin between the adhesion pool and the intracellular signaling pool<sup>68-73</sup>. If this interaction is occurring, further research is needed to evaluate a possible mechanism by which  $\beta$ -catenin commonly localized to focal adhesions may participate in intracellular signaling in response to substrate surface characteristics and other mechanical cues.



**CHAPTER 3. Aptamer-Functionalized Fibrin Hydrogel  
Improves Vascular Endothelial Growth Factor Release  
Kinetics and Enhances Angiogenesis and Osteogenesis in  
Critically Sized Cranial Defects**

Authors:

Otto J. Juhl IV, Nan Zhao, Anna-Blessing Merife, David Cohen, Michael Friedman, Yue Zhang, Zvi Schwartz, Yong Wang, Henry J. Donahue

*ACS Biomaterial Science & Engineering, 2019, 5, 11, 6152–6160*

## ABSTRACT

An aging population, decreased activity levels and increased combat injuries, have led to an increase in critical sized bone defects. As more defects are treated using allografts, which is the current standard of care, the deficiencies of allografts are becoming more evident. Allografts lack the angiogenic potential to induce sufficient vasculogenesis to counteract the hypoxic environment associated with critical sized bone defects. In this study, aptamer-functionalized fibrin hydrogels (AFH), engineered to release vascular endothelial growth factor (VEGF), were evaluated for their material properties, growth factor release kinetics, and angiogenic and osteogenic potential *in vivo*. Aptamer functionalization to native fibrin did not result in significant changes in biocompatibility or hydrogel gelation. However, aptamer functionalization of fibrin did improve the release kinetics of VEGF from AFH and, when compared to fibrin hydrogels (FH), reduced the diffusivity and extended the release of VEGF several days longer. VEGF released from AFH, *in vivo*, increased vascularization to a greater degree, relative to VEGF released from FH, in a murine critical-sized cranial defect. Defects treated with AFH loaded with VEGF, relative to non-hydrogel loaded controls, showed a nominal increase in osteogenesis. Together, these data suggest that AFH more efficiently incorporates and retains VEGF *in vitro* and *in vivo*, which then enhances angiogenesis and osteogenesis to a greater extent *in vivo* than FH.

## INTRODUCTION

Critical sized bone defects, defects that do not heal completely without intervention, continue to be an issue in clinical settings. Biomaterials used to treat critical sized bone defects do exceptionally well at inducing angiogenesis or osteogenesis, but rarely both, and fail roughly 13% of the time<sup>1,3,68,74</sup>. Many materials used impair self-healing, which is problematic when determining effective treatments for critical sized bone defects<sup>75,76</sup>. With the number of critical sized bone defects rising due to the increased prevalence of diseases such as osteoporosis, resulting in more severely comminuted fractures, and high-energy injuries such as those commonly seen in the armed forces it is important to

provide viable solutions to meet this growing need<sup>77</sup>. The development of new scaffolds, grafts, and other biomaterials has led to alternate forms of treatment for critical sized bone defects and bone nonunion<sup>78</sup>. However, bone allografts continue to be the most widely used graft material to heal critical sized defects.

While allografts are often used to treat critical sized defects in both load bearing and non-load bearing situations, they present several problems. For instance, allografts often do not resolve the hypoxic environment typically associated with large bone defects, because they fail to vascularize fully. Additionally, infection and rejection, often caused by the innate immune response to leftover cellular debris in the grafts themselves, prevent complete bone union and ossification<sup>68,75,79</sup>. If complete bone union is not achieved, then the patient risks a host of complications ranging from defect site pain to local or possible systemic infection<sup>80</sup>. The use of biomaterials in tandem with allografts allows for an improved angiogenic and osteogenic response, providing a greater healing response than allografts alone<sup>81</sup>. Current biomaterials are adequate at restoring both structure and function in smaller bone defects but often lack the angiogenic potential needed to sufficiently vascularize critical sized bone defects<sup>82-84</sup>. Thus, the hypoxic environment commonly associated with these defects is not resolved, preventing complete healing<sup>82</sup>. Hydrogels, a promising group of biomaterials that mimic the extracellular matrix and are conducive to both angiogenesis and osteogenesis, are being explored as a potential solution to this problem<sup>85</sup>. Hydrogels are flexible and multifaceted, allowing them to be tailored to improve various properties. Unfortunately, because hydrogels lack the mechanical stability needed for load-bearing defects, hydrogels are instead utilized in conjunction with a mechanically competent scaffold in load bearing situations or as a filler for non-load bearing situations<sup>38</sup>. With that stated, there are various types of hydrogels, with one of the most commonly used hydrogels being native fibrin hydrogel (FH).

Native FHs are commonly used because of their simplicity and conduciveness to cell growth. Compared to other hydrogels, FHs are highly dynamic and biocompatible, making them advantageous for numerous healing applications<sup>80,85</sup>. In clinical application, FH forms a three-dimensional polymerized network anchored by fibroblasts, eventually

becoming stiff enough to regulate wound hemostasis<sup>83</sup>. FH has also been shown to moderately induce osteogenesis but does not enhance angiogenesis effectively, a necessity for critically sized defect repair<sup>85</sup>. Attempts at loading FH with growth factors such as vascular endothelial growth factor (VEGF), which induces endothelial cell mitogenesis and tubule formation, have had moderate success at resolving this problem. Unfortunately, FH, like other hydrogels, poorly incorporates or retains growth factors. Instead, FH exhibits a “burst release” kinetic with the majority of the growth factor being released over an initial 48-hour period<sup>83,86,87</sup>. To solve this, we have developed a novel nucleotide aptamer-functionalized fibrin hydrogel (AFH) with improved retention and release kinetics, compared to non-aptamer-functionalized FH.

Aptamers, typically comprised of a highly specific sequence of oligonucleotides or peptides, bind to their target molecules with extremely high affinities<sup>88</sup>. The engineered aptamer conjugated to fibrinogen, and with the addition of thrombin, forms AFH with an enhanced affinity for a specific growth factor<sup>83</sup>. AFH exhibits similar structural qualities to native FH but also offers tailorable release kinetics<sup>89</sup>. Past studies have shown that AFH loaded with VEGF can be used to enhance vascularization in skin defects, but minimal research has been done to evaluate AFH in bone regeneration and healing<sup>83,87</sup>. This gap in knowledge has led us to examine how AFH loaded with VEGF affects angiogenesis and osteogenesis in a critical sized cranial bone defect.

We implanted VEGF-loaded AFHs in an established murine cranial defect model<sup>55</sup>. We hypothesize that VEGF-loaded AFHs with improved VEGF release kinetics increase, compared to VEGF-loaded FHs, angiogenesis and osteogenesis.

## **MATERIALS AND METHODS**

### **Materials.**

All chemicals used for aptamer functionalization and hydrogel synthesis were obtained from Sigma-Aldrich (St. Louis, MO). Fibrinogen and thrombin were purchased from Millipore (Billerica, MA). VEGF and enzyme-linked immunosorbent assay (ELISA) kits for

VEGF were purchased from PeproTech (Rocky Hill, NJ). VEGF-binding aptamer and complementary sequence of VEGF-binding aptamer (Table 1) were purchased from Integrated DNA Technologies (Coralville, IA). Nylon sutures were purchased from Ethilon (Johnson & Johnson Medical N.V., Belgium). Radiopaque MICROFIL solution was purchased from Flow-Tech Inc. (Microfil, Flow-Tech Inc., Carver, MA). Decalcification solution was purchased from Statlabs (StatLab, McKinney, TX). Eppendorf tubes used for scanning purposes were purchased through Thermo-Fisher Scientific (Waltham, MA).

### Hydrogel Preparations and Synthesis.

Aptamer-conjugated fibrinogen was synthesized using methods previously reported (Figure 2a)<sup>55</sup>. Briefly, 50 mg of native fibrinogen was reacted with acrylic acid N-hydroxysuccinimide (NHS) in NaHCO<sub>3</sub> (0.1 M) solution for 4 hours. Unreacted NHS and byproducts were removed by washing with a 100 kDa centrifugal filter. Thiol-modified anti-VEGF aptamers were reduced in 50 mM tris(2-carboxyethyl) phosphine hydrochloride at room temperature. The reduced aptamers were purified, and 30 nmol of aptamer reacted with 50 mg of acrylate-modified fibrinogen in Tris-HCl buffer. Then the fibrinogen conjugated with the anti-VEGF aptamer was purified with a 100 kDa centrifugal filter and stored at -20 °C for future use.

**Table 1.** DNA sequence of VEGF Aptamer

DNA name	Sequence (5'-->3')
Aptamer	/ThiolMC6-D/AAAAA AAAAA CCCGT CTTCC AGACA AGAGT GCAGG G
Complementary sequence of aptamer	CCCTG CACTC TTGTC TGGAA GACGG G

Fibrinogen and aptamer-conjugated fibrinogen were mixed to form a pre-gel solution (20 mg/mL total fibrin). Thrombin and CaCl<sup>2</sup> were then mixed to form the second pre-gel solution (2 U/mL of thrombin and 10 mM CaCl<sup>2</sup>). The two pre-gel solutions were then mixed and allowed to mature at 37 °C for 1 hour. To make VEGF-loaded hydrogels, VEGF was first added to either the fibrin solution or the aptamer-functionalized fibrin solution that was then used for hydrogel preparation. Native (no aptamer) fibrin hydrogel, with or

without VEGF, was used as a control. For all of the following experiments, the molar ratio of the aptamer to VEGF in the aptamer-functionalized hydrogel was kept at 20:1.

### **Hydrogel Evaluation.**

#### *Gelation Time.*

25 $\mu$ L of aptamer-conjugated fibrinogen (4 mg/mL) was mixed with 25 $\mu$ L of fibrinogen (16 mg/mL) and transferred to a BMD-QuickCoag 1004 coagulometer (BioMedica, Nova Scotia, Canada). 25 $\mu$ L of CaCl<sup>2</sup> (20 mM) was mixed with 25 $\mu$ L of thrombin (4 U/mL). The mixtures were allowed to equilibrate to 37°C. Then 50 $\mu$ L of the CaCl<sup>2</sup> and thrombin solution was added to the coagulometer to initiate the gelation process and the gelation process initiated on the coagulometer. Once the movement of the magnetic bar in the coagulometer is stopped, gelation time was recorded. All gelation was measured at 37 °C.

#### *Dynamic Modulus.*

25 $\mu$ L of aptamer-conjugated fibrinogen (4 mg/mL) was mixed with 25 $\mu$ L of fibrinogen (16 mg/mL). The two parts were mixed and transferred to a Discovery HR3 rheometer (New Castle, DE). A strain sweep was performed at a frequency of 10 rad/s from 0.1% to 15% to determine the linear viscoelastic region. The dynamic modulus was determined using an oscillatory strain sweep at a strain of 1% and a frequency of 1 Hz.

#### *Bulk Hydrogel Imaging.*

Hydrogels were stained with complementary sequences (4  $\mu$ M) of the VEGF-binding aptamers at room temperature. Then the hydrogels were washed with PBS and stained with SYBR Safe. After washing with PBS 3 times, the hydrogels were imaged with a Maestro Imaging System (Woburn, MA).

#### *Scanning Electron Microscopy.*

Hydrogels were fixed with a 4% paraformaldehyde solution, washed with ddH<sub>2</sub>O 3 times, frozen at -80 °C, and then lyophilized. The lyophilized materials were sputter-coated with iridium and imaged with a scanning electron microscope (Zeiss Sigma, US). For all

images, a 5 kV acceleration voltage was used, and all images were taken at a working distance of 5.5 mm and a 2000 magnification.

#### *VEGF Release Profile.*

AFH loaded with 2  $\mu\text{M}$  aptamer and 100 nM VEGF and native non-aptamer-functionalized FH loaded with 100 nM VEGF with diameters of 8 mm and thicknesses of 1 mm were incubated in 1 mL of release media (0.1% bovine serum albumin supplemented Dulbecco's phosphate buffered saline (DPBS)). The release media was collected at predetermined time points and replenished with a new release media. The collected release media was stored at  $-20\text{ }^{\circ}\text{C}$ . To quantify the amount of VEGF in collected release media, ELISA was performed according to the manufacture's protocol. The effective diffusivity of VEGF from FH and AFH was calculated using Equation 1<sup>74,90</sup>.

$$\frac{M_t}{M_o} = 4 \left( \frac{D}{\pi l^2} \right)^n t^n \quad \text{Equation 1}$$

where  $M_t$  is the amount of released VEGF at time  $t$ ,  $M_o$  is the total amount of VEGF,  $M_t/M_o$  is the fractional release,  $D$  is the effective diffusivity,  $l$  is the thickness of the hydrogel, and  $n$  is the diffusional exponent ( $n = 0.5$ ).

#### **In Vivo Evaluation.**

All animal procedures were performed in accordance with the Virginia Commonwealth University Institutional Animal Care and Use Committee guidelines and requirements. Skeletally mature, 16-week-old male C57/B6J mice (Jackson Laboratories, Bar Harbor, ME) were housed in a light and temperature-controlled environment with free access to food and water. There were 7 experimental groups (Table 2). VEGF concentrations of 2.5  $\mu\text{g}/\text{mL}$  and 10  $\mu\text{g}/\text{mL}$  were chosen to be similar to previous literature where 2  $\mu\text{g}/\text{mL}$  was used in a skin defect model with similar aptamer-functionalized hydrogels, and 10  $\mu\text{g}/\text{mL}$  was used in a femoral fracture model<sup>38,39</sup>.

**Table 2.** Hydrogel Treatment Groups

Experimental Group	Hydrogel Type	VEGF Concentration
Non-Hydrogel Loaded Control (E)	None	None
Fibrin Hydrogel (FH)	Fibrin	None
Fibrin Hydrogel w/ 2.5µg/mL VEGF (2.5FH)	Fibrin	2.5 µg/mL
Fibrin Hydrogel w/ 10µg/mL VEGF (10FH)	Fibrin	10 µg/mL
Aptamer-Functionalized Hydrogel (AFH)	Fibrin  Aptamer-Functionalized Fibrin	None
Aptamer-Functionalized Hydrogel w/ 2.5µg/mL VEGF (2.5AFH)	Fibrin  Aptamer-Functionalized Fibrin	2.5 µg/mL
Aptamer-Functionalized Hydrogel w/ 10µg/mL VEGF (10AFH)	Fibrin  Aptamer-Functionalized Fibrin	10 µg/mL

*Critical Sized Cranial Defect Model.*

The cranial defect was created as previously reported<sup>83</sup>. Mice were anesthetized with 2.5% isoflurane, followed with a toe pinch to confirm the depth of the anesthesia. Mice then received 0.6 mg/kg of buprenorphine to relieve pain intra- and postoperatively. An incision that extends over the majority of the dorsal skull was created, and the skin was retracted to expose the parietal bone. Using a 4 mm external diameter trephine drill bit, a critically sized defect (Figure 1) was made in the parietal bone, using caution not to extend the defect into the underlying dura mater. 13µL of sterile hydrogel from each group listed



in Table 2 was then injected into the defect site. A non-injected control group without hydrogel served as the negative control with 6 mice per group per time point. The hydrogel was then allowed to cure for 3 minutes before the defect site was closed using a horizontal mattress suture technique.



**Figure 1.** Representative images of the critical sized bone defect. (a) A superior view of the 4 mm defect created in the left parietal bone of 16-week-old male mice at 7 days post-defect introduction with no intervention performed, (b) 14 days post-defect introduction with no intervention performed, and (c) 21 days post-defect introduction with no intervention performed. The images show little to no healing, affirming that a critical sized bone defect that will not heal without external intervention was created.

#### *Vascular Perfusion.*

After defect creation and treatment, animals were sacrificed at 7, 14, and 21 days. To assess angiogenesis, mice were perfused with a radio-opaque silicone-based contrast agent, MICROFIL, to visualize the vasculature as previously reported<sup>82,91</sup>. Mice were first anesthetized with 2.5% isoflurane, followed with a toe pinch to confirm the depth of the anesthesia. A catheter was placed into the apex of the left ventricle. Using a peristaltic

pump (Cole Parmer, Vernon Hills, IL), 7 mL-heparinized PBS (50 U/mL) was perfused through the mouse's vasculature at 0.7 mL/min. Complete perfusion of the vasculature was assessed by hepatic filling and by the perfused solution leaving the right atrium of the heart. Following heparin perfusion, the animal's vessels were perfused with 7 mL of 10% neutral buffered formalin to maintain vessel structure and integrity at 0.7 mL/min. 3 mL of prepared MICROFIL solution (53% MICROFIL, 42% diluent, 5% curing agent) was then perfused through the upper vasculature of the animal at 0.3 mL/min. The MICROFIL was then allowed to polymerize for 90 minutes at room temperature and then overnight at 4 °C to ensure complete polymerization. After polymerization, the head was dissected from the body and placed into 10% neutral buffered formalin until microCT analysis.

#### *Micro-CT Analysis.*

Micro-CT was used to examine both calcified and decalcified samples. Samples were first dried and then placed into 50 mL Eppendorf tubes. Specimens were then fixed to specimen holders in a Skyscan 1172 (Bruker, Billerica, MA). Scanning was performed at 57 kV and 87 mA. The rotational step size and zoom were set to 0.2 degrees and 17.98  $\mu\text{m}$  voxels, respectively. The scan resolution was set to medium, creating a 1024  $\times$  1024 pixel image matrix.

Images were reconstructed using a modified Feldkamp algorithm via N-Recon Software (Kontich, Belgium). Images were processed to remove noise and produce accurate structure before reconstruction. Beam hardening reduction was performed at 20%, and ring artifact reduction and post-alignment were performed at various steps based on the quality of each image. The histogram setting was held at a uniform range of 0 to 0.032168.

After reconstruction, DataViewer (Kontich, Belgium) was used to select a volume of interest (VOI) that completely encompassed the defect based on visualization of the defect and normalization to the curvature of the skull. The cranial VOI was then analyzed using CTAn (Bruker, Billerica, MA). A binary representation of the bone was then created with a minimum threshold value of 110. Bone volume to total volume (BV/TV) was measured in three-dimensional space to normalize for variations in bone thickness.

After initial analysis using micro-CT to identify calcified bone healing, skulls were placed in a decalcification solution for 72 hours with gentle agitation. After decalcification, the samples were rinsed thoroughly and placed in 10% neutral buffered formalin until analysis. Decalcified skull samples underwent similar micro-CT scanning and reconstruction. After reconstruction, samples were evaluated to determine if the MICROFIL perfusion was successful. Complete perfusion of the carotid arteries on both sides of the skull was considered successful. If the carotid arteries were not perfused, the sample was excluded from analysis; 3 mice were excluded for this reason. A binary representation of the VOI was then created with a minimum threshold value of 125 and a maximum value of 210. Percent vascularization, which is a measure of vessel volume divided by total defect volume, vessel separation, which is a measure of the average distance between a vessel and its nearest neighboring vessel, and vessel density, which is a measure of the number of vessels per micron, were then quantified in a three-dimensional space.

### **Statistical Methods.**

Analysis between treatment groups was performed using one-way ANOVA followed by Tukey's post hoc analysis with SigmaPlot statistical analysis software version 14 (Systat Software, Inc., San Jose, CA, USA). All hydrogel property analysis is shown as mean  $\pm$  SD, while in vivo studies are shown as mean  $\pm$  SEM. Correlation coefficients between data were determined using a Spearman nonparametric correlation test (GraphPad Software, La Jolla, CA, USA). Values of  $p < 0.05$  were considered statistically significant.

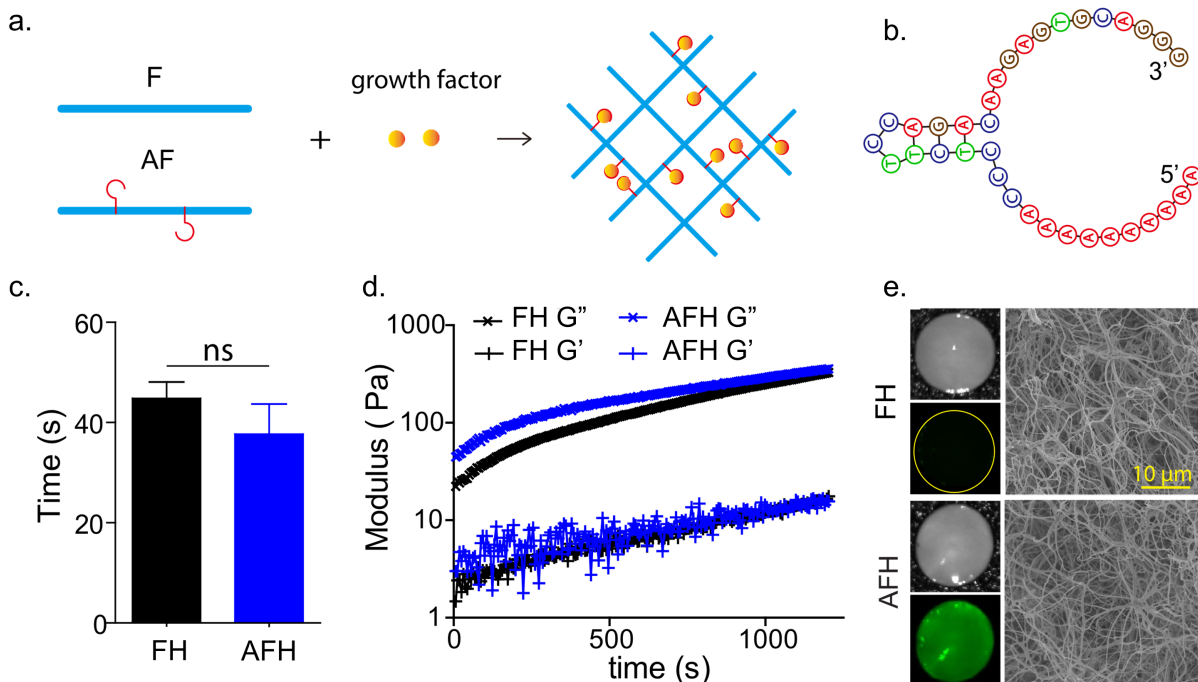


**Figure 2.** Evaluation of aptamer-functionalized fibrin hydrogel properties in comparison to native fibrin hydrogels. (a) Schematic illustration of functionalization synthesis, native fibrinogen (F); aptamer-functionalized fibrinogen (AF). (b) Secondary structure of the VEGF-binding aptamer. (c) Gelation time of FH and AFH,  $n \geq 3$ , ns = not significant. (d) Dynamic modulus.  $G'$  loss modulus;  $G''$ , storage modulus. (e) Representative images of hydrogels. Left: Optical images of bulk hydrogels (top) and images of hydrogels stained with SYBR Safe (bottom). Right: scanning electron microscopy images.

## RESULTS

### Aptamer Functionalization Prolongs Release of VEGF without Affecting Native Fibrin Hydrogel Material Properties.

This study used anti-VEGF DNA, an aptamer with a 37-nucleotide sequence (Figure 2b). Due to the small size of the aptamer, the conjugation of this aptamer to fibrinogen did not significantly affect the gelation time of the hydrogel, which is around 40 seconds (Figure 2c). The rheological evaluation showed that native FH and AFH exhibited similar mechanical properties as indicated by loss and storage moduli (Figure 2d). To confirm aptamer functionalization in the AFH, we stained the native FH and AFH with the complementary sequence followed with SYBR Safe. AFH showed strong green fluorescence, whereas native FH did not (Figure 2e). To further demonstrate that aptamer

functionalization did not affect the final hydrogel structure, we imaged the lyophilized hydrogels using scanning electron microscopy. Similar interconnected nanofibrillar networks were observed in both FH and AFH (Figure 2e), suggesting that the aptamer did not affect the structure of the final hydrogel.

We next examined short-term VEGF release kinetics from FH and AFH and quantified the effective diffusivity (Figure 3a–c). Aptamer functionalization significantly decreased the effective diffusivity of VEGF from  $0.49 \pm 0.04 \mu\text{m}^2/\text{s}$  to  $0.14 \pm 0.04 \mu\text{m}^2/\text{s}$  (Figure 3b). It is important to note that this calculation may significantly underestimate the aptamer mediated decrease of diffusivity because the VEGF molecules that are initially released might not be bound to the aptamers during AFH synthesis. Thus, we further examined the long-term release of VEGF from AFH (Figure 3c). At day 1, FH released approximately  $68 \pm 3\%$  of the total VEGF, whereas AFH released  $47 \pm 4\%$ . After 4 days, VEGF concentration was undetectable in the FH group, suggesting that all VEGF molecules were released within the first 72 hours to 96 hours. In contrast, we observed sustained VEGF release from AFH hydrogels over the next 10 days. Taken together, these data demonstrate that the aptamer functionalization prolonged the release of VEGF from the AFH.

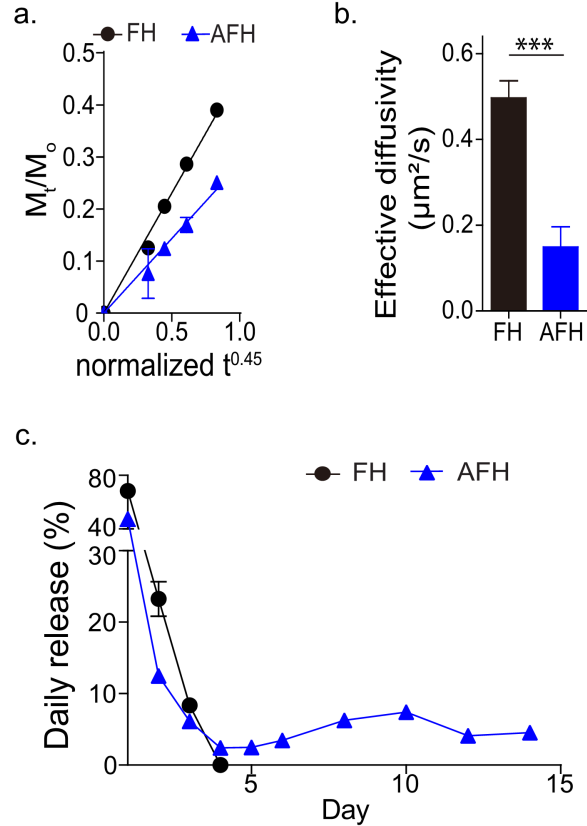


**Figure 3.** Evaluation of aptamer-functionalized fibrin hydrogel (AFH) and native fibrin hydrogel (FH) VEGF release kinetics. (a) Fractional VEGF release within the first 4 hours.  $M_t$  is the VEGF release at time  $t$ ;  $M_0$  is the initially loaded VEGF.  $M_t/M_0$  is the fractional release at time  $t$ . (b) Effective diffusivity calculated from a (c) daily release of VEGF.  $n \geq 3$ ,  $*** p < 0.05$ .

### Aptamer Functionalization with High Doses of VEGF Improves Angiogenesis Following Cranial Defect.

Vascular fraction was quantified as a percentage of total defect volume (Figure 4). Groups, 2.5AFH and 10AFH, showed a significant increase in overall vascularization. At 7 days, the 2.5AFH group had a significant 1.5-fold increase in percent vascularization over the non-hydrogel loaded control (Figure 4c) but did not have a significant increase compared to any other treatment group. At 21 days, 2.5AFH had a significant 2-fold increase compared to all other treatment groups, excluding the 10AFH group (Figure 4e). At this same time point, the 10AFH group showed a significant 2-fold increase compared to all treatment groups evaluated besides the 2.5FH and 2.5AFH groups (Figure 4e). Visual inspection confirmed successful perfusion with MICROFIL for all cranial

vasculature based on successful perfusion of the carotid arteries, as well as successful perfusion of the defect site (Figure 4a). Examination of the de novo vascularization within the defect, outlined in red in Figure 4a, with the surrounding vasculature removed, provides a clearer visualization of the variations in angiogenesis caused by each intervention. Removal of the surrounding vasculature reveals the increase in vascular formation in the 2.5AFH and 10AFH groups compared to all other treatment groups (Figure 4b), reaffirming the quantitative measures made previously.

Vessel density (vessels/micron) was significantly increased in the 2.5AFH group compared to the E treatment group after 7 days. We also observed an increase in both the 2.5AFH and 10AFH groups over time, reaching statistical significance at day 21 (Supplemental Information Figure S1). 2.5AFH and 10AFH groups showed a 68% and 257%, respectively, increase in vessel density from 7 to 21 days. From day 7 to day 21, an approximately 1-fold increase in vessel density was observed in the E treatment group, while a 20% decrease in density was observed in the FH group. At day 21, both the 2.5AFH and 10AFH groups displayed a 2-fold increase in vessel density relative to both the E and FH groups (Supplemental Information Figure S1c). The treatment groups receiving FH with VEGF at either concentration did not display a significant increase in the number of blood vessels formed compared to any other group evaluated. From day 7 to 21, we observed a 97% and 63% increase in vessel density in the 2.5FH and 10FH groups, respectively. AFH alone only showed a 66% increase in vessel density from day 7 to day 21.

We observed a significant decrease in vessel separation between the 2.5AFH and E treatment groups 7 days postoperatively, with a 2.5-fold reduction in the distance between vessels. An approximately 66% significant decrease in vessel separation was observed, in both the 2.5AFH and the 10AFH groups, compared to the non-hydrogel loaded control, 21 days post-hydrogel introduction (Supplemental Information Figure S1f). The average distance between vessels 21 days postoperatively was 217 $\mu$ m and 193 $\mu$ m in the 2.5AFH and 10AFH groups, respectively. The non-hydrogel loaded control defect had an average distance of 645 $\mu$ m between vessels 21 days after hydrogel introduction, while the FH,



2.5FH, and 10FH with groups had an average distance of 577 $\mu$ m, 319 $\mu$ m, and 358 $\mu$ m between vessels, respectively. The AFH group had an average separation of 350 $\mu$ m between vessels 21 days after hydrogel introduction, which was not significantly different than the 517 $\mu$ m separation observed with FH. At no other time point was the separation between the vessels significant for any treatment group (Supplemental Information Figure S1d, e).

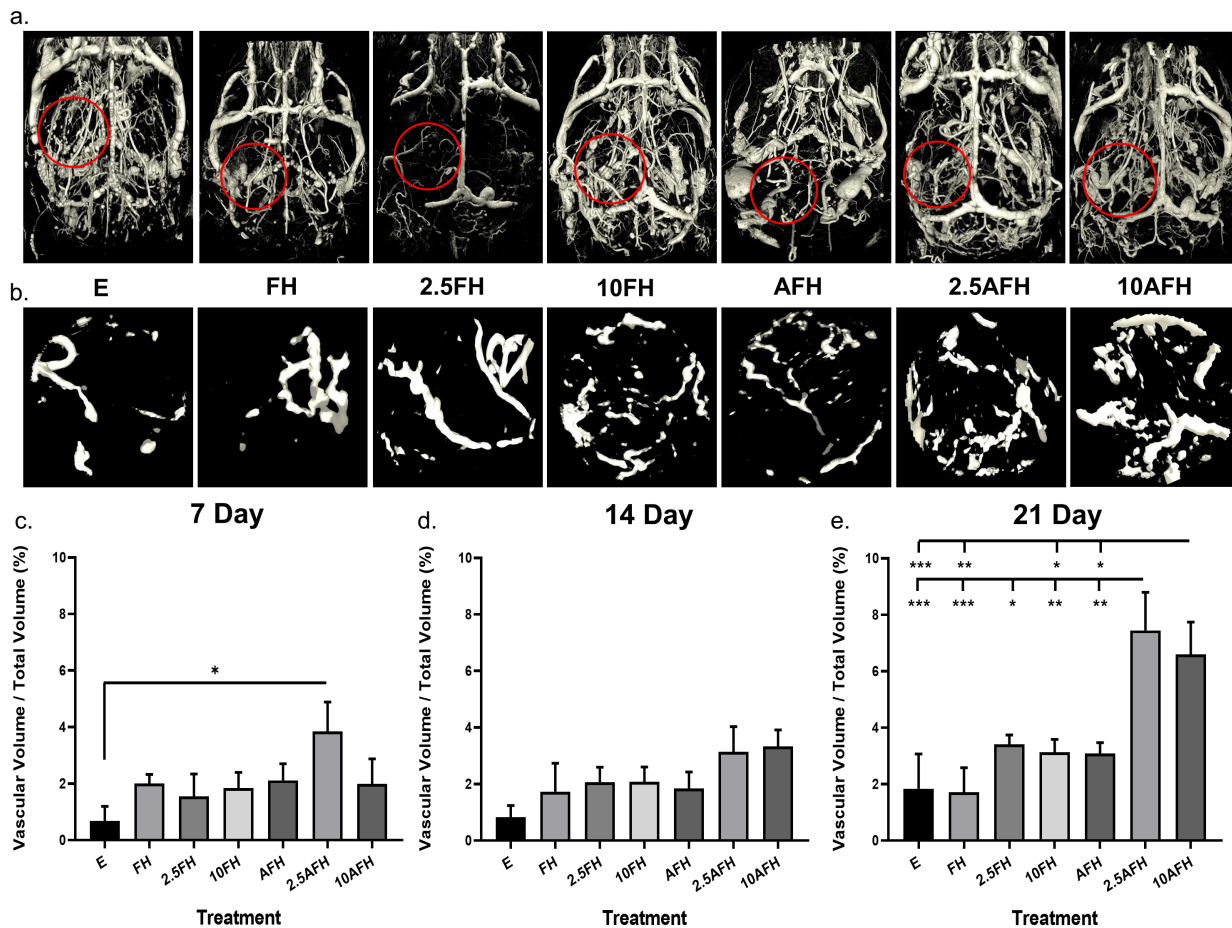


**Figure 4.** Total vascularization within the defect volume as a result of hydrogel treatment. (a) A representative image of the total skull vascularization for each intervention 21 days post defect introduction. (b) Enhanced view of the vascularization within the defect region outlined in red in part (a) for each intervention 21 days post defect introduction. Micro-CT analysis of the percent vascularization (vascular volume/total defect volume) of the defect at (c) 7 days post defect introduction for all intervention types, (d) 14 days post defect introduction for all intervention types, and (e) 21 days post defect introduction for all intervention types. \*  $p < 0.05$ , \*\*  $p < 0.005$ , \*\*\*  $p < 0.001$ ,  $n \geq 3$ .



### **Aptamer Functionalization with High Doses of VEGF Improves Osteogenesis Following Cranial Defect.**

The non-hydrogel loaded control group showed minimal de novo bone formation in the defect site by day 21 (Figure 5). Seven days post-hydrogel introduction, no treatment group, AFH or FH with or without VEGF, was significantly different from the non-hydrogel loaded control defect or any of the other treatments evaluated (Figure 5a). However, at 14 days, the 10AFH group showed significantly greater BV/TV than all other treatment groups, except AFH (Figure 5b). At 21 days postoperatively, BV/TV increased 3.8-fold (from 0.75% to 2.92%) in the 10AFH treatment group compared to the non-hydrogel loaded control group (Figure 5c). Qualitative visualization of bone formation and healing confirms the quantitative analysis, showing a significant decrease in defect size in the 10AFH group 14 days after hydrogel introduction compared to all treatment groups besides AFH. Additionally, there was a slight decrease in defect size in the 10AFH group compared to the FH treatment groups 21 days postoperatively and a significant decrease in defect size compared to E (Figure 5d).

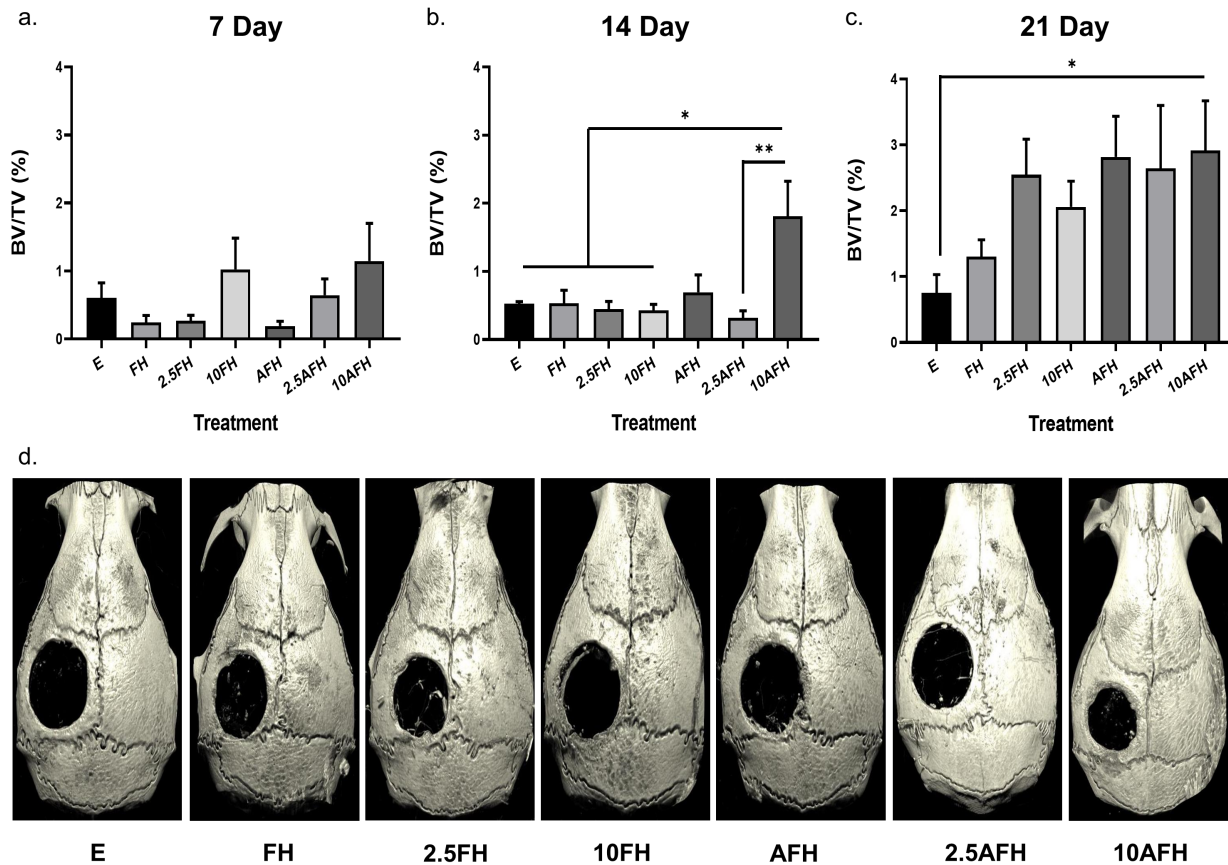


**Figure 5.** Analysis of bone healing in critical sized cranial defect. (a) Micro-CT analysis of the percent bone volume (bone volume/total defect volume, BV/TV) at 7 days post defect introduction for all intervention types, (b) 14 days post defect introduction for all intervention types, and (c) 21 days post defect introduction for all intervention types. (d) Representative images of each experimental group 21 days post defect introduction. \* $p < 0.05$ , \*\*  $p < 0.005$ ,  $n \geq 3$ .

## DISCUSSION

The design and use of novel biomaterials for bone healing applications, especially in large bone defects, is of critical importance due to increasing rates of disease, disuse, and injury<sup>92</sup>. Hydrogels loaded with growth factors have proven to be effective in treating smaller bone defects, but critical sized bone defects have proven challenging to treat, because of the inadequate release kinetics associated with most hydrogels<sup>83,86</sup>. To address this problem, we developed a novel AFH loaded with VEGF, and used it to treat a critical sized cranial defect in mice. Our results show that this novel hydrogel increases

the sequestration and retention of VEGF compared to FH. More importantly, this improvement in VEGF kinetics in AFH, relative to FH, was able to promote greater vascularization and osteogenesis in a critically sized calvarial defect, suggesting AFH is a promising avenue for clinical wound healing applications.

The results of this study show that we can successfully increase VEGF incorporation and retention by utilizing an anti-VEGF aptamer while maintaining mechanical and structural properties similar to those of native fibrin hydrogel (Figures 2 and 3). AFH maintained a similar elastic and viscous response as well as similar morphological properties to FH<sup>93-95</sup>. The literature has shown that the physical properties of FH facilitate wound healing. FH alone promotes and aids in cell proliferation, differentiation, and migration, all of which are necessary for healing critical sized defects<sup>96</sup>. The mechanical properties of FH also allow for the proper stability to support angiogenesis; therefore, maintaining similar physical properties to FH with AFH is highly desirable<sup>97</sup>. In addition to maintaining similar physical and mechanical properties to FH, AFH improves the fractional release of VEGF over an initial 4-hour period, diminishes diffusivity, and significantly elongates, compared to FH, measurable VEGF release over 14 days. Our results, corroborated by previous studies with AFH, also show a diminished burst release and an elongated release profile through the use of VEGF-specific aptamers<sup>83</sup>. The improved release kinetics of AFH and diminished diffusivity also suggest that AFH not only maintains VEGF release over a longer period but also improves VEGF localization and bioavailability at the defect site. Previous studies have shown VEGF is not only important in the promotion of vascularization but also critical in the facilitation of bone formation by recruiting mesenchymal stem cells, activating osteoblast differentiation, and promoting mineralization<sup>98</sup>. Due to the typical release kinetics exhibited by most hydrogels including FH, VEGF is not localized to the defect long enough to facilitate bone healing, which typically begins 2–3 weeks postinjury<sup>79,99</sup>. Although this issue lacks a complete resolution, even with the use of AFH, the extended diffusivity still has significant implications for bone healing. Previous studies have shown that between 7 and 10 days, the presence of VEGF enhances mesenchymal stem cell recruitment and survival, with VEGF playing a synergistic role with bone morphogenic protein-4 (BMP4), resulting in a significant

increase in bone formation after 28 days compared to situations where VEGF was not present<sup>78,95</sup>. This suggests that by using AFH, the extended diffusivity and localization of VEGF will enhance bone formation.

The effects of the improved incorporation and release of VEGF observed in vitro were validated in vivo. An overall increase in vascularization was observed 21 days after hydrogel introduction for AFH compared to all FH treatment groups (Figure 4). Groups receiving AFH loaded with VEGF showed significant changes in vessel separation and vessel density compared to nontreated defects (Figure 3). Similar to previous studies, there was an inverse correlation between the observed increase in vessel density and decrease in vessel separation, validating both measurements, with R-values ranging between  $-0.6901$  and  $-0.9736$  (Data not shown)<sup>100</sup>. Both vessel density and vessel separation are critical for the successful healing of critical sized bone defects because of the hypoxic environment created in most such bone defects<sup>101,102</sup>. Because of the size of critical defects, diffusion is often the rate limiting factor. Unless the vessels achieve anastomosis, proper intramembranous ossification and bone remodeling, necessary for a successful repair, are highly unlikely<sup>98,103</sup>. This is because the hypoxic environment needs to be relieved for mesenchymal stem cells to infiltrate the defect site and begin the intramembranous ossification process<sup>88,104,105</sup>.

Our data also suggest the effect AFH with VEGF has on vascularization may be underestimated. Vessel density and vessel separation (Supplemental Information Figure S1) are measures of only mature vessels or vessels that have undergone anastomosis. Overall vascularization accounts for total vessel volume regardless of maturity and interconnection (Figure 4). The observed changes in overall vascularization were of greater significance than the changes we observed in vessel density and number. This increase in overall vascularization suggests that more vessel anastomosis may occur if this study investigated vascularization at longer time points since some vessels may have yet to reach maturity at the time points currently evaluated. Alternatively, we are aware of the limitations of MICROFIL and its limited perfusion in vessels less than  $10\mu\text{m}$  in diameter<sup>106</sup>. However, this limitation would underestimate the effect of AFH with VEGF

has on vasculogenesis, as it may not have allowed quantification of all newly formed vessels that are less than 10 $\mu$ m in diameter. Thus, this would not change the interpretation of our results.

In vivo evaluation shows a moderate increase in bone healing 14 days postoperatively between the 10AFH treatment group compared to the empty and FH treatment groups. An observable difference was only seen between the 10AFH and empty treatment groups 21 days postoperatively (Figure 5); however, there were no differences observed between the treatment groups at 7 days. Although there was a trend at day 7, suggesting the 10FH and 10AFH groups were inducing greater bone formation, the variance between samples as well as limited sample size did not yield significant differences. The lack of greater significance in bone healing, relative to vascularization, may also be due to the time points evaluated in this study. Because this study aimed to evaluate the properties and release kinetics of AFH and how these may affect vascularization, we evaluated earlier time points than those typically used in bone healing studies<sup>106,107</sup>. This prevents bone healing from being characterized fully within the scope of this study, as the bone formation process can take up to 3 months, and vascularization occurs rapidly over the first 3 weeks<sup>108–110</sup>. Despite this, information gathered 14 and 21 days postoperatively suggests AFH with VEGF has improved bone formation and healing, a trend that would likely continue at later time points.

Although VEGF is known as an important growth factor in angiogenesis and osteogenesis, intramembranous bone healing is highly complex and utilizes numerous growth factors and chemokines. Because of this, codelivery of multiple factors, such as platelet-derived growth factor and bone morphogenic protein-2 (BMP2), has been studied extensively using other biomaterial systems with varied success<sup>7,109</sup>. The specificity of the aptamers used in our AFH system would allow for codelivery of multiple growth factors, allowing for improved healing and a more targeted approach to wound healing. Therefore, AFH is of significant interest for future biomedical applications. The high affinity and specificity of aptamers allow for multiple factors to be investigated simultaneously and various steps in the intramembranous healing process to be promoted. Our AFH system

would allow for the development of a proactive and targeted approach for critically sized bone defects.

## **CONCLUSION**

This study shows the ability to successfully engineer a functionalized anti-VEGF aptamer into native fibrin and then into AFH. These hydrogels showed no significant changes in structural or mechanical properties compared to FH alone, based on the rheological assessment and nanoscale surface (scanning electron microscopy) evaluation. The AFH showed enhanced retention and release profile of VEGF in vitro, extending the release of VEGF for more than a week longer compared to native FH without aptamer functionalization. Engineered AFH loaded with 10  $\mu\text{g/mL}$  of VEGF enhanced bone formation 14 days postintervention compared to the FH treatment groups and empty controls, but this increase was not observed 21 days postintervention compared to the FH treatment groups. Additionally, the novel hydrogels loaded with VEGF at both concentrations showed a greatly increased ability to induce angiogenesis, increasing vessel density, reducing the separation between blood vessels, and greatly increasing overall vascularization compared to the FH and non-hydrogel loaded defects. The study revealed that AFH, relative to nonfunctionalized FH, has a greater release and retention profile of VEGF, improved bone reparative effects, and induced increased vasculogenesis while maintaining similar structural and mechanical properties to nonfunctionalized FH. This evidence suggests that our AFH could have a considerable clinical application for bone regeneration.

## **CHAPTER 4. Effect of Carbonated Hydroxyapatite Submicron Particle Size on Osteoblastic Differentiation**

Authors:

Otto J. Juhl IV, Seyed Mohsen Latifi, Henry J. Donahue

*Journal of Biomedical Materials Research Part B: Applied Biomaterials, 2021, 11, 1-11*

## **ABSTRACT**

Synthetic biomimetic carbonated hydroxyapatite (CHA) has shown significant promise in bone tissue engineering for its mechanical and chemical biocompatibility and osteogenic potential. Variations in the size of hydroxyapatite particles have also been shown to contribute to the hydroxyapatite's osteogenic success. However, synthesizing biomimetic CHA with optimal osteogenic properties using a simple synthesis methodology to make highly reproducible, biomimetic, and osteogenic CHA has not been evaluated fully. The objective of this study was to synthesize submicron CHA particles using a nanoemulsion method. We hypothesized that by varying the synthesis technique we could control particle size while still creating highly biomimetic CHA typically produced during nanoemulsion synthesis. Furthermore, we hypothesized that 500 nm CHA particles would induce greater osteoblastic differentiation compared to larger or smaller CHA particles. X-ray diffraction, Fourier transform infrared spectroscopy, scanning electron microscopy, and dynamic light scattering were used to characterize the chemical composition, shape, and size of CHA synthesized through variations in pH, temperature and stirring speed during synthesis. Manipulation of pH showed the ability to selectively tailor CHA particle size from 200 nm to 900 nm in a reproducible manner while maintaining the chemical composition. In addition, 500 nm particles elicited the most rapid increase in osteoblastic differentiation and did not decrease cell viability compared to 200 and 900 nm particles.

## **INTRODUCTION**

The use of synthetic biomimetic carbonated hydroxyapatite (CHA) for bone tissue engineering has been evaluated in great depth over the last 20 years. As the main inorganic phase of bone, hydroxyapatite is comprised of two main constituents, calcium and phosphorus, at a stoichiometric ratio of 1.67 Ca/P. Biological hydroxyapatite exhibits a rod-shaped morphology, has a crystallite size ranging from 5–200nm, a crystallinity between 60% and 80%, and agglomerates into larger particles that exist on the micron scale<sup>110,111</sup>. Biological hydroxyapatite, being a ceramic, also has high-compressive strength and significant osteoconductive properties that allow it to create a mechanically



stable matrix<sup>111</sup>. Because of these favorable qualities, synthesis of synthetic hydroxyapatite that can be utilized in bone tissue engineering applications has been extensively studied.

As a result of the extensive examination into hydroxyapatite synthesis, it was determined that the size and shape of hydroxyapatite particles resulted in significant variations in the apatite's overall osteogenic potential<sup>112–114</sup>. Previous studies have shown that the use of submicron hydroxyapatite particles increases the apatite's overall osteogenic properties both *in vitro* and *in vivo*<sup>111,115</sup>. This may be a result of various submicron topographies, including particle shape, size, and surface features, differentially affecting osteogenesis<sup>7,9,116–118</sup>. For example, submicron hydroxyapatite particles synthesized by Kalia *et al.* determined that “rice” shaped particles were far less effective than round particles at inducing osteoblastic differentiation and preventing cell apoptosis<sup>119,120</sup>. The majority of other studies examining the effect of hydroxyapatite particle shape on osteogenesis have corroborated this observation, suggesting that despite natural apatite's rod-like morphology; rod-shaped synthetic hydroxyapatite does not elicit the greatest osteogenic response<sup>121</sup>. Instead, spherical hydroxyapatite is more conducive to cell viability and osteogenesis<sup>122</sup>.

Despite the consensus as to which shape of CHA particle best promotes osteogenesis, the size of the particle that best promotes osteogenesis is still not agreed upon. Numerous studies by our group and others have shown the importance of surface topography in promoting osteogenesis<sup>123</sup>. One way in which surface topography can be modified is through incorporation of various sizes of nano and submicron particles into a bone implant or scaffold<sup>124</sup>. However, conflicting results as to which size hydroxyapatite particle is most osteogenic has hindered the fabrication of synthetic bone grafts incorporating hydroxyapatite particle of optimized size<sup>125</sup>. For example, a study by Yang *et al.* evaluated submicron hydroxyapatite particles and their effect on osteogenesis. They determined that roughly 570nm hydroxyapatite particles were optimally osteogenic<sup>125–127</sup>. However, a study by Cai *et al.* observed an increase in osteogenesis on 20nm hydroxyapatite particles<sup>18,128</sup>. Additional studies have noted that larger features, 500nm to 700nm pillars,

reduced apoptosis and increased osteogenesis to a greater degree than smaller features of roughly 200nm<sup>127,129</sup>. These results illustrate the vast range of hydroxyapatite particle sizes that can increase osteogenesis, thus highlighting the challenge of identifying optimally osteogenic particles based on published results alone. The lack of agreement on what hydroxyapatite particle size induces the greatest osteogenic response makes it challenging to reproducibly and easily create hydroxyapatite particles that will be optimally osteogenic.

Successful attempts have been made at creating synthetic biomimetic hydroxyapatite with a variety of methodologies ranging from wet precipitation to chemical synthesis methods<sup>130</sup>. Variations within each method allows for the creation of chemically pure CHA with a range of sizes, shapes, distributions, and costs of synthesis. These various synthesis methods have been examined extensively and summarized in numerous reviews<sup>18,131,132</sup>.

Microemulsion, dry synthesis and chemical synthesis are all challenging to use. This can be because of various factors including not consistently creating a controlled particle size and shape, implementing harsh chemicals for synthesis, requiring extreme conditions such as high temperatures or surfactants, or a combination of one or more of these factors<sup>124,129</sup>. These syntheses methods necessitate extensive purification and washing to make the synthesized hydroxyapatite suitable for biological applications and to maintain a narrow particle size distribution, with even commercially available hydroxyapatite particles not maintaining a narrow distribution<sup>18</sup>. Because of these challenges, there is a need for simple, consistent methods for synthesizing CHA particles within the submicron range and evaluating their osteogenic potential.

In this study, we utilized a nanoemulsion synthesis methodology based on techniques created by Nelson and Featherstone<sup>18</sup>, but as modified by others<sup>18,125,126,129,133</sup>. This process is favorable because it does not require harsh chemicals, is highly reproducible, rapid, and produces spherical particles on the submicron scale. We hypothesized that by modifying this nanoemulsion synthesis methodology through the manipulation of

temperature, pH, and homogenization speed we can selectively tailor the size of CHA particles. Based on previous studies of cell response to various substrate features such as particle size and nanopillars<sup>18</sup>, we hypothesize that the synthesized CHA particles would be biocompatible and that 500 nm CHA particles would elicit the greatest osteogenic response in vitro.

## **MATERIALS AND METHODS**

### **Materials.**

All chemicals used for nanoparticle synthesis were obtained from Sigma-Aldrich (St. Louis, MO). Chemicals used for nanoparticle characterization were obtained from Thermo Fisher Scientific (Waltham, MA)

### **Carbonated Hydroxyapatite Synthesis.**

#### *Standard Submicron Carbonated Hydroxyapatite Particle Synthesis.*

Submicron CHA particles were synthesized following methods described previously<sup>125,126</sup>. Briefly, the calcium source (calcium nitrate tetrahydrate) was dissolved in 5 ml acetone and stirred for 30 minutes at a standard temperature of 21°C while the phosphate source (hydrogen phosphate and ammonium bicarbonate) was dissolved in 5 ml ultrapure water, brought to the standard pH of 11 using a 1 M NaOH solution, and stirred for 30 minutes at the desired temperature of 21°C. The calcium source was then added into the phosphate source rapidly and allowed to homogenize for 30 sec at the standard of 500RPM before 50 ml of ultrapure water was added to the slurry to quench the reaction and homogenization discontinued. The slurry was then vacuum filtered and rinsed with 1 L of ultrapure water. The paste that remained after filtration was then removed and dried for 24 hours at 80°C. The resulting dried CHA was then ball milled at a 20:1 bearing weight to dried CHA weight ratio using a 4.05 g stainless steel bearing at 1000RPM for 1 hour yielding a powder with submicron particles. This powder was then heat-treated at 600°C for 30 minutes with a ramp rate of 5°C min<sup>-1</sup>.

The standard values for synthesis of the CHA throughout this study were pH 11, 21°C, and 500 RPM. These values were determined based on the methods described previously<sup>129,133,134</sup>. Using these standard values, a reproducible CHA was generated. The effects of each variable; pH, temperature, or RPM were then manipulated individually while maintaining the standard values of the other two variables to effectively characterize how manipulation of pH, temperature, or RPM individually would affect particle size, crystallite morphology and chemical composition.

#### *pH Variant Submicron CHA Particle Synthesis.*

pH variant CHA was created following a procedure identical to that listed above with variation occurring as to the desired pH obtained in the phosphate source (Table 3). Again, using 1 M NaOH, the phosphate sources were brought to a pH of either pH 10, pH 11, or pH 12 before being stirred for 30 seconds at the standard temperature of 21°C and 500 RPM. The paste resulting from calcium source introduction and filtration was then dried for 24 hours at 80°C, ball milled at 1000RPM for 1 hour then heat-treated yielding a powder.

The pH values that were used in this study were determined from a review of previous literature<sup>18,135,136</sup>. To yield what we hypothesized would be the greatest distribution of size between experimental groups, while creating biomimetic CHA, we evaluated the nanoemulsion methodology at the extremes of pH 10 and pH 12 and at the median value of pH 11. We chose a value of pH 11 because it was examined in previous studies where CHA was created and was shown to reliably create CHA particles<sup>18</sup>. However, pH values less than 10 resulted in rod-like particles that were not conducive to cell growth<sup>135</sup>, and values greater than 12 resulted in poor control over the distribution of particle size as well as a crystallinity higher than typical biological apatite<sup>135,136</sup>.

**Table 3.** Synthesis parameters for each CHA variant

Variant Group Synthesized		pH	Temperature (°C)	Homogenization Speed (RPM)	Abbreviation
pH	pH 10	pH 10	21°C	500 RPM	PH10
	pH 11	pH 11	21°C	500 RPM	PH11
	pH 12	pH 12	21°C	500 RPM	PH12
Temp	4°C	pH 11	4°C	500 RPM	T4
	21°C	pH 11	21°C	500 RPM	T21
	55°C	pH 11	55°C	500 RPM	T55
RPM	200 RPM	pH 11	21°C	200 RPM	R200
	500 RPM	pH 11	21°C	500 RPM	R500
	800 RPM	pH 11	21°C	800 RPM	R800

*Homogenization Speed (RPM) Variant Submicron CHA Particle Synthesis.*

RPM variant CHA was created following a procedure identical to that listed above with variation occurring during the homogenization speed of the phosphate and calcium source (Table 3). Again, the calcium source and phosphate source were synthesized as described above at the standard values of 21°C and a pH of 11. When the calcium source was added to the phosphate source the homogenization speed (RPM) was manipulated to either 200 RPM, 500, RPM or 800 RPM for 30 seconds before water was introduced and the stirring discontinued. The paste resulting from calcium source introduction and filtration was then dried for 24 hours at 80°C and then ball milled at 1000 RPM for 1 hour and heat-treated yielding a powder.

The homogenization speeds that were used in this study were determined from a review of previous literature<sup>18,136–138</sup>. A homogenization speed of 500 RPM being the value examined in previous studies that created CHA<sup>18</sup>. It was determined by Salimi *et al.* that higher agitation rates, those above 1200 RPM, would begin to produce elongated hydroxyapatite particles but decreased the overall size consistency of the particles formed, whereas lower rates allowed for a more controlled particle size<sup>136</sup>. It was also found that slower agitation speeds below 200 RPM resulted in cuboid shaped hydroxyapatite particles, which based on previous literature, would be less osteogenic and therefore less favorable<sup>138</sup>. Therefore, we evaluated the homogenization speeds of

200 RPM, 500 RPM, and 800 RPM to maintain what we hypothesized would be spherical CHA, while maintaining a high reproducibility of CHA during synthesis.

#### *Temperature Variant Submicron CHA Particle Synthesis.*

Temperature variant particles CHA was created following a procedure identical to that listed above with variation in the temperature at which the solutions were maintained and mixed (Table 3). Again, the calcium and phosphate source were synthesized as described above at the standard value of pH 11 but were maintained at either 4°C, 21°C, or 55°C, verified by handheld thermometer, before the addition of the calcium source to the phosphate source, throughout the entirety of the synthesis process. The paste resulting from calcium source introduction, after 30 seconds of stirring at the standard value of 500 RPM and filtration, was then dried for 24 hours at 80°C and then ball milled at 1000 RPM for 1 hour and heat-treated thus yielding a powder.

The temperature values that were used in this study were determined from a review of previous literature<sup>136</sup>. A temperature of 21°C, was used in previous studies that had created CHA<sup>137,139</sup>. A study by Elhendawi *et al.* reported synthesis of hydroxyapatite at -10°C, 37°C, and 60°C using a coprecipitation methodology. They determined that increasing temperature allowed for greater hydroxyapatite crystallinity as well as larger particle sizes. In addition, increasing the temperature over 60°C resulted in less control over hydroxyapatite size and shape<sup>140,141</sup>. Others have reported successful synthesis of hydroxyapatite particles at 50°C, although the crystallinity and morphology were not conducive to osteogenesis<sup>142</sup>. Furthermore, Eldendawi *et al.* determined that hydroxyapatite synthesized at -10°C has low crystallinity, roughly 10%, a percentage significantly lower than biological apatite<sup>143</sup>. Additional studies have reported apatite with a crystallinity more similar to biological hydroxyapatite when using temperatures between 0°C and 5°C<sup>143</sup>. For these reasons, we used 4°C, 21°C, and 55°C to prepare our CHA. We hypothesized that this would allow the creation of CHA with biomimetic crystallinity and maintain the spherical morphology desired.

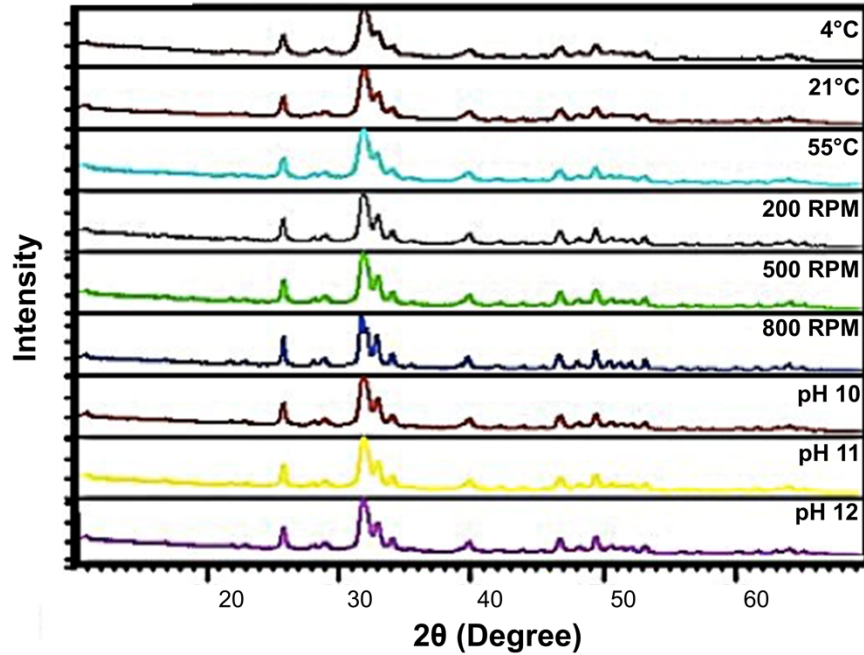


**Figure 6.** XRD showing each CHA variant with similar phase characteristics. XRD spectra of all synthesized CHA variants showing similar phase characteristics and intensities.

### CHA characterization.

#### *X-ray Diffraction Analysis.*

The phase composition, crystallite size and crystallinity of prepared samples were analyzed by X-ray diffraction (XRD, X'Pert Pro PANAnalytical) using a CuK $\alpha$  radiation generated at 45 kV and 40 mA from 10° to 70° with a step size of .026° (2 $\theta$ ), a speed of .016°/second, and a time of 4 seconds per step. Crystallite diameter responsible for the (002) plane was calculated using the Scherrer relationship shown in Equation 2<sup>144</sup>.

$$\tau = (\kappa\lambda)/(\beta\cos\theta) \quad \text{Equation 2}$$

where  $\kappa$  is the dimensionless shape factor of 0.9,  $\lambda$  is the wavelength of the X-ray (0.15918 nm),  $\beta$  is the full width at half maximum for the diffraction peak under consideration (rad),  $\theta$  is the diffraction angle (°), and  $\tau$  is the mean crystal size in nanometers<sup>145</sup>. The crystallinity fraction ( $X_c$ ) was calculated using Equation 3<sup>145</sup>.

$$X_c = 1 - (V_{112/300}/I_{300}) \quad \text{Equation 3}$$

where  $V_{112/300}$  is the intensity of the peak area between (112) and (300) and  $I_{300}$  is the intensity of the (300) reflection peak<sup>106</sup>.

#### *Fourier Transform Infrared Analysis.*

Examination of chemical group composition and formation of each variant of CHA was performed using Fourier transform infrared spectroscopy (FTIR) (Nicolet–Nexus 670 FT-IR) with a flat diamond cell probe. Absorbance was gathered over the wavelength spectrum from  $400\text{ cm}^{-1}$  to  $4000\text{ cm}^{-1}$ .

#### *Scanning Electron Microscopy Analysis.*

CHA morphology was examined using scanning electron microscopy (SEM, Hitachi FE SEM Su-70). A 0.02 mg/ml solution of CHA and analytical grade ethanol was created and sonicated for 10 minutes. 10 $\mu$ L of the CHA solution was then placed on a pure silica wafer and the ethanol allowed to evaporate. The remaining CHA particles deposited on the surface of the wafer were then platinum sputter coated for 60 seconds to generate a 2 Å coating. The samples were then imaged using a 5 kV acceleration voltage and a 5 mm working distance.

#### *Dynamic Light Scattering Analysis.*

Particle size of CHA was analyzed using dynamic light scattering (DLS) (Zeta Sizer Nanoseries Nano-zs90, Malvern). A 0.01 mg/ml solution of CHA in analytical grade ethanol was created. Immediately before analysis, each suspension was vortexed briefly then sonicated for 10 minutes before 1 ml of the CHA solution was placed into a cuvette and analyzed. Thirty collections were performed per measurement and each sample measurement was repeated three times. The three replicates were then averaged to determine the average CHA particle diameter.



### ***In vitro* characterization.**

#### *Cell Viability Assay.*

hFOB 1.19 cells, a human preosteoblastic cell line, were cultured at 30,000 cells per well in a 24 well tissue culture polystyrene (TCPS) plate. Cells were cultured under proliferative conditions at 33.5°C and 5% CO<sub>2</sub> and Dulbecco's Modified Eagle Medium: Nutrient Mixture F-12 media (Thermo Fisher Scientific, Waltham, MA) supplemented with 10% fetal bovine serum (FBS) and 1% penicillin streptomycin (Gibco, Gaithersburg, MD). After 24 hours, a 0.02 mg/ml solution of CHA and standard growth media was created. The suspension was then vortexed briefly and sonicated for 10 minutes before 250 ul of the various media and CHA suspensions were added to the respective wells. Cells were then incubated in proliferative conditions with the media and CHA suspension for 48 hours. Following incubation, cell viability was quantified using a ReadyProbes Cell Viability Imaging Kit (Thermo Fisher Scientific, Waltham MA). The cells were then imaged for either blue stain (all cells) or green stain (dead cells) using an EVOS microscope. The images were then quantified using Fiji image analysis software<sup>18,139,146</sup>.

#### *Particle Effect on Osteoblast Differentiation.*

For the following, because no variation in CHA chemical composition was determined between the pH, temperature or homogenization variants, only particles synthesized using the pH synthesis methodology were used to evaluate the effect of CHA size on osteoblastic differentiation. This is because pH synthesis was the only methodology that allowed significant manipulation of particle size. hFOB 1.19 cells were cultured at 30,000 cells per well in a 24 well TCPS plate in differentiation conditions at 33.5°C in Dulbecco's Modified Eagle Medium: Nutrient Mixture F-12 media (Thermo Fisher Scientific, Waltham, MA) supplemented with 10% FBS, 1% penicillin streptomycin (Gibco, Gaithersburg, MD), 100 ug/ml ascorbic acid, and 100uM Vitamin-D3 for 24 hours. A 0.02mg/ml CHA and differentiation media solution was created using CHA synthesized with either the pH 10, pH 11, or pH 12 methodology. Immediately before use the solutions were vortexed briefly and sonicated for 10 min. The media in each well was then replaced with the respective solution of either pH 10, pH 11, or pH 12 CHA and media and cultured for 7 days under differentiation conditions. The media was changed every 3 days. At 1, 3, and 7 days after

the addition of the media and CHA suspension, whole cell protein lysate was collected, and cellular alkaline phosphatase (AP) enzymatic activity was quantified as previously described<sup>18</sup>. Briefly, cells were freeze thawed in 400 $\mu$ L of 0.05% Triton-X100 in phosphate buffered saline twice and then the cell lysate collected. 10 $\mu$ L of each sample lysate was removed and used to quantify total protein concentration using Pierce BCA protein assay kit (Thermo Fisher, Waltham, MA). AP enzymatic activity was then determined by conversion of p-nitrophenyl phosphate to p-nitrophenol. 200 $\mu$ L of AP reaction buffer was then added to each sample and incubated at room temperature for 30 minutes. After incubation 50 $\mu$ L of each sample was moved to 200 $\mu$ L of 0.1 NaOH in a 96 well plate to quench the reaction. All samples were then measured at 410nm and SIGMA units calculated based on the standard curve. All readings were then normalized to total protein concentration to control for variations in cell number between samples.

#### *Conditioned Media Effect on Osteoblast Differentiation.*

For the following, because no variation in CHA chemical composition was determined between the pH, temperature or homogenization variants, only particles synthesized using the pH synthesis methodology were used to evaluate the effect of CHA size on osteoblastic differentiation because pH allows significant variations in particle size to be achieved during synthesis. A 0.02mg/ml CHA and differentiation media solution was created. The media was then conditioned for 7 days at 4°C with the CHA under gently agitation. After 7 days, the conditioned media was sterile filtered using a 0.11 $\mu$ m filter to remove all CHA particles. hFOB 1.19 cells were then cultured at 30,000 cells per well in a 24 well TCPS plate for 24 hours. After 24 hours the differentiation media was replaced with conditioned media. The cells were then cultured under differentiation conditions and the conditioned media changed every 3 days. 1, 3, and 7 days after the addition of conditioned media, whole cell protein lysate was collected, and AP activity quantified as previously described<sup>137-139</sup>.

#### **Statistical Evaluation.**

Variations in crystallite size and crystallinity were assessed with a two-way ANOVA followed by Tukey's post hoc analysis and are reported as mean  $\pm$  SD. Variations in

particle size were assessed using an unpaired t-test followed by Bonferroni post-hoc analysis and are reported as mean  $\pm$  SEM. Variations in cell viability were assessed with a two-way ANOVA and are reported as mean  $\pm$  SD. Post-hoc analysis was not performed on cell viability data. Osteoblastic AP activity after particle or conditioned media exposure was assessed using two-way ANOVA followed by Tukey's post hoc analysis and are reported as mean  $\pm$  SD. All analysis was performed using GraphPad Prism version 8.1.1 for Windows (GraphPad Software, La Jolla CA). p-values  $<$  0.05 were considered statistically significant.

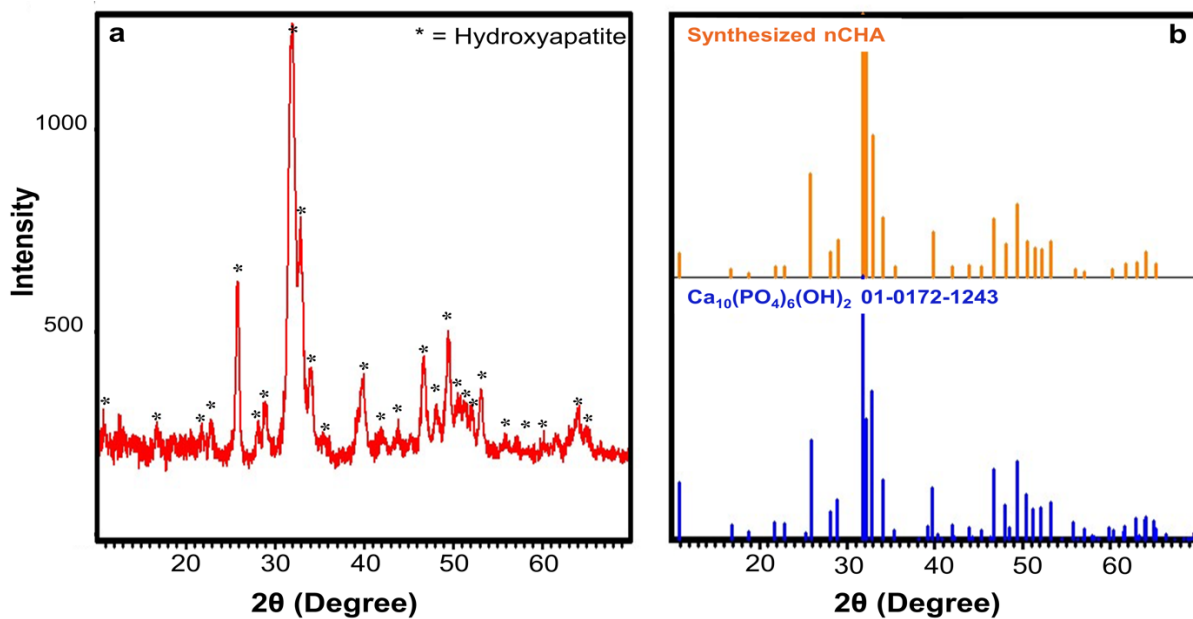


**Figure 7.** XRD spectra confirming synthesis of carbonated hydroxyapatite. (a) XRD spectra of representative CHA synthesized via the T4 method with significant carbonated hydroxyapatite peaks labeled. (b) Comparison of XRD spectra of representative CHA synthesized via the T4 method and standard (01–0172-1,243) hydroxyapatite.

## RESULTS

### Variation in Synthesis Methodology does not Affect Particle Composition or Morphology.

XRD analysis of each CHA variant showed that all variants had similar spectra (Figure 6). The similarities between the peaks of each CHA variant suggests that the changes in

synthesis methodology did not alter the crystallinity or phase composition of the respective samples. In addition, a representative sample of CHA, synthesized using the T4 methodology, is compared to that of standard CHA (01–0172–1243) in Figure 7b. Similar peaks of the CHA and CHA variant are labeled in Figure 7a. Crystallinity percentage of each CHA variant was then quantified using the observed spectra with degree of crystallinity ranging from roughly 60% to 88% (Table 4).

**Table 4.** CHA crystallite size and crystallinity of all synthesized CHA variants. n = 3 samples with each sample being the average of 3 measurements. Groups not sharing the same letter are significantly different ( $p < 0.05$ ) within the same column.

Variant Group Synthesized		Crystallite Size (nm)	Crystallinity (%)
pH	pH 10	27.7 ±1.5	65.6%
	pH 11	23.9±1.4	64.1%
	pH 12	25.4±1.3	62.0%
Temp	4°C	24.0±5.1	84.0% <sup>a</sup>
	21°C	23.9±3.6	78.4% <sup>a</sup>
	55°C	20.8±2.4	88.8% <sup>a</sup>
RPM	200 RPM	24.2±1.6	60.5%
	500 RPM	24.6±0.6	61.6%
	800 RPM	25.4±3.1	63.6%

FTIR analysis of each variant of CHA can be seen in Figure 8a, with a representative image of CHA, synthesized via the T55 methodology, shown in Figure 8b. The FTIR analysis revealed the presence of both carbonate ( $\text{CO}_3^{2-}$ ) and phosphate groups ( $\text{PO}_4^{3-}$ ) detected at wavelengths of  $1454\text{cm}^{-1}$ ,  $1414\text{cm}^{-1}$ , and  $873\text{cm}^{-1}$  for carbonate and  $1016\text{cm}^{-1}$ ,  $1088\text{cm}^{-1}$ , and  $962\text{cm}^{-1}$  for phosphate. The crystallinity of each variant can be qualitatively characterized through observation of the FTIR peaks. Sharp distinguished peaks such as those seen in Figure 8a between the  $1454\text{cm}^{-1}$  and  $1414\text{cm}^{-1}$  peaks as well as the peaks at  $1016\text{cm}^{-1}$  and  $962\text{cm}^{-1}$  suggests that the synthesized CHA is of high crystallinity

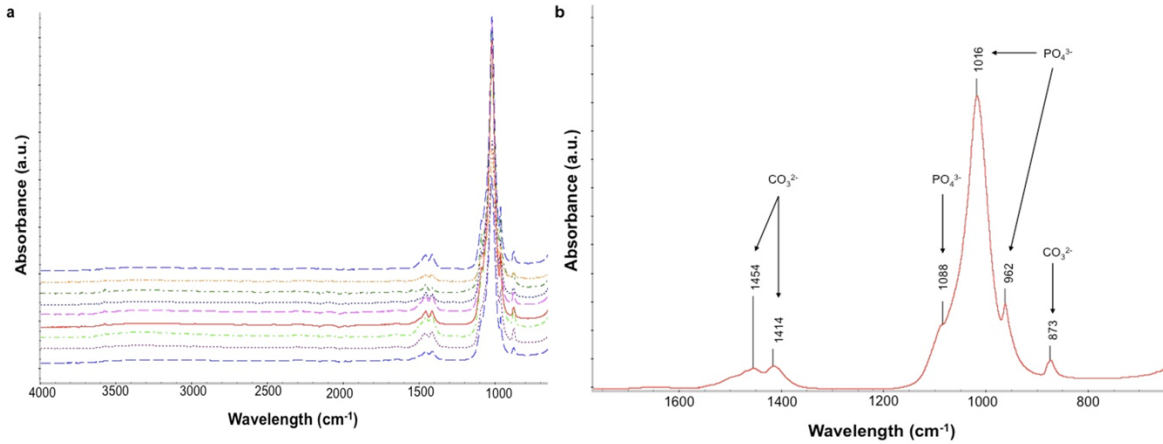


**Figure 8.** FTIR showing each CHA variant has similar chemical composition (a) FTIR of CHA variants from top; PH12, PH11, PH10, R800, R500, R200, T55, T21 and T4. (b) FTIR analysis of representative CHA variant T55 with significant carbonated hydroxyapatite peaks labeled.

CHA crystallites and particle morphology was similar for all CHA variants. CHA crystallites, which are indicated by the black arrows in Figure 9, clearly shows the crystallites to be sphere or almost sphere like in shape. CHA particles indicated by the black dotted outline (Figures 9a), ranged in shape from a roughly spherical morphology to a more random morphology. The CHA particles that were produced consisted of numerous single spherical crystallites that are sintered together during the heat treatment process and create a distinct topography on the outer surface of the agglomerations themselves (Figure 9).

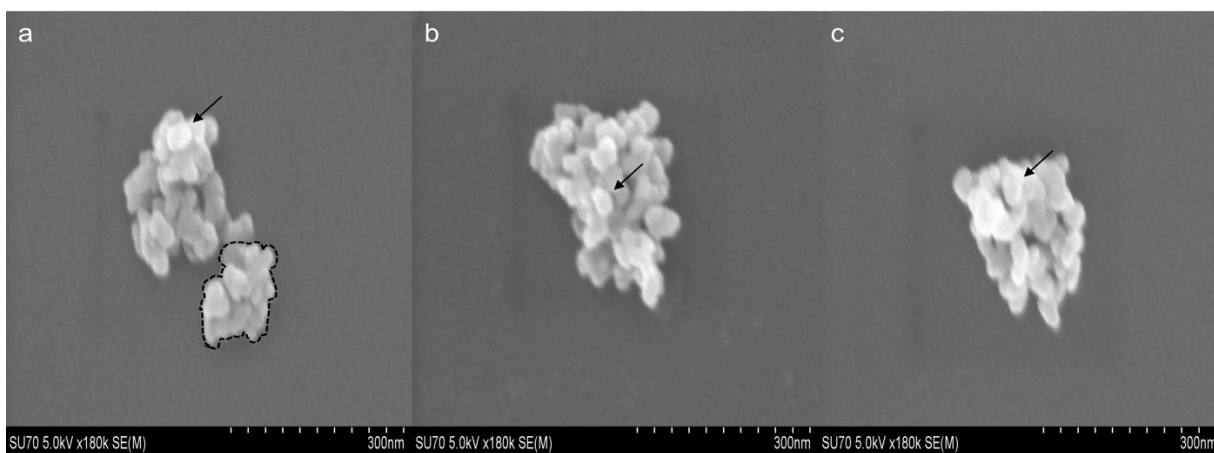


**Figure 9.** Analysis of CHA particle and crystallite morphology. SEM images of each CHA variant at 180 K magnification with CHA crystallites indicated with black arrow and CHA particles shown with black dotted outline (a) CHA variant synthesized using pH 11 methodology. (b) CHA variant synthesized using R500 methodology (c) CHA variant synthesized using T4 methodology.

### Variation in pH Allows Selective Manipulation of pCHA Size.

The nanoemulsion method forms two distinct functional units, the spherical crystallites that are nanometer in scale, noted by arrows (Figure 9), and the particles, noted by a black outline (Figure 9a), that are submicron in scale and are agglomerations of multiple crystallites. These agglomerations are the result of the sintering that occurs during the heat treatment process. CHA crystallite size was visually approximated to be 15–30nm in diameter for each variant of CHA. Moreover, each variant of CHA crystallite maintained a spherical morphology regardless of synthesis methodology used (Figure 9). The z-average diameter, the diameter as measured through DLS analysis, reflects the diameter of the CHA particles for each variant, not the individual CHA crystallites (Figure 10). No significant variation in the CHA particle size was evident from the RPM synthesis methodology, as all particle agglomerations remained roughly 550nm in size (Figure 10). Clear variations in CHA particles size were achieved through both pH and temperature variation, although the pH synthesis methodology was the only variation to show a significant difference between all test groups ( $p < 0.05$ ).

The temperature synthesis methodology allowed for CHA particles to be created with average diameters of  $288.6\text{nm} \pm 53.43$ ,  $558.6\text{nm} \pm 17.24$ , and  $776.8\text{nm} \pm 10.33$  using the

T55, T21 and T4 methodologies respectively (Figure 10). Overall, the variation in size was 488.2nm. Manipulation of the pH during synthesis was the only variation able to significantly affect CHA particle size. This manipulation allowed successful creation of CHA particles with average diameters of 176.3nm  $\pm$  22.74, 474.4nm  $\pm$  6.97, and 955.1nm  $\pm$  36.29 using the pH 10, pH 11 and pH 12 methodologies respectively, an overall variation in size of 602.5nm. Manipulation of temperature did not create a significant variation in the CHA particle size. This may be due to uneven heating or cooling in the solution as well as uneven flux of thermal energy during homogenization despite all precautions to have the solution be at a uniform temperature. This highlights an additional challenge associated with manipulating the temperature of the solutions. In addition, the pH and temperature methodologies resulted in a narrow distribution of particles in each synthesis and creation of the desired size particles was highly repeatable (Figure 10).

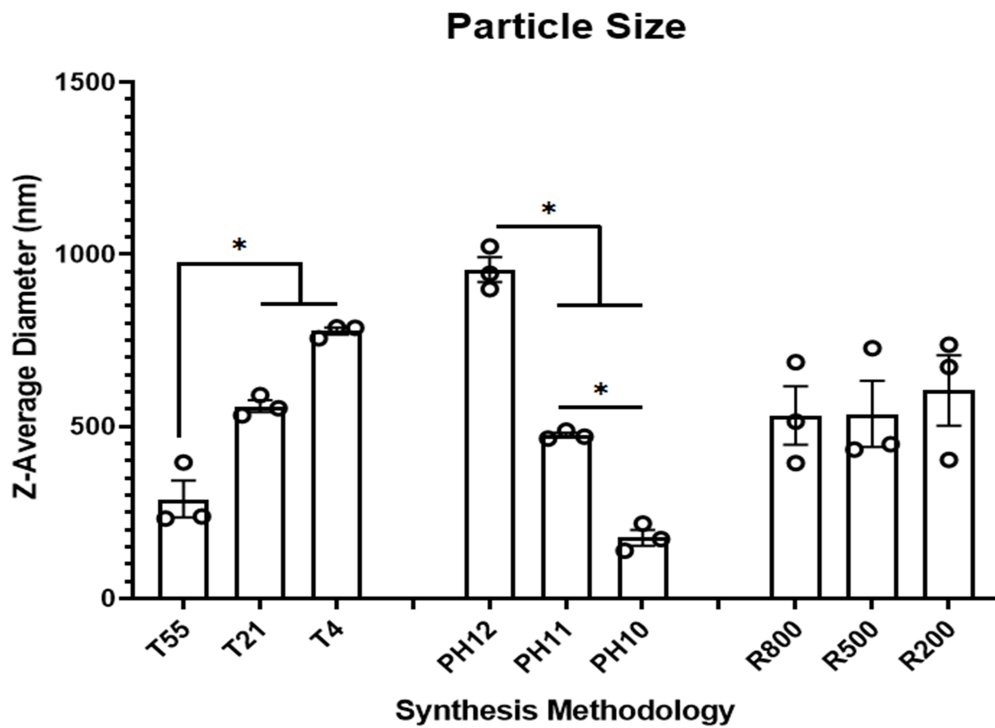


**Figure 10.** Average CHA particle agglomeration size for each synthesis technique. Average z-diameter (nm) of each CHA synthesis methodology evaluated. \*  $p < .05$ ,  $n = 3$  samples with each sample being the average of three separate measurements.

The crystallite size for each CHA variant was calculated using Scherrer's equation (Table 4). The crystallite size ranged from 20–28 nm with the largest crystallite being 27.7 nm, which resulted from the pH 10 variant, while the smallest crystal size of 20.8 nm resulted from the T55 synthesis variant. Narrow distributions of crystallite size were maintained regardless of the synthesis methodology despite the varying CHA particle size.

**500nm CHA Particles Increase Osteoblastic Alkaline Phosphatase Activity without Affecting Viability.**

The effect that all CHA variants had on hFOB 1.19 cells was then evaluated to determine the cytotoxicity of the CHA as well as the potential of CHA to influence osteoblastic differentiation. Osteoblasts cultured in media conditioned with the various CHA variants did not show a significant difference in cell viability compared TCPS controls (Figure 11).

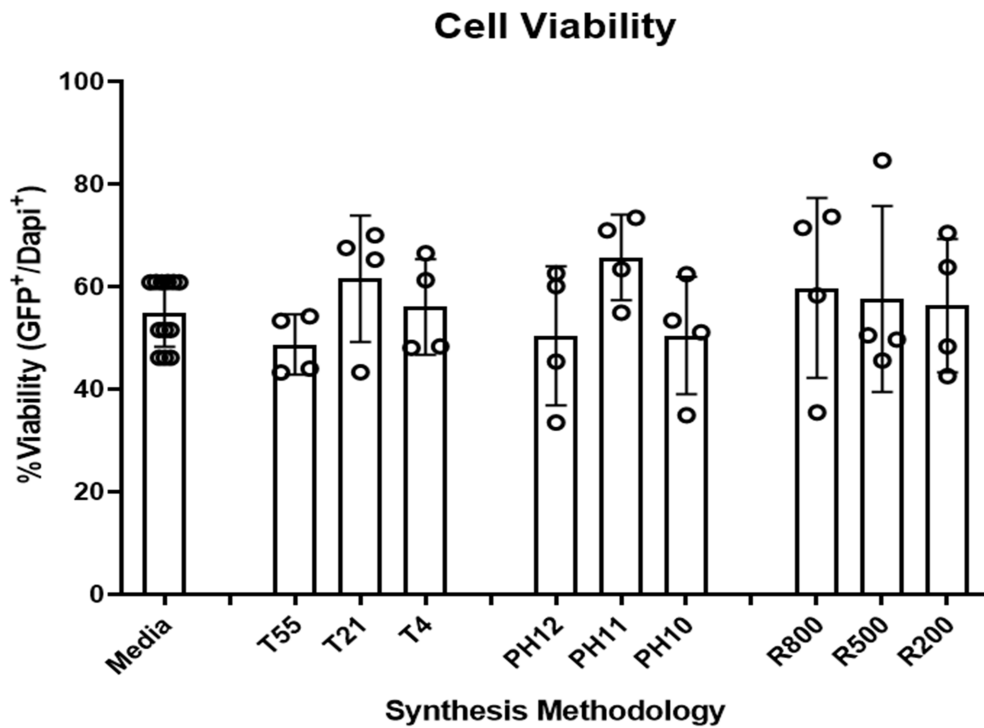


**Figure 11.** CHA effect on osteoblastic cell viability. Percent cell viability (# alive cells/# total cells) of hFOB 1.19 preosteoblastic cells after being cultured with CHA for 48 hr. n = 4–12 samples.



Both the effects of CHA directly and indirectly were evaluated in this study. First, CHA particles of 200nm, 500nm, and 900nm were added directly to media used to cultured hFOB1.19 cells. Addition of the 500nm particles directly to media resulted in a 2-fold increase in cell AP activity after 1 day of culture compared to cells in media without CHA and cells cultured in media with either 200nm or 900nm CHA particles (Figure 12a). Further, culturing cells with CHA particles did not result in any significant changes in osteoblast morphology compared to cells cultured on TCPS or variations between CHA particle sizes (Supplemental Figure S2). To determine if the release of ions from the CHA was contributing to the observed increase in AP activity, hFOB 1.19 cells were cultured in media conditioned with either 200nm, 500nm, or 900nm CHA particles. Conditioned media did not induce a significant variation in AP activity compared to nonconditioned culture media over the course of 7 days regardless of the particle size (Figure 12b). Furthermore, no significant differences were observed between media conditioned with either 200nm, 500nm, or 900nm. This suggests that the ions, if any, released from the CHA were not contributing to the observed osteoblastic differentiation and therefore an ion release profile of the hydroxyapatite was not performed.

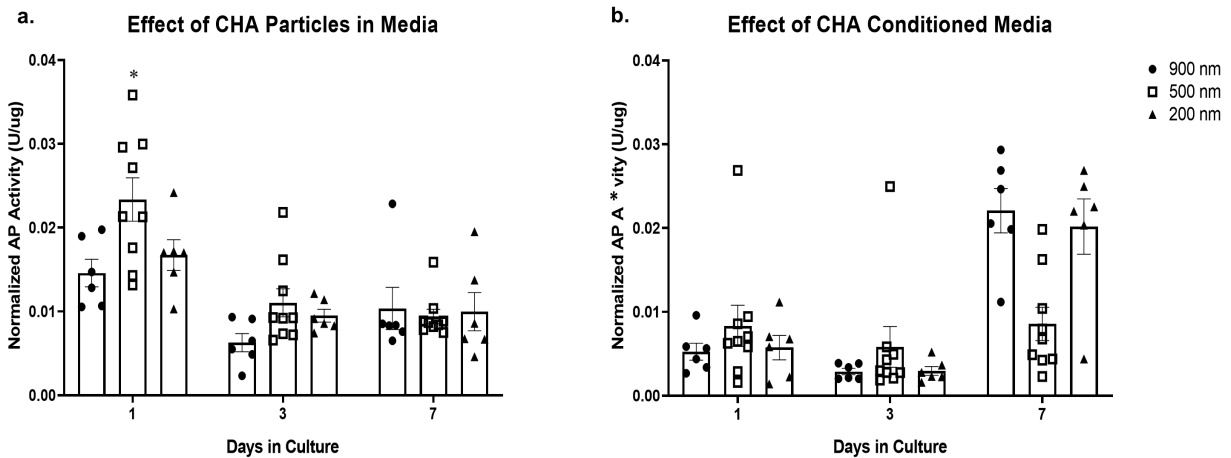


**Figure 12.** Evaluation of the effect each CHA variants has on osteoblastic differentiation. (a) Normalized alkaline phosphatase enzymatic activity of hFOB 1.19 preosteoblastic cells after 1, 3, and 7 days in culture with media conditioned with each CHA variant. (b) Normalized alkaline phosphatase enzymatic activity of hFOB 1.19 preosteoblastic cells after 1, 3, and 7 days in culture with particles from each CHA variant. \*  $p < 0.05$  compared to all other groups,  $n = 3-6$  samples with each sample being the average of two replicates.

## **DISCUSSION**

As the design and use of novel biomaterials for bone tissue engineering becomes of greater importance to meet the demand of increasing bone graft procedures, the use of CHA alone or in tandem with other materials is becoming more common<sup>22,147</sup>. Tailoring the size of hydroxyapatite is a common practice, although it is still not agreed upon as to which size of hydroxyapatite particles is most osteogenic. Moreover, current synthesis methodologies utilize caustic chemicals, surfactants, and extremely high or low temperatures to produce submicron and nano sized hydroxyapatite particles<sup>22,148</sup>. To address these issues, we have modified a simple methodology for the synthesis of biomimetic hydroxyapatite that does not require harsh synthesis techniques and creates a ready to use product that is osteogenically favorable<sup>149</sup>. Our results show that we are able to reproducibly create a range of submicron CHA particles through the manipulation of pH to modify a nanoemulsion technique. In addition, the synthesized CHA maintained similar chemical properties, morphology, and biological characteristics regardless of synthesis methodology used.

The results of this study show that we can selectively manipulate CHA particle size through the manipulation of pH during synthesis (Figure 10). The variation in CHA size we observed through changes in temperature manipulation also looks to be an avenue to manipulate the size of CHA in the submicron range, though it did not induce significant changes in size. Although the ability to control the CHA particle size through pH manipulation has been shown in previous studies, the synthesis methodology used in these previous studies necessitated the use of caustic chemicals or surfactants to produce and manipulate the size of the CHA<sup>150,151</sup>. Despite the efficacy of these synthesis methodologies, reproducibility of these methods is often difficult. The precise conditions that are needed to recreate a narrow distribution of CHA particles in a reproducible manner are often challenging, due to the volatility of the chemicals and temperatures required to synthesize biomimetic hydroxyapatite. The methodology developed during this study does not utilize any caustic chemicals or surfactants and is easily reproduced.

In addition to selectively tailoring the CHA particle size, the CHA synthesized during this study also exhibited highly biomimetic qualities. Biological apatite exhibits a range of crystallinity from 60% to 70% depending on the location of the apatite<sup>124,152</sup>; our synthesized CHA exhibited a crystallinity range of roughly 60% to 85%. Differences in peak intensity between the standard CHA and the representative samples can be observed (Figure 8b). These differences are likely due to variations in the crystallinity of the synthesized apatite, which in the representative sample is roughly 80%, and typical biological apatite, which is roughly 70%. For this reason, the pH synthesis methodology also has advantages over the other methodologies, as it maintains an ideal crystallinity (between 60% and 70%) while temperature manipulation generated higher crystallinity CHA. This is significant because synthetic hydroxyapatite with a crystallinity between 60 and 70% is more bioactive and more osteoconductive than hydroxyapatite that falls outside of the 60–70% range<sup>153–155</sup>. This suggests that the CHA synthesized with the pH methodology is also optimally osteogenic. To examine this further, we evaluated CHA in vitro to determine its overall osteogenic potential.

CHA examined during this study was not cytotoxic, with no synthesis methodology resulting in particles that induced a significant decrease in cell viability compared to cells cultured on TCPS. Interestingly, cells cultured with 500nm hydroxyapatite particles expressed a significantly higher level of AP activity after just 1 day in culture compared to both 200nm and 900nm particles. A review by Chen *et al.*, reported that multiple studies highlighted the fact that 500nm topographic features induced the greatest osteogenic response from stem cells and preosteoblastic cells<sup>101,118</sup>. These features were created using a variety of synthesis techniques ranging from electrospinning and anodization to nanoimprinting<sup>156–158</sup>. The diversity of these synthesis techniques and the corroborating result, that 500nm topographic features promote osteogenesis, highlights an observation made in our study that 500nm CHA particles induce the greatest AP activity compared to other particle sizes. Moreover, studies noted that 500nm topographic features allowed for an increase in cell stiffness, spreading, and adhesions, which is hypothesized to upregulate osteogenesis<sup>159,160</sup>.

It is important to note that many factors influence the cell response to an associated material. Factors such as chemical composition, pH, and crystallinity have all been shown to mediate osteoblastic differentiation<sup>110,121</sup>. In the study presented here chemical composition, crystallinity of the various compositions, and pH, while not shown in this study, are not significantly different between any of the particle sizes evaluated in this study for osteoblastic differentiation. This suggests particle size is the main contributor to osteoblastic differentiation observed in this study. These findings suggest a further avenue of study and, based on the results of the study presented here, suggest investigation of how the 500nm CHA particles regulate cell adhesions, spreading, and stiffness.

## **CONCLUSION**

This work demonstrates that it is possible to repeatably synthesize monophasic, highly crystalline, spherical CHA in the submicron range through the use of a nanoemulsion methodology that eliminates the use of caustic chemicals or surfactants. Moreover, this work demonstrates the ability to vary CHA particle size through manipulation of the synthesis methodology, specifically by manipulating the pH. This knowledge allows a more thorough understanding of a nanoemulsion techniques that reproducibly generates carbonated biomimetic hydroxyapatite particles of submicron scale quickly and safely and at a low cost, allowing this method of hydroxyapatite production to be scaled. In addition, we determined that 500nm CHA particles increased AP activity, suggesting an increase in osteoblastic differentiation, after only 1 day, compared to 200nm and 900nm particles. The further development of the nanoemulsion method for CHA enables further research into the osteogenic potential of hydroxyapatite particles. By tailoring CHA size, the ability to create synthetic biomimetic bone scaffolds with predictable and optimized submicron properties is possible. This will enable investigation and eventual use of submicron and nanoscale environments to facilitate osteogenesis.

## **CHAPTER 5. Hydroxyapatite Particle Density Regulates Osteoblastic Differentiation Through $\beta$ -Catenin Translocation**

Authors:

Otto J. Juhl IV, Anna-Blessing Merife, Yue Zhang, Christopher A. Lemmon, Henry J. Donahue

*Frontiers in Bioengineering & Biotechnology, 2021, 8, 1501–1515*

## **ABSTRACT**

Substrate surface characteristics such as roughness, wettability and particle density are well-known contributors of a substrate's overall osteogenic potential. These characteristics are known to regulate cell mechanics as well as induce changes in cell stiffness, cell adhesions, and cytoskeletal structure. Pro-osteogenic particles, such as hydroxyapatite, are often incorporated into a substrate to enhance the substrate's osteogenic potential. However, it is unknown which substrate characteristic is the key regulator of osteogenesis. This is partly due to the lack of understanding of how these substrate surface characteristics are transduced by cells. In this study substrates composed of polycaprolactone (PCL) and carbonated hydroxyapatite particles (HAp) were synthesized. HAp concentration was varied, and a range of surface characteristics created. The effect of each substrate characteristic on osteoblastic differentiation was then examined. We found that, of the characteristics examined, only HAp density, and indeed a specific density (85 particles/cm<sup>2</sup>), significantly increased osteoblastic differentiation. Further, an increase in focal adhesion maturation and turnover was observed in cells cultured on this substrate. Moreover,  $\beta$ -catenin translocation from the membrane bound cell fraction to the nucleus was more rapid in cells on the 85 particle/cm<sup>2</sup> substrate compared to cells on tissue culture polystyrene. Together, these data suggest that particle density is one pivotal factor in determining a substrate's overall osteogenic potential. Additionally, the observed increase in osteoblastic differentiation is at least partly the result of  $\beta$ -catenin translocation and transcriptional activity suggesting

a  $\beta$ -catenin mediated mechanism by which substrate surface characteristics are transduced.

## **INTRODUCTION**

Studies evaluating the effect of substrate surface characteristics on osteogenesis have determined that there is a significant interplay between surface characteristics and bone cell response<sup>110,121,161</sup>. For instance, recent studies have demonstrated that micro and nano-scale topographies, by affecting surface characteristics such as roughness, wettability, and height, effect changes in the cell's cytoskeletal structure<sup>90,110</sup>. These topographies also promote osteogenesis and direct mesenchymal stem cells toward the osteoblastic lineage<sup>90</sup>. Frequently, the substrate surface characteristics are created by incorporating a pro-osteogenic material, such as hydroxyapatite particles (HAp), directly into the substrate.

Hydroxyapatite is the main mineral component of bone and is highly osteoconductive. HAp is synthesized in a variety of sizes, from the nanometer to micron scale, and a variety of shapes, from spheres to needle-like rods<sup>162-164</sup>. The effect of various HAp sizes and shapes on their osteogenic potential has been summarized in numerous reviews that suggest spherical HAp less than 1 micron in size facilitate osteogenesis to the greatest degree<sup>152</sup>. Unfortunately, hydroxyapatite is not a viable material for all load bearing applications because of its extreme brittleness during shear<sup>124</sup>. To overcome this, HAp is typically combined with other materials, including polymers such as polycaprolactone

(PCL), which is biocompatible, bioresorbable, and exhibits mechanical properties more similar to that of bone<sup>43,44</sup>.

Combining HAp and PCL has resulted in materials that have unique and tunable surface characteristics. By increasing or decreasing the ratio of HAp to PCL, variations in substrate surface characteristics such as roughness, particle density, wettability, and height can be achieved<sup>165</sup>. Studies investigating these substrate properties have yielded conflicting results because the substrates examined have numerous properties that differ. This has made identifying a singular property that is causing osteogenesis challenging. To overcome this, previous studies have cultured cells on nanoposts, limiting the differences in substrate characteristics and instead varying only post-size, post-height, and post-density. These studies determined that the presentation of denser nanoposts to human mesenchymal stem cells resulted in more adipogenic differentiation, while less dense substrates resulted in a more osteogenic differentiation<sup>11,17</sup>. Moreover, nanoposts that were between 200nm and 700nm in diameter were the most osteogenic, but this was also dependent on post-height and stiffness<sup>166</sup>. These studies suggest that the ability of the cell to form the correct cell-substrate adhesion, known as a focal adhesion, is a significant contributor to inducing osteogenesis. However, translation of these results to materials that can be utilized in vivo such as PCL and HAp have yielded conflicting results.

One reason it is still challenging to create novel substrates with increased osteogenic potential is because it is still unknown how substrate surface characteristics are transduced and how this signal then regulates osteogenesis<sup>15,167</sup>. Numerous attempts



have been made to determine the mechanism by which substrate surface characteristics are transduced into intracellular signals. This has given rise to the concept that surface characteristics induce cytoskeletal changes that then alter nuclear morphology and gene expression<sup>12</sup>. Previous data also suggest  $\beta$ -catenin, a protein found at cell adhesions and a key contributor in the Wnt signaling pathway, transduces substrate surface characteristics, but this concept has yet to be validated<sup>60,61</sup>.

The canonical Wnt signaling pathway relies on  $\beta$ -catenin translocation to the nucleus to regulate transcription factors, which in the case of osteoblastic cells, regulate pro-osteogenic genes<sup>168</sup>. Another role of  $\beta$ -catenin is its contribution to the formation and stabilization of cell adhesions such as focal adhesions and cadherins<sup>169</sup>. At E-cadherins,  $\beta$ -catenin binds the cadherin directly at the N-terminus, where it is then stabilized by  $\alpha$ -catenin.  $\alpha$ -catenin then either binds directly to actin or indirectly to vinculin that then binds actin<sup>55</sup>. More recent studies have also suggested that vinculin may directly bind  $\beta$ -catenin after activation and that the  $\beta$ -catenin/vinculin complex is capable of supporting mechanical tension<sup>170–173</sup>. Interestingly, vinculin is also a component of another adhesion complex, focal adhesions, although the role of  $\beta$ -catenin, if any, at focal adhesions is still unknown<sup>174</sup>.

Focal adhesion complexes are composed of greater than 50 proteins and are known to contribute to mechanosensing within the cell<sup>175</sup>. The transmembrane portion is comprised of integrins that bind to the extracellular matrix. Previous studies suggest that integrins respond differentially to various surface characteristics, with different forms of integrins

adhering preferentially to pro-osteogenic substrates compared to sub-optimal substrates<sup>13,17,176</sup>. Focal adhesions, well-known mechanosensors, also increase in size in response to increased actin fiber tension. This phenomenon, known as the growth model of force-induced focal adhesion, is driven by actomyosin-mediated tension<sup>174</sup>. Previous studies examining human mesenchymal stem cell differentiation have observed a correlation between nanopost density, focal adhesion formation and maturation, and the differentiation state of the cell<sup>144</sup>. These studies found the median densities often elicit the greatest increase in focal adhesion maturation and differentiation. In addition, evidence presented by Dubrovskiy *et al.* suggests that  $\beta$ -catenin may localize to focal adhesions as well, binding paxillin during Rac activation<sup>144</sup>. However, the contribution  $\beta$ -catenin may have facilitating focal adhesion formation and binding of actin stress fibers has not been fully explored. The relationship between focal adhesion maturation, osteoblastic differentiation, and  $\beta$ -catenin localization has led to the examination of whether focal adhesions transduce substrate surface characteristics to mediate osteogenesis and, if so, the mechanism by which this occurs<sup>57</sup>.

To better understand the mechanism by which substrate surface characteristics affect osteogenesis we varied the concentration of HAp independent of PCL to create substrates with a range of surface characteristics. We hypothesized that substrates with a concentration of 30% HAp to PCL would increase osteoblastic differentiation compared to lower (5%) or higher (50%) concentrations of HAp to PCL, similar to that which has been observed in previous studies using various densities of nanoposts<sup>177</sup>. Furthermore, the mechanism by which this occurs may involve the regulation of  $\beta$ -catenin by, or

liberation from, proteins at adhesion complexes, located at the cell membrane. This would result in increased  $\beta$ -catenin translocation from these adhesion complexes to the nucleus on the more osteogenic substrate.

To evaluate this hypothesis, we examined osteoblastic differentiation, as assessed by osteoblastic gene expression and alkaline phosphatase (AP) activity, on 5%, 30%, and 50% HAp to PCL substrates. We also evaluated focal adhesion morphology and number over time,  $\beta$ -catenin localization over time, and nuclear  $\beta$ -catenin activity. We observed that cells on substrates with a concentration of 30% HAp to PCL displayed increased expression of genes associated with osteoblastic differentiation and osteoblastic activity, relative to cells on other substrates examined. However, the substrates examined did not exhibit significant changes in surface roughness, wettability, or height. Moreover, focal adhesion turnover and maturation of cells on the substrate with a concentration of 30% HAp to PCL occurs more rapidly compared to cells on tissue culture polystyrene (TCPS). This more rapid turnover and maturation also corresponded with a more rapid release of  $\beta$ -catenin from the membrane bound fraction, where  $\beta$ -catenin is retained at adherens junctions and focal adhesions, to the nucleus.

## **MATERIALS AND METHODS**

### **Materials.**

All chemicals used for nanoparticle and substrate synthesis were obtained from Sigma-Aldrich (St. Louis, MO).

## **Substrate Synthesis and Characterization.**

### *Polycaprolactone and Hydroxyapatite Substrate Synthesis.*

To create a pro-osteogenic substrate to test our hypothesis, various formulations of HAp and PCL substrates were fabricated. Five thousand molecular weight PCL was suspended at a 2.5% wt./vol. ratio in chloroform. The mixture was then homogenized until all PCL was dissolved into solution. After homogenization, 500nm HAp was added into the solution at a ratio of 5%, 30%, or 50% wt./wt. with the PCL. Using a dip-coating technique, 22mm coverslips were coated with one of the following: PCL solution only (PCL), 5% HAp to PCL solutions, 30% HAp to PCL solutions, or 50% HAp to PCL solution. After coating, the various substrates were allowed to dry at room temperature for 24 hours.

### *Substrate Surface Roughness and Height Characterization.*

Substrate surfaces were characterized for roughness and height (z-range) using a Dimension ICON atomic force microscopy platform (Veeco, Plainview, NY). Briefly, each substrate was rinsed with 70% ethanol to remove debris left on the surface after synthesis and the ethanol allowed to evaporate. The substrates were then imaged by atomic force microscopy using a TESPSS antimony doped silicon cantilever (Bruker, Billerica, MA). The cantilever used a single tip with a resonance frequency in the range of 230 KH to 410 KHz. The probe radius was 5nm, with a tip height of 10 $\mu$ m to 15 $\mu$ m, spring constant of 42 N/m and a cone angle of less than 10° over the first 200 nm of tip length. All evaluations were performed in air. The set point voltage was kept between 0.1 V and 0.3 V with the cantilever force kept constant. The frequency employed was manipulated based on the

substrate in order to accurately quantify the surface roughness and height. The scan resolution was  $256 \times 256$  pixels with a scan frequency of 0.85 Hz over a  $5\mu\text{m} \times 5\mu\text{m}$  area scanned. The average height and roughness of three random areas per substrate was determined and used to estimate each substrate's overall roughness and height.

#### *Substrate Surface Energy Characterization.*

Surface energy, also referred to as wettability, was characterized using contact angle measurements with a 590 Advanced Automated Goniometer/Tensiometer (Ramé-Hart, Succasunna, NJ). Briefly, each substrate was rinsed with 70% ethanol to remove any debris left on the surface after synthesis and the ethanol allowed to evaporate. The substrates then underwent contact angle measurement using doubly distilled water. Three random areas were evaluated on each substrate and the average of the three measurements was taken as the substrate's overall wettability. Image analysis was performed by using the DROPimage version 2.4 software (Ramé-Hart, Succasunna, NJ).

#### *Substrate Particle Density Characterization.*

Particle density for the various substrates was quantified using an EVOS light microscope. Images of the substrate were taken at three random locations. Using Fiji image software<sup>145</sup>, HAp was isolated by increasing the contrast between the HAp, which auto-fluoresces, and the background image using a 0.3% increase in saturated pixel contrast. The images were then converted to an 8-bit file format and then the background image subtracted using a 5-pixel rolling ball radius leaving only HAp visible. The particles were then outlined before being quantified using the Analyze Particles tool package in

Fiji<sup>178</sup>. The average particle number of the three random locations was then determined and divided by the field of view to determine the substrates areal particle density (particles/cm<sup>2</sup>).

### **Mechanistic Evaluation of Substrates.**

#### *Osteoblast Cell Culture.*

To assess osteogenesis, the differentiation capacity of human fetal osteoblasts (hFOB 1.19 cells), a preosteoblastic cell line, was assessed as previously described<sup>179</sup>. Briefly, for proliferation of hFOB 1.19 cells, cells were cultured at 33.5°C with 5% CO<sub>2</sub> to 80% confluence in standard DMEM:F12 media supplemented with 10% fetal bovine serum (Gibco, Gaithersburg, MD) and 1% Penicillin/Streptomycin mixture (Sigma, St. Louis, MO). To induce differentiation of the hFOB 1.19 cells, the standard media was supplemented with 100µg/mL ascorbic acid, 10<sup>-8</sup> M menadione, and 10<sup>-8</sup> M dihydroxy-vitamin D<sub>3</sub> (Sigma, St. Louis, MO), and the cells were cultured at 39.5°C with 5% CO<sub>2</sub> until the desired timepoint. Media was changed every 3 days unless otherwise stated for all experimental methods. All substrates used were sterilized by completely submerging the substrates in 70% ethanol for 5 minutes before the ethanol was aspirated and remaining ethanol allowed to evaporate for 1 hour under UV light.

#### *Osteoblastic Gene Expression.*

hFOB 1.19 cells were cultured on tissue culture polystyrene (TCPS), PCL, 5% HA/PCL substrate, 30% HA/PCL substrate, or 50% HA/PCL substrate and cultured under differentiation conditions for 1 and 7 days. At each time point RNA was isolated using a

RNeasy Mini Kit (Qiagen, Hilden, Germany). Quantitative real time PCR (RT-qPCR) was performed using a C1000 Touch Thermal Cycler with CFX96 Real-Time System (Bio-Rad Laboratories, Hercules, CA). PowerUp Sybr Green Master Mix was used to quantify gene expression (Thermo Fisher Scientific). The genes we evaluated are associated with the various stages of osteoblastic differentiation and are as follows; alkaline phosphatase (*ALPL*), Osteocalcin (*BGLAP*), Collagen1-a1 (*COL1A1*), Runt related transcription factor-2 (*RUNX2*), and Sp7 Transcription Factor (*SP7*), the gene that control Osterix (*OSX*) protein expression. Glyceraldehyde-3-Phosphate Dehydrogenase (*GAPDH*) was used as a reference gene for all samples. All primers used in this study were PrimePCR Sybr Green Assay Primers (Bio-Rad Laboratories, Hercules, CA) and the unique assay ID numbers are provided in Table 5. The  $\Delta\Delta C_t$  method used to quantify fold-change in gene expression relative to the housekeeping gene *Gapdh*, as previously described<sup>180,181</sup>.

**Table 5.** Reference numbers associated with each osteoblastic gene evaluated using primers purchased from Bio-Rad Laboratories, Hercules, CA.

Gene of Interest	Gene Abbreviation	Primer Reference #
Alkaline Phosphatase	<i>ALPL</i>	qHsaCID0010031
Osteocalcin	<i>BGLAP</i>	qHsaCED0038437
Collagen1-a1	<i>COL1A1</i>	qHsaCEP0050510
Runt related transcription factor-2	<i>RUNX2</i>	qHsaCID0006726
Sp7 Transcription Factor	<i>SP7</i>	qHsaCEP0025867
Glyceraldehyde-3-Phosphate Dehydrogenase	<i>GAPDH</i>	qHsaCEP0041396

### *Alkaline Phosphatase (AP) Activity.*

hFOB 1.19 cells were cultured on either tissue culture polystyrene (TCPS), PCL substrate, 5% HA/PCL substrate, 30% HA/PCL substrate, or 50% HA/PCL substrate at 15,000 cells/cm and cultured under differentiation conditions for 7 days. Differentiation was evaluated using a colorimetric AP enzymatic activity assay as previously described<sup>182</sup>. Briefly, cells were freeze thawed in 400 $\mu$ L of 0.05% Triton X-100 in phosphate buffered saline twice and then the cell lysate collected. 10 $\mu$ L of each sample lysate was removed and used to quantify total protein concentration using Pierce BCA protein assay kit (Thermo Fisher, Waltham, MA). AP enzymatic activity was then determined by conversion of p-nitrophenyl phosphate to p-nitrophenol. Two hundred microliter of AP reaction buffer was then added to each sample and incubated at room temperature for 30 minutes. After incubation 50 $\mu$ L of each sample was moved to 200 $\mu$ L of 0.1 NaOH in a 96 well-plate to quench the reaction. All samples were then measured at 410nm and SIGMA units calculated based on the standard curve. All readings were then normalized to total protein concentration to control for variations in cell number between samples.

### *Mineralization Staining.*

hFOB 1.19 cells were cultured on either tissue culture polystyrene (TCPS), PCL substrate, 5% HA/PCL substrate, 30% HA/PCL substrate, or 50% HA/PCL substrate at 15,000 cells/cm and cultured under differentiation conditions for 7, 10 and 14 days. Mineralization was evaluated using alizarin red staining as previously described<sup>183</sup>. Briefly, cell cultured medium was removed, and cells were fixed in 4% paraformaldehyde for 15 min at room temperature. After fixation, cells were gently washed twice with deionized water. After washing 500 $\mu$ L of Alizarin Red Staining Solution (Sigma Aldrich,



St. Louis, MO) was added to each well and incubated for 1 hour at room temperature. After incubation, excess dye was removed, and cells were gently washed 2 times with deionized water. 400uL of acetic acid was then added to each well and incubated for 30 minutes at room temperature under agitation. Cells were released from substrate by scarping, and then acetic acid and cell mixture was transferred to a 1.5mL microcentrifuge tube. The sample was then vortexed for 30 seconds before being heated to 85C for 10 minutes. Immediately following incubation samples were placed on ice for 5 minutes and then immediately centrifuged for 15 minutes. Supernatant was then removed, and all samples measured at 405nm and mineralization quantified.

#### *Focal Adhesion Staining.*

hFOB 1.19 cells were cultured on either glass, PCL, 5% HA/PCL substrate, 30% HA/PCL substrate, or 50% HA/PCL substrate at 15,000 cells/cm and cultured under differentiation conditions for 1, 2, 4, 12, 24, or 48 hours. At the selected time point, cells were stained using a FAK 100 Actin Cytoskeleton and Focal Adhesion Staining Kit (Sigma, St. Louis, MO). Briefly, cell culture medium was removed, and cells were fixed in 4% paraformaldehyde for 15 min at room temperature. After fixation, cells were washed twice with wash buffer consisting of 0.01% Tween-20 in PBS. Cells were then permeabilized with 0.1% Triton-X100 in PBS for 3 minutes. After permeabilization cells were washed twice with wash buffer and then blocked for 30 minutes at room temperature in Odyssey Blocking Buffer (Thermo Fisher Scientific, Waltham, MA). After blocking anti-vinculin antibody was diluted to 1:250 in blocking buffer and incubated for 1 hour at room temperature. Cells were then washed three times in wash buffer. After washing ReadyProbes AlexaFluor 488 (Thermo Fisher Scientific, Waltham, MA) was diluted in PBS according to the manufactures protocol. Samples were then incubated in the PBS solution for 1 hour at room temperature and protected from light. After incubation samples

were washed three times in wash buffer and then DAPI stain, diluted at 1:1,000 in PBS, was added and incubated at room temperature for 5 minutes. After incubation samples were mounted on glass slides using ProGold Antifade Mounting Solution (Thermo Fisher Scientific, Waltham, MA).

#### *Focal Adhesion Characterization.*

Confocal images of the various samples were gathered using an LSM 710 Confocal Microscope (Zeiss, Jena, Germany). Briefly, a 30 $\mu$ m z-stack of each sample was taken with 10 slices per stack. The image that provided the greatest resolution of vinculin (GFP+) was then used for further analysis and quantification. Using custom MATLAB-based software, images were analyzed for focal adhesion size and morphology, and number normalized to cell number. A contrast threshold of 0.450 was selected and applied to all images allowing segmentation of the individual focal adhesions. If the segmentation did not accurately represent the original image, a different threshold value was chosen manually until segmentation of the focal adhesions was representative of the original images. Thresholding analysis was then performed and focal adhesion number, length and width dimensions ( $\mu$ m), and area ( $\mu$ m<sup>2</sup>) were output and recorded. Representative images are shown in supplemental figure S3.

#### *$\beta$ -Catenin Cellular Dynamics.*

The 30% HA/PCL substrate, which elicited the greatest increase in focal adhesion maturation and osteoblast differentiation, along with TCPS (control), were further evaluated to assess  $\beta$ -catenin cellular dynamics. hFOB 1.19 cells were seeded onto

either TCPS or pro-osteogenic (30% HA/PCL) substrates at 100,000 cells/cm<sup>2</sup> and cultured under differentiation conditions for 4 hours, 12 hours, 24 hours, 48 hours, 72 hours, or 96 hours. After culture, cells underwent protein fractionation using the Subcellular Protein Fractionation kit for Cultured Cells (Thermo Fisher Scientific, Waltham, MA). After fractionation, 10 $\mu$ L of cell lysate from each fraction was removed and used to quantify total protein concentration using a Pierce BCA protein assay kit (Thermo Fisher, Waltham, MA). 25 $\mu$ g of total protein from each cell fraction at the various time points was then used to quantify total  $\beta$ -catenin protein concentration in the various cell fractions over time using a Human Total  $\beta$ -catenin DuoSet IC ELISA (R&D Biosystems, Minneapolis, MN). All cell fractions were then normalized to total  $\beta$ -catenin concentration at the respective timepoints.

*Luciferase Based  $\beta$ -Catenin Translocation Reporter Assay.*

To validate nuclear  $\beta$ -catenin translocation and activity from cell fractionation experiments, hFOB 1.19 cells were examined using a luciferase-based reporter assay (Promega Corporation, Madison, WI) as previously described<sup>184</sup>. Briefly, hFOB1.19 cells were transiently transfected with either a TOPFLASH reporter construct, which contains a firefly luciferase reporter that is activated by TCF/LEF binding or a FOPFLASH reporter construct, which has a mutated TCF/LEF protein that prevents  $\beta$ -catenin activation of the firefly reporter. After 24 hours, 100,000/cm<sup>2</sup> cells were seeded onto either TCPS or the pro-osteogenic substrate (30%) and cultured for 48 hours and 72 hours. After culture, the cells were lysed and a TOPFLASH/FOPFLASH quantified.  $\beta$ -catenin translocation and activity in cells on TCPS or the pro-osteogenic substrate was then calculated.

*Inhibition of  $\beta$ -Catenin Binding to TCF/LEF.*

To determine if observed changes in differentiation were, in part, a result of  $\beta$ -catenin activity, we inhibited  $\beta$ -catenin binding to TCF/LEF using a small molecule inhibitor PNU-74564<sup>179</sup>. Under normal physiological conditions  $\beta$ -catenin binds TCF/LEF upon translocation to the nucleus, which then activates transcription of various genes associated with osteoblastic differentiation and other genes such as *AXIN2*<sup>180</sup>. Upon introduction of PNU-74564, the binding of  $\beta$ -catenin is inhibited, thus inhibiting downstream effector gene expression. hFOB 1.19 cells were seeded onto either TCPS or pro-osteogenic (30% HA/PCL) at 100,000/cm<sup>2</sup>. The cells were then exposed to either differentiation media supplemented with 0.1% dimethyl sulfoxide (DMSO) or differentiation media supplemented with 0.1% DMSO and 25 $\mu$ M PNU-74564 determined by TOPFLASH expression evaluate at 10 $\mu$ M, 25 $\mu$ M, and 50 $\mu$ M (Supplemental Figure S4). Cells were then cultured under differentiation conditions for 2 days, 3 days, or 7 days with media changed every 2 days. At each time point cells were evaluated for AP activity as described previously in the section *Alkaline Phosphatase (AP) Activity*, or for *AXIN2* gene expression using methods described previously in section *Osteoblastic Gene Expression*. *GAPDH* was used as a reference gene for all samples. All primers used were PrimePCR Sybr Green Assay Primers (BioRad Laboratories, Hercules, CA). The  $\Delta\Delta$ Ct methodology was used as described previously to compared changes in gene expression relative to *AXIN2* gene expression in the control cells cultured on TCPS at day 2<sup>4</sup>.

### **Statistical Evaluation.**

Changes in substrate surface properties were assessed with 3 or more samples with each sample being the average of three replicates. Gene expression was assessed for 3 to 4 samples with each sample being the average of three replicates. Focal adhesion quantification and characterization was assessed with 3 samples with each sample consisting of approximately 5 to 75 cells or roughly 500 to 5000 focal adhesions per sample.  $\beta$ -catenin localization was assessed for 4 to 6 samples with each sample consisting of two replicates. Osteoblastic gene expression and differentiation in response to  $\beta$ -catenin inhibitor PNU-74564 was assessed for 5 to 6 samples with each sample being the average of 3 replicates or 2 replicates for gene expression and AP activity, respectively. Changes in surface properties and osteoblastic AP activity were assessed using two-way ANOVA followed by Tukey's post-hoc analysis and are reported as mean  $\pm$  SD. Changes in osteoblastic gene expression and focal adhesion size and eccentricity were assessed using two-way ANOVA followed by Tukey's post-hoc analysis and are reported as mean  $\pm$  SD. Changes in  $\beta$ -catenin localization were assessed using two-way ANOVA followed by Tukey's post-hoc analysis and are reported as mean  $\pm$  SD. Changes in  $\beta$ -catenin translocation and activity, determined using a luciferase-based reporter assay, was assessed using an unpaired t-test followed by Bonferroni post-hoc analysis and are reported as mean  $\pm$  SD. The effect of  $\beta$ -catenin inhibitor, PNU-74564, on *AXIN2* gene expression and AP activity were assessed using two-way ANOVA followed by Tukey's post-hoc analysis and are reported as mean  $\pm$  SD. All analysis was performed using GraphPad Prism version 8.1.1 for Windows (GraphPad Software, La Jolla California USA). Values of  $p < 0.05$  were considered statistically significant.

## RESULTS

### **Substrate Surface Roughness and Particle Density Varied Based on HA Concentration.**

Characterization of the roughness, substrate height, particle density, and wettability for the glass substrate, PCL substrate, 5% HA/PCL, 30% HA/PCL, and 50% HA/PCL substrates is summarized in Table 6. The PCL coating in HA/PCL substrates alone was 150nm thick in areas that did not include a particle, affirming that the HA particles were not covered but embedded during the dip coating process (Supplemental Figure S5). The substrate height of glass and PCL only substrates did not vary significantly from each other with observed values of  $543 \pm 8\text{nm}$  and  $598 \pm 82\text{nm}$ , respectively. However, these values were significantly different than all other substrates evaluated. No significant variation in substrate height was observed between the 5% and 30% substrates with observed heights of  $1063 \pm 229\text{nm}$  and  $969 \pm 361\text{nm}$ , respectively, while the 50% substrate with an average height of  $2165 \pm 121\text{nm}$  was significantly different than all other substrates evaluated. Substrate wettability did not vary significantly between any of the evaluated substrates, but surface roughness of the 50% HA/PCL substrate was greater than all other substrates. Particle density did vary significantly between the Glass, TCPS, and 5% substrates with particles densities of  $0 \pm 0\text{p/cm}^2$ ,  $3 \pm 1\text{p/cm}^2$ , and  $16 \pm 2\text{p/cm}^2$ , respectively, compared to the 30% and 50% substrates with particle densities of  $86 \pm 2\text{p/cm}^2$  and  $165 \pm 8\text{p/cm}^2$ , respectively. The 30% and 50% substrates were significantly different than all other substrates and significantly different from each other.

**Table 6.** Substrate characteristic characterization and evaluation of osteoblastic differentiation.  $n \geq 3$  with each sample being the average of 3 replicates. Groups sharing the same letter are not significantly different ( $p < 0.05$ ) within the same column.

Substrate	Height (nm)	Roughness (Ra)	Surface Energy (°)	Particle Density (particles/cm)	AP Activity (U/ug)
TCPS	--	--	--	--	13 ± 4.9
Glass	543 ± 8 <sup>a</sup>	2 ± 2.19	84.32 ± 1.11	0 ± 0 <sup>a</sup>	13 ± 5.4
PCL	598 ± 82 <sup>a</sup>	8 ± 19.16	85.88 ± 1.11	3 ± 1 <sup>a</sup>	13 ± 6.4
5%	1063 ± 229 <sup>b</sup>	21 ± 9.58	88.24 ± 0.73	16 ± 2 <sup>a</sup>	17 ± 9.8
30%	969 ± 361 <sup>b</sup>	25 ± 7.97	87.42 ± 0.98	86 ± 2 <sup>b</sup>	32 ± 9.2 <sup>a</sup>
50%	2165 ± 121	94 ± 3.53 <sup>a</sup>	92.03 ± 0.36	165 ± 8 <sup>c</sup>	15 ± 9.9

**Osteoblastic Differentiation Is Increased On 30% HA/PCL Substrate.**

In order to assess osteogenic potential of the various substrates, expression of key osteoblastic differentiation markers was assessed at days 1 and 7 (Figure 13). At day 1, *BGALP* expression was significantly upregulated in cells on the 30% substrates vs. all other substrates. *SP7* expression was significantly upregulate in cells on the 5% substrate compared to all other substrates, however these results varied based on HA/PCL composition.

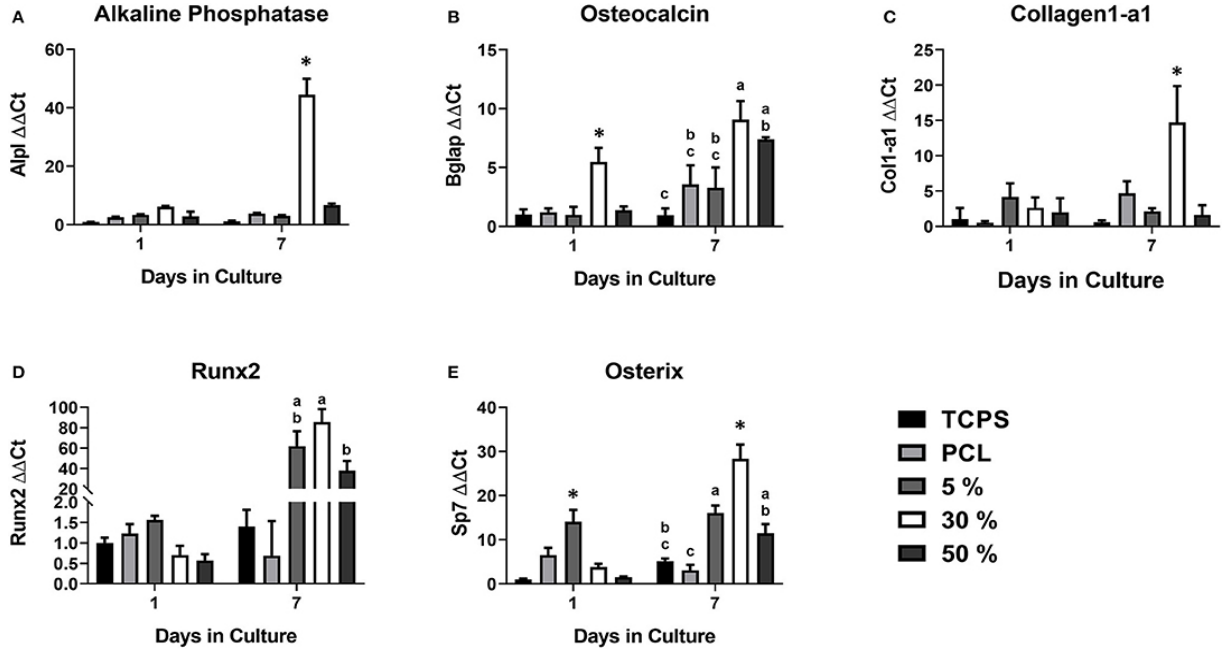


**Figure 13.** Osteoblastic gene expression on the various PCL/HA substrates. Evaluation of osteoblastic gene expression of (a) alkaline phosphatase (*ALPL*), (b) osteocalcin (*BGLAP*), (c) collagen1-a1 (*COL1A1*), (D) *RUNX2*, and (E) Osterix (*SP7*) at 1 and 7 days on the various substrates evaluated in this study. Substrates sharing the same letter denotes a lack of significance at the same time point, \* significantly different compared to all other groups at the same time point. n = 3–4 samples with each sample being the average of three replicates.

Trends were more apparent after 7 days of culture. *RUNX2* gene expression, a marker of commitment to the osteoblast lineage, was significantly increased in cells on substrates that contained HA (5%, 30%, and 50%) compared to cells that were seeded on substrates that did not contain HA (TCPS, PCL). This suggests HA has a significant impact on osteoblastic differentiation, regardless of the substrate characteristics. Cells on the 30% HA/PCL substrate had significantly greater gene expression in genes related to bone matrix deposition (*ALPL*, *COL1A1*, and *BGLAP*) and *SP7* than all other groups. This indicated that the 30% HA/PCL substrate promotes greater osteoblastic differentiation



compared to other substrates. To confirm the results observed at day 7 on the various substrates, AP activity and mineralization was quantified for cells on each substrate. After 7 days of culture cells on the 30% substrate exhibited a significant 1-fold increase in AP activity compared to cells on any of the other substrates (Table 6). Significant variations in AP activity were not observed in cells on any of the other substrates. After 14 days in culture, only cells cultured on the 30% substrate exhibited a significantly greater amount of mineralization compared to cell cultured on any of the other substrates (Supplemental Figure S6). No significant variations in mineralization were observed on any substrate at after either 7 or 10 days in culture.

**Osteoblast Focal Adhesion Maturation Was Increased by 30% HA/PCL Substrate.**

The number of focal adhesions per cell was evaluated for all substrates (Figure 14a). Over the first 12 hours all substrates demonstrated a dramatic increase in focal adhesion number. After 24 hours the number of adhesions per cell begins to decrease on all substrates aside from the PCL substrate. From 12 hours to 24 hours, the 30% substrate had the greatest decrease in adhesion number, decreasing by roughly 100 adhesions per cell. Conversely, the total number of adhesions per cell on glass, 5% HA/PCL and 50% HA/PCL substrates decreased by roughly 50 adhesions per cell. The decrease in adhesion number continued at 48 hours when the evaluation concluded. Again the 30% HA/PCL substrate had the greatest decrease in adhesion number per cell compared to the glass, 5% and 50% HA/PCL substrates. The number of adhesions per cell in cells on the PCL substrate did decrease drastically between 24 hours and 48 hours but remained higher than all other substrates.

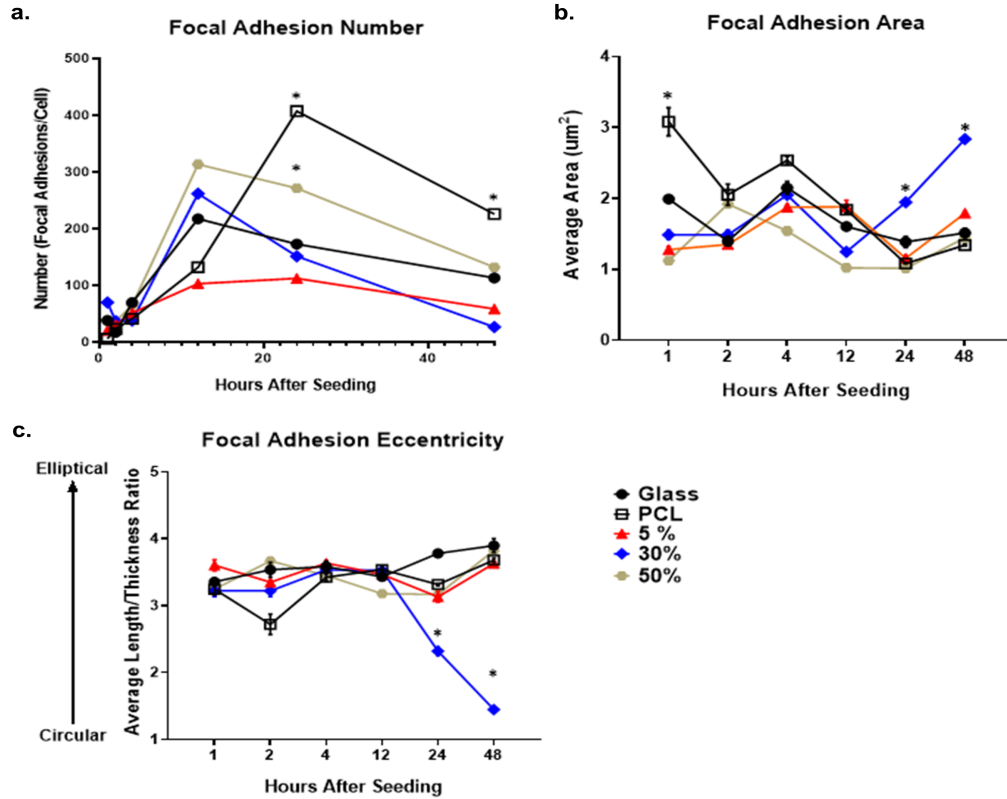


**Figure 14.** Focal adhesion number, size, and morphology over time on each of the evaluated substrates. Temporal quantification of focal adhesion (a) number, (b) area, and (c) eccentricity over time on either glass, PCL, 5%, 30%, or 50% substrates. \*  $p < 0.05$  compared to all other groups at the same time point.  $n = 3$  samples with each sample consisting of approximately 5–75 cells or roughly 500 to 5000 focal adhesions per sample.

To further evaluate focal adhesion maturation, both adhesion size and eccentricity were quantified. The average area of focal adhesions in cells on the 30% HA/PCL substrate was significantly increased 24 hours and 48 hours after cell seeding compared to all other substrates (Figure 14b). Furthermore, compared to cells on all other substrates, a 1-fold and 3-fold increase in adhesion eccentricity (value closer to 1) was observed in cells on the 30% HA/PCL substrate 24 hours and 48 hours, respectively, after cell seeding. We

also observed differences in focal adhesion morphology in cells cultured on other substrates 2 hours after cell seeding (Figure 14c). These variations in adhesion morphology were not as much as those observed 24 hours and 48 hours after cell seeding on the 30% substrate and therefore are not discussed in detail. The increase in focal adhesion area and decrease in overall number are typical markers of focal adhesion maturation<sup>4</sup>. These results indicate that the 30% HA/PCL substrate caused more rapid focal adhesion turnover and maturation compared to all other substrates evaluated.

### **More Rapid $\beta$ -Catenin Protein Translocation from Cell Membrane to Nucleus on Pro-Osteogenic Substrate (30% PCL/HA).**

To further examine our hypothesis, we examined sub-cellular  $\beta$ -catenin localization with protein fractionation and ELISA to quantify  $\beta$ -catenin localization within the cell. We also evaluated transcriptional activity using a TOPFLASH reporter assay (Figure 15). Because we sought to evaluate the mechanism by which substrate surface characteristics induce osteoblastic differentiation, and because the 30% HA/PCL substrate was the only substrate that induced osteoblastic differentiation (Table 6 and Figure 13), it was the only substrate that was evaluated in further detail. We will refer to the 30% substrate as the “pro-osteogenic substrate” henceforth because it enhanced pro-osteogenic capacity and induced greater focal adhesion maturation. Data from cells cultured on TCPS is presented as a reference to more clearly illustrate the observed variations of  $\beta$ -catenin localization and activity in cells cultured on the 30% substrate which have undergone significant differentiation compared to cells cultured on a substrate that did not induce differentiation.

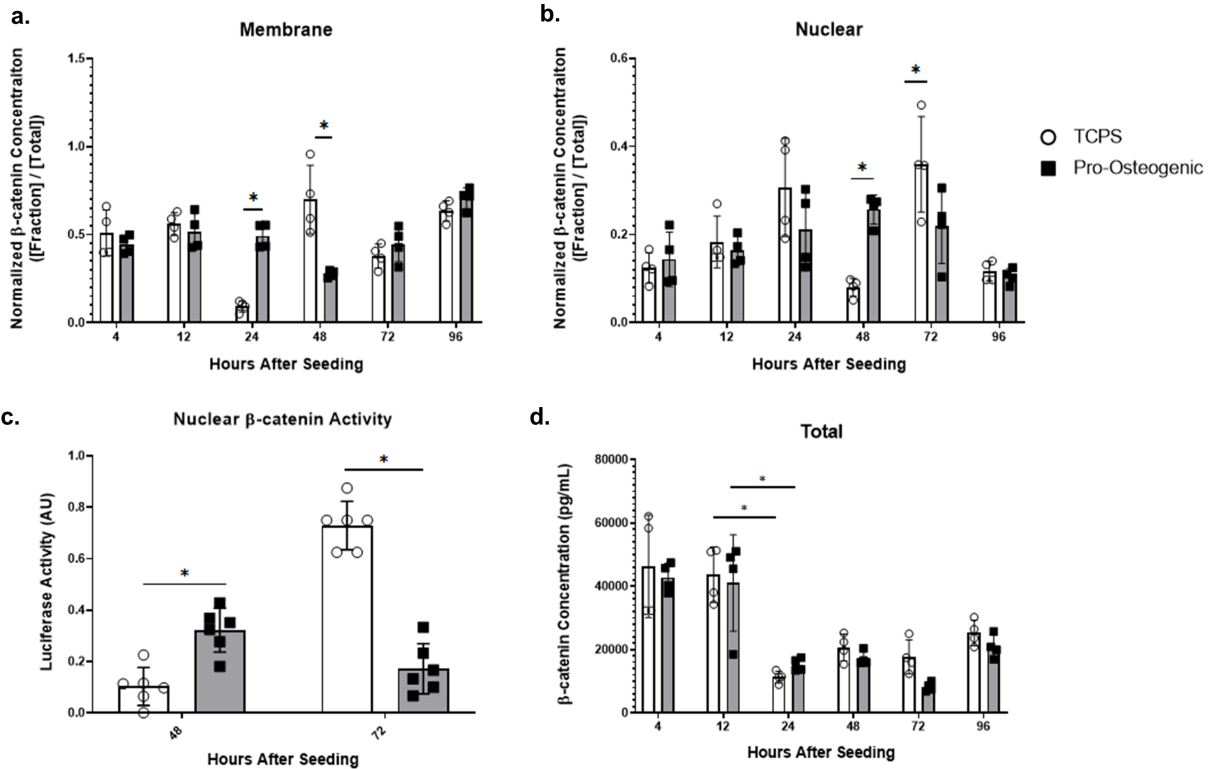


**Figure 15.**  $\beta$ -catenin localization and total  $\beta$ -catenin concentration over 96 hours and transcriptional activity at 48 hours and 72 hours in hFOB 1.19 cells cultured on either TCPS or pro-osteogenic substrate. Quantification of normalized  $\beta$ -catenin concentration in either the (a) membrane bound cell fraction, (b) nuclear cell fraction, or (d) total  $\beta$ -catenin concentration. (c) Nuclear  $\beta$ -catenin activity quantified by TOPFLASH activity on either TCPS or pro-osteogenic substrate after 48 hours and 72 hours.  $n = 4-6$  samples with each sample consisting of two replicates. \*  $p < 0.05$ .

At each time points, cytoplasmic, membrane, nuclear, and cytoskeletal fractions were isolated and normalized to total  $\beta$ -catenin concentration at the respective timepoint.  $\beta$ -catenin concentration in the cytoplasmic and cytoskeletal fraction was not significantly different at any time point and is therefore not shown. At 4 hours, 12 hours, and 96 hours after seeding cells onto either TCPS or pro-osteogenic substrate, no cell fraction exhibited significant differences in  $\beta$ -catenin concentration. 24 hours after cell seeding, no

significant variations in total  $\beta$ -catenin concentration in the nuclear fraction was observed between cells cultured on TCPS or pro-osteogenic substrate. However, in the membrane bound fraction, where  $\beta$ -catenin is localized at adherens junctions or focal adhesions, we observed a significant increase in  $\beta$ -catenin concentration in cells on pro-osteogenic substrates compared to cells on TCPS (Figure 15a). At 48 hours, in the membrane bound fraction we observed a significant increase in  $\beta$ -catenin concentration in cells on TCPS compared to cells on the pro-osteogenic substrate (Figure 15a). Cells on pro-osteogenic substrates also displayed a significant increase in  $\beta$ -catenin concentration within the nuclear fraction compared to cells cultured on TCPS (Figure 15b). At 72 hours, no significant variations in normalized  $\beta$ -catenin concentration within the membrane bound fraction was observed between cells on TCPS and cells on the pro-osteogenic substrate. However, there was a significant increase in normalized  $\beta$ -catenin concentration in the nuclear fraction of cells on TCPS compared to cells on pro-osteogenic substrate.

To confirm these findings, we used a luciferase-based TOPFLASH reporter assay that indicates increased transcriptional activity of TCF/LEF caused by  $\beta$ -catenin binding within the nucleus (Figure 15c). We observed a significant increase in TOPFLASH activity in cells on the pro-osteogenic substrate compared to cells on TCPS at 48 hours. At 72 hours we observed a significant increase in TOPFLASH activity in cells on TCPS compared to cells on pro-osteogenic substrate. Both of these results corroborate our finding as regards the translocation of  $\beta$ -catenin observed when using protein fractionation coupled with ELISA. Total cellular  $\beta$ catenin was also quantified and no significant difference in cells on TCPS compared to cells on pro-osteogenic substrate at any of the examined time points

(Figure 15d). Interestingly, at 4 hours and 12 hours the total, concentration of  $\beta$ -catenin, i.e., combining membrane and nuclear fractions, was roughly 4,500pg/mL. At 24 hours the total concentration of  $\beta$ -catenin within the cells decreased almost 1.5-fold, to roughly 1500pg/mL, in cells cultured on both the TCPS and pro-osteogenic substrate. The total  $\beta$ -catenin concentration within the cells cultured on TCPS and pro-osteogenic substrate then remained at the lower concentration for the remainder of the study.

### **Inhibition of $\beta$ -Catenin Binding to TCF/LEF Prevents Substrate-Induced Increases in Osteoblastic Differentiation.**

To examine whether the observed changes in osteoblastic differentiation were, in part, a result of the observed increase in  $\beta$ -catenin translocation to the nucleus we then inhibited  $\beta$ -catenin's ability to bind to TCF/LEF using PNU-74564<sup>5</sup>. We examined the inhibitor's efficacy by evaluating *AXIN2*, a downstream effector gene of TCF/LEF<sup>6</sup>. After 2 days in culture, in the absence of PNU-74564, *AXIN2* gene expression increased significantly in cells cultured on pro-osteogenic substrates compared to cells cultured on TCPS (Figure 16a). However, the observed increase in *AXIN2* expression in cells on pro-osteogenic substrates was inhibited in the presence of PNU-74564. After 3 days in culture, cells cultured on either TCPS or pro-osteogenic substrate, in the absence of PNU-74564, displayed a significant increase in *AXIN2* gene expression compared to cells cultured on the same substrate in the presence of PNU-74564. Moreover, in the absence of PNU-74564, *AXIN2* gene expression in cells cultured on TCPS was significantly increased compared to cells cultured in the absences of PNU-74564 on pro-osteogenic substrate. After 7 days in culture, no significant changes in *AXIN2* gene expression were observed

in any of the groups evaluated. AP activity was significantly increased after 7 days in cells cultured on pro-osteogenic substrate not in the presence of PNU-74564. This increase was inhibited in cells exposed to PNU-74564 (Figure 16b).

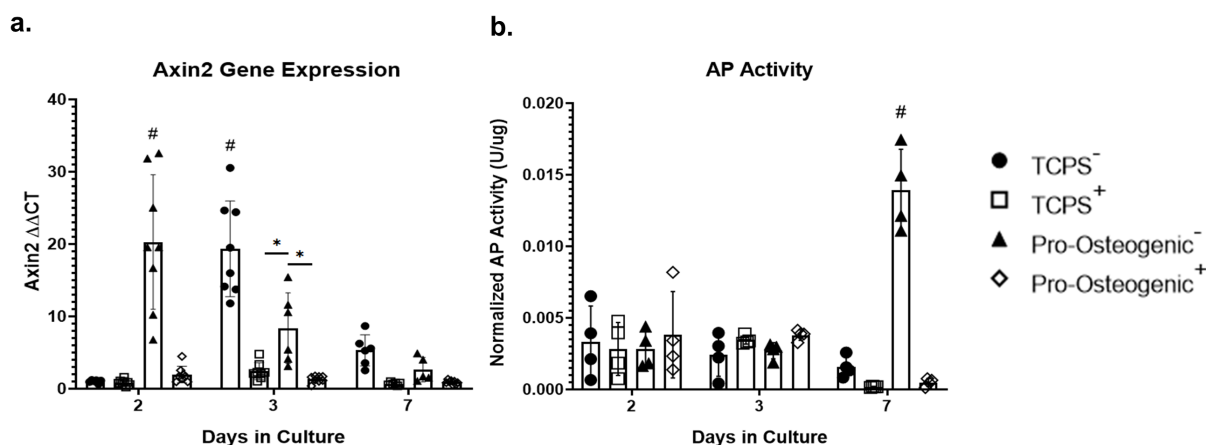


**Figure 16.** Inhibition of  $\beta$ -catenin binding to TCF/LEF in hFOB 1.19 cells on TCPS or Pro-Osteogenic Substrates. Evaluation of effect of  $\beta$ -catenin inhibitor, PNU-74564, on (a) Axin2 gene expression and (b) AP Activity in cells cultured in media with inhibitor (+) or without inhibitor (-) on either TCPS or Pro-Osteogenic substrates. \*  $p < 0.05$ , #  $p < 0.05$  compared to all other groups at same time point.  $n = 5-6$  samples with each sample being the average of 3 replicates or 2 replicates for gene expression and AP activity, respectively.

## DISCUSSION

Development of substrate surface characteristics to promote osteointegration has been an area of intense interest for decades. However, the specific mechanism by which substrate surface characteristics are transduced, as well as what substrate characteristic may regulate this mechanism, are still largely unknown. We hypothesized that the 30% HAp particle density may be a key regulator of osteogenesis. Further, liberation of  $\beta$ -

catenin from focal adhesions as they undergo maturation and the subsequent translocation of  $\beta$ -catenin to the nucleus is a possible mechanism by which substrate surface characteristics are transduced. We observed that only one of the evaluated substrates, the 30% PCL/HA substrate, induced an increase in osteogenic gene expression, AP activity and focal adhesion maturation (Figure 13). We also determined that the cells on the 30% PCL/HA substrate had more rapid  $\beta$ -catenin translocation from the cell membrane to the nucleus than cells on TCPS. These results suggest that focal adhesion turnover, by releasing  $\beta$ -catenin, increases cellular osteogenic activity by increasing nuclear  $\beta$ -catenin transcriptional activation.

Upon evaluation of the 30% HAp substrate surface characteristics, only particle density differed significantly between all other substrates examined in this study. Substrate height, roughness, and wettability were not significantly different between the substrates examined (Table 6). However, literature suggests that the determination of which substrate surface characteristics regulate osteogenesis is highly complex.

Investigation by Dalby *et al.*<sup>67</sup> and Khang *et al.*<sup>7</sup> determined that substratum roughness and height directly affected osteoblastic response, a finding not corroborated by our study. Specifically, they determined that micron scale topographies with a substrate height between 100nm to 300nm and nanoscale roughness between 12nm and 14nm elicited increased osteoblastic differentiation. Lim *et al.* proposed that substratum surface height was responsible for inducing osteoblastic differentiation<sup>8,57,185</sup>. They determined that isotropic topography with a height of 11nm induced greater osteoblastic



differentiation, proliferation, focal adhesion formation and cell spreading compared to 35nm and 85nm high topographies *in vitro*<sup>8,185</sup>. A study by Loisel et al. evaluated substratum topography *in vitro* and *in vivo*<sup>152</sup>, with findings contradictory to those observed by Lim et al. Loisel et al. observed that 50nm to 60nm substratum height induced the greatest osteoblastic differentiation *in vitro* as well as greater *in vivo* mineralization compared to 10nm to 15nm and 45nm substratum height<sup>124</sup>. In the study presented here we found no significant differences in surface roughness between the 5%, 30%, and 50% substrates, with roughness averages of 21, 25, and 94, respectively. Although this study evaluated significantly larger substratum surface heights (0.5µm – 2µm), variations in substratum surface height also varied independently of osteoblastic differentiation. These conflicting results suggests more investigation is needed to determine conclusively if substrate roughness and height significantly contribute and regulate osteogenesis.

Similar to substrate roughness and height, studies examining substrate wettability have yielded conflicting results. Although a correlation between substrate wettability and osteoblastic differentiation has been reported, the osteoblastic response observed has been inconsistent and varied depending on surface topography, chemistry, and the specific cell line being evaluated<sup>7,186</sup>. In the study presented here, surface wettability was not significantly altered between any of the substrates examined suggesting substrate wettability may not have as significant a role in regulating osteoblastic differentiation as previous studies have suggested<sup>11,118,187</sup>.

Particle density, unlike the other characteristics examined in this study, was significantly different on the 30% substrate compared to the other substrates examined. The 30% substrate had a particle density of 86 particles per centimeter, roughly 70 particles per centimeter greater than the 5% substrate and 80 less particles per centimeter than the 50% substrates, which had particle densities of 16 and 165 particles per centimeter, respectively. A study by Ahn *et al.* examined how nanopost density influenced osteogenic commitment of human mesenchymal stem cells (hMSCs) and observed a parabolic correlation between post-density and osteogenic differentiation<sup>12</sup>, similar to the response observed in this study. It was determined that lower and higher nanopost densities did not induce a sufficient amount of cell spreading to increase cell stiffness and induce osteogenic differentiation. Another study by Kuo *et al.* corroborated these findings. They determined that 500nm to 700nm nanopillars reduced apoptosis and increased focal adhesion formation to the greatest extent. They also determined that roughly 900nm between pillars was the ideal spacing to induce cell spreading<sup>181</sup>. Our findings, coupled with the previously mentioned studies, suggest that there is an optimal density, when using roughly 500nm topographic features that induces an increase in osteogenesis. However, the results observed in this study and others suggest that the relationship between substrate characteristics and osteogenesis is highly complex. It depends heavily on the specific materials, surface characteristics, cell type, and culture conditions being used, and further study is required before definitive assertions can be made as to which substrate characteristic is responsible for inducing osteogenesis.

Interestingly, in the previously mentioned studies that examined substrate characteristics there was a commonality, despite the conflicting results as to which substrate characteristic induces osteogenesis. The substrate that resulted in the greatest increase in osteoblastic differentiation also induced an increase in focal adhesion formation and maturation<sup>13,66,166</sup>. In a proliferative state, cells exhibit numerous, small, oblong focal adhesions. These adhesions probe the surrounding environment to evaluate the substrate. As the focal adhesions mature, they become larger and decrease in overall number. Upon investigation of the 30% HAp substrate, we observed similar changes that suggest a maturation of focal adhesions (Figure 14). This maturation was observed on the 30% substrate in conjunction with upregulation of key osteoblastic differentiation genes as well as increased AP activity, suggesting a relationship between focal adhesion maturation and osteoblastic differentiation. This suggests that while substrate surface characteristics may be variable, the substrate's ability to induce focal adhesion formation and maturation may be a key factor in regulating osteoblastic differentiation. Evidence of this interaction has been observed in previous studies examining cell adhesion complexes and osteogenesis<sup>188</sup>. However, these studies have failed to identify a mechanism by which focal adhesion maturation may contribute to the regulation of osteoblastic differentiation. This unknown question has been succinctly summarized in a review by Jamora and Fuches<sup>175,189–191</sup>. The question is as follows: it is known that disassociation of adhesion complexes occurs in response to various stimuli, but what happens to the proteins, such as  $\beta$ -catenin, that make up the adhesion complexes after disassociation? Do they participate in other facets of cell mechanotransduction, or are they broken down and recycled within the cell?

To probe the question posed by Jamora and Funches, we examined  $\beta$ -catenin sub-cellular localization over time. Interestingly on the pro-osteogenic substrate,  $\beta$ -catenin concentration remained high in the membrane after 24 hours before decreasing at 48 hours then returning to a concentration similar to that observed over the first 12 hours. At 48 hours,  $\beta$ -catenin concentration in cells on the pro-osteogenic substrate exhibited an increase in nuclear translocation of  $\beta$ -catenin, which coincided with the decrease in  $\beta$ -catenin at the membrane. After 48 hours nuclear  $\beta$ -catenin concentration returned to levels observed over the first 24 hours. Cells on TCPS exhibited the same shift of  $\beta$ -catenin from the membrane to the nucleus and then back to basal levels over a 24-hour period, similar to that observed on the pro-osteogenic substrate. However, unlike cells on the pro-osteogenic substrate, in cells on TCPS the shift of  $\beta$ -catenin from the membrane to the nucleus did not begin until 48 hours after seeding, 24 hours later than the pro-osteogenic substrate (Figure 15). This more rapid translocation of  $\beta$ -catenin in cells on pro-osteogenic substrate is likely due to one of the three mechanism discussed previously. The increase in nuclear localization of  $\beta$ -catenin at 48 hours on the pro-osteogenic substrate also coincided with an increase in TOPFLASH activity indicating an increase in TCF/LEF transcriptional activity, which is pivotal in the regulation of osteogenesis (Figure 15d). It is also worth noting that *AXIN2* gene expression closely mirrors the transcriptional activity of  $\beta$ -catenin as measured by the TOPFLASH reporter assay, further corroborating the observed changes (Figure 16a).

We further confirmed that the observed increase in AP activity on the pro-osteogenic substrate is, in part, a result of the more rapid translocation of  $\beta$ -catenin to the nucleus as well as the observed increase in transcriptional activity. Inhibiting  $\beta$ -catenin binding to TCF/LEF inhibits upregulation of downstream effector genes, many of which regulate osteoblastic differentiation<sup>60</sup>. Upon inhibition using PNU-74564, a significant decrease in *AXIN2* gene expression was observed in cells cultured on pro-osteogenic substrates and TCPS after 2 and 3 days, respectively (Figure 16a). Importantly, the significant increase in AP activity that is typically associated with the pro-osteogenic substrate was inhibited in cells cultured in the presence of PNU-74564 (Figure 16b). This suggests that the observed increase in AP activity is a consequence of the more rapid  $\beta$ -catenin translocation and increase in transcriptional activity. Taken together these results support our hypothesis that the osteogenic substrate we identified in this study induces the liberation of  $\beta$ -catenin from adhesion complexes allowing  $\beta$ -catenin to translocate to the nucleus and activate osteoblastic differentiation. This also provides further evidence that  $\beta$ -catenin bound at adhesion complexes and  $\beta$ -catenin that actively participates in intracellular signaling come from the same pool, a concept suggested by results from previous studies<sup>167</sup>.

We hypothesized that  $\beta$ -catenin, a protein bound at the cell adhesion complexes, is liberated and is then free to translocate to the nucleus where it can bind TCF/LEF and regulate osteogenic gene expression. Evidence from the study presented here, as well as previous studies, suggests one of three mechanism by which focal adhesions may mediate the observed change in  $\beta$ -catenin localization and activity. The first is that as

maturation of focal adhesions occurs, greater intracellular tension is generated. Increasing tensile force within the cells then causes disassociation of cadherin complexes therefore liberating  $\beta$ -catenin. This concept is supported by previous studies that have observed increased breakdown and turnover of E-cadherins in response to increased contractile activity<sup>16,63,192,193</sup>. The second is that  $\beta$ -catenin may participate in the binding of vinculin to actin filaments at focal adhesions similar to that observed at adherens junctions. As focal adhesion turnover occurs,  $\beta$ -catenin can then be liberated from the focal adhesion complexes. Recent studies suggest  $\beta$ -catenin interacts with paxillin during increased Rac1 activation, which occurs during focal adhesion turnover<sup>116,186</sup>. In addition, it is reasonable to suggest that  $\beta$ -catenin binds vinculin at focal adhesions in a manner similar to what is observed at adherens junctions, and then as turnover occurs it is liberated from the adhesion complex<sup>63,194,195</sup>. The third possibility is that while  $\beta$ -catenin may assist in focal adhesion formation and stabilization, and therefore localize at these locations, focal adhesions may mediate  $\beta$ -catenin translocation through a secondary messenger. One proposed mechanism is that focal adhesion phosphorylation, which occurs during adhesion turnover, causes AKT phosphorylation which then inhibits GSK-3 $\beta$ , a protein that phosphorylates  $\beta$ -catenin. The decreased  $\beta$ -catenin phosphorylation leads to an increase in cytosolic  $\beta$ -catenin and, in turn increased  $\beta$ -catenin nuclear translocation and activity<sup>124,174</sup>. However, this mechanism has only been examined in mesenchymal stem cells with respect to adipogenesis. It has not been evaluated in osteoblastic cells with respect to osteogenesis.

Further examination of the interplay between focal adhesion maturation,  $\beta$ -catenin shuttling, and osteoblastic differentiation is required to evaluate our hypothesized mechanism. Wnt signaling is known to be regulated by various stimuli and the study presented here does not encompass or evaluate the wide array of upstream and downstream Wnt targets such as AKT phosphorylation<sup>9,149,196</sup>. The studies discussed previously have observed noticeable changes in focal adhesion size and shape on pro-osteogenic substrates<sup>30</sup>. Unfortunately, the focal adhesions were not characterized fully for maturation and therefore do not allow for a determination to be made on the relationship between focal adhesion maturation and osteogenesis. Lastly, inhibition of this pathway further upstream, ideally at the focal adhesion complex, would provide greater insight into the mechanism by which  $\beta$ -catenin is liberated from focal adhesions. However, inhibitors that more directly interfere with  $\beta$ -catenin signaling or the focal adhesions cause significant phenotypic changes regardless of the substrate they are being cultured on, making experimental results difficult to interpret<sup>6,149</sup>.

## **CONCLUSION**

This study examined the role of substrate surface characteristics to determine if a singular characteristic was regulating osteoblastic differentiation. Additionally, this study examined the correlation between osteoblastic differentiation, focal adhesion formation and maturation, and suggested and evaluated a novel mechanism to explain this correlation. We found that one substrate, the pro-osteogenic 30% HA/PCL substrate, increased AP activity and expression of genes associated with osteoblastic differentiation as a result of

a more rapid translocation and increase in  $\beta$ -catenin transcriptional activity. We concluded that in this study only particle density, and therefore the distance between topographic features, was significantly different. Thus, our findings, in addition to information from previous studies<sup>11,12,45</sup>, suggest that particle density is possibly one substrate characteristic which regulates osteogenic potential. However, more study is needed as the relationship between substrates and osteogenesis is complex and depends on various factors such as cell type and substrate materials.

Cells on the 30% substrate also exhibited variations in focal adhesion formation and morphology, becoming larger and more eccentric compared to cells on all other substrates. These observations are indicative of focal adhesion turnover and maturation and similar to those seen on other pro-osteogenic substrates. Additionally, we found that there is a translocation of  $\beta$ -catenin from the membrane fraction at 24 hours to the nuclear fraction at 48 hours on pro-osteogenic substrate, 24 hours earlier than that which was observed in cells on TCPS. Furthermore,  $\beta$ -catenin was not only more localized to the nucleus on 30% HA/PCL, but it also bound TCF/LEF more frequently, indicating increased  $\beta$ -catenin transcriptional activity. It was further determined that by inhibiting  $\beta$ -catenin binding of TCF/LEF, the increase in osteoblastic differentiation typically observed in cells cultured on the pro-osteogenic substrate was inhibited. Taken together these results suggest that as focal adhesions mature, reducing in number in response to topography, the liberated  $\beta$ -catenin is then translocated to the nucleus and actively binds TCF/LEF. This would indicate that a focal adhesion initiated  $\beta$ -catenin mediated mechanism contributes to the transduction of substrate surface characteristics. More



study is required to determine which of the three possible mechanisms described previously of  $\beta$ -catenin and focal adhesion interaction are occurring and causing the observed  $\beta$ -catenin translocation and enhanced osteogenic response.

**CHAPTER 6. Inhibition of Focal Adhesion Turnover Prevents  
Osteoblastic Differentiation through  $\beta$ -catenin Mediated  
Transduction of Pro-Osteogenic Substrate**

## ABSTRACT

The mechanism by which substrate surface characteristics are transduced by osteoblastic cells and their progenitors is not fully known. Data from previous studies by our group suggests the involvement of  $\beta$ -catenin in the mechanism by which substrate surface characteristics are transduced. This focal adhesion initiated,  $\beta$ -catenin mediated mechanism functions as  $\beta$ -catenin is liberated from focal adhesion complexes as turnover in response to pro-osteogenic substrates occurs. After liberation,  $\beta$ -catenin can translocate and participate in the upregulation genes associated with osteogenesis. Unfortunately, determining if the observed correlation between focal adhesion turnover and  $\beta$ -catenin translocation was a direct result of focal adhesion turnover was challenging. In this study we inhibited focal adhesion turnover using a FAK inhibitor PF-573228. We found that inhibition of focal adhesion turnover resulted in an abrogation of the more rapid translocation and increased transcriptional activity of  $\beta$ -catenin induced by pro-osteogenic substrate. In addition, inhibition of focal adhesion turnover mitigated the increase in osteoblastic differentiation induced by pro-osteogenic substrate as measured by alkaline phosphatase enzymatic activity and key protein and gene expression. Together, these data coupled with previous findings suggests that the observed  $\beta$ -catenin translocation is a result of focal adhesion turnover, providing evidence for the proposed focal adhesion initiated,  $\beta$ -catenin mediated mechanism of substrate surface transduction.

## INTRODUCTION

Ongoing development of biomaterials for use in orthopedics and bone tissue engineering has yielded promising results through the modification of substrate surface characteristics<sup>43,197</sup>. Surface modifications that are typically include grit blasting, acid etching, anodization, and plasma spraying with either metal or osteoconductive materials such as hydroxyapatite<sup>59</sup>. These modifications aim to increase the surface roughness, wettability, and protein absorbance of the substrate. However, studies investigating biomaterial characteristics have not come to a consensus as to how

implant and substrate surface characteristics are transduced by bone cells and their progenitors<sup>11</sup>. Such information would allow for optimization of biomaterial characteristics for osteogenesis and osteointegration. Focal adhesions are well-known mechanosensors, regulating force and load-responsive transcription factors in osteoblastic cells in response to changes in intracellular tension and external stimuli<sup>12</sup>. Previous studies suggest changes in focal adhesions and changes in the cytoskeleton may at least partly contribute to the mechanism by which substrates are transduced<sup>59,173</sup>.

Focal adhesion complexes are located at the membrane of the cell and bridge the gap between the extracellular matrix (ECM) and the intracellular environment<sup>15</sup>. Cell signaling from the ECM to the intracellular compartment is mediated by focal adhesions and other transmembrane cell receptors, such as cadherins<sup>13,60,61</sup>. Various cell pathways including matrix assembly, cell migration, and spatially organized signaling are regulated by these adhesions<sup>63,198</sup>. Focal adhesions also share many proteins including vinculin and  $\alpha$ -catenin with cadherins as well and binds the actin cytoskeleton in a similar manner to cadherins<sup>199</sup>. Interestingly, one of the proteins that localize at cadherins is  $\beta$ -catenin<sup>199</sup>. At cadherin complexes  $\beta$ -catenin stabilizes the  $\alpha$ -catenin and vinculin complex to allow binding to the actin cytoskeleton<sup>200,201</sup>. This suggests it may a similar role at focal adhesion complexes.

The accumulation of  $\beta$ -catenin in the cytoplasm and stimulation of its release results in translocation to the nucleus, where it regulates pro-osteoblastic gene expression<sup>201</sup>. The importance of  $\beta$ -catenin in the promotion of osteogenesis and bone development is highlighted in a study Case *et al*<sup>43,58</sup>. They observed that  $\beta$ -catenin-deficient bone cells developed poor skeletal structures. Further, treatment with lithium chloride, prevents inactivation of  $\beta$ -catenin, enhanced the response of bone cells to mechanical signals<sup>174</sup>. These results highlight the vital role  $\beta$ -catenin plays in bone formation.

Focal adhesion kinase (FAK) activation is also a prominent signaling mechanism via ECM-integrin interactions that enhance the Wnt/ $\beta$ -catenin signaling pathway in bone

cells<sup>58</sup>. These data suggest a relationship between focal adhesions, FAK, and  $\beta$ -catenin-transcription mediated and mechanical activation of osteogenesis. However, despite the extensive research on FAK and  $\beta$ -catenin's role in transduction of pro-osteogenic substrate(s) (POS), the mechanism by which the transduction occurs is still unknown<sup>58</sup>.

To better understand this mechanism, it is essential to understand the interaction between substrate surface characteristics and their resulting effect on cell FA turnover and  $\beta$ -catenin translocation. Evidence shows that substrates with varying surface densities influence FA maturation and differentiation<sup>202</sup>. A previous study by our group characterized various substrates that combined polycaprolactone (PCL) and varying wt./wt. concentrations of hydroxyapatite particles (HAp)<sup>58</sup>. We determined that the 30% HAp/PCL substrate induced significantly more osteoblastic differentiation. Upon further evaluation, we observed greater focal adhesion maturation and more turnover of focal adhesions on the 30% HAp/PCL substrate, referred here as the pro-osteogenic substrate (POS), compared to all other substrates examined. Interestingly, this turnover and maturation of focal adhesion coincided with a more rapid translocation of  $\beta$ -catenin from the membrane-bound protein fraction to the nucleus<sup>58</sup>. This led us to hypothesize a novel mechanism by which substrate surface characteristics are transduced by osteoblastic cells. We hypothesized that the mechanism by which this occurs may involve the regulation of  $\beta$ -catenin by, or liberation from, proteins at focal adhesion complexes, located at the cell membrane. This would result in increased  $\beta$ -catenin translocation from these focal adhesion complexes to the nucleus on the more osteogenic substrate. We have previously evaluated this proposed focal adhesion initiated,  $\beta$ -catenin mediated mechanism<sup>202</sup>. However, to evaluate the more rapid translocation of  $\beta$ -catenin is a consequence of the observed focal adhesion turnover, focal adhesion turnover would need to be differentially regulated, and the resulting  $\beta$ -catenin translocation examined. We hypothesized that inhibition of focal adhesion turnover would result in a decrease in osteoblastic differentiation, a delay in the translocation of  $\beta$ -catenin from the membrane-bound protein fraction to the nucleus, and

a decrease in nuclear activity in cells cultured on POS compared to cells cultured on POS without FAK inhibition.

To evaluate this hypothesis, we examined the effect of a focal adhesion inhibitor, PF-573228, which is known to inhibit focal adhesion turnover *in vitro*<sup>202</sup>, on osteoblastic differentiation, focal adhesion turnover and maturation, and  $\beta$ -catenin localization and activity over time on a previously examined POS<sup>93,97</sup>. We observed that cells cultured on the POS displayed increased osteoblastic differentiation, greater focal adhesion maturation, a more rapid (24 hours) translocation of  $\beta$ -catenin from the membrane-bound fraction to the nuclear fraction, and greater nuclear activity compared to cells cultured on tissue culture polystyrene (TCPS), corroborating previous findings<sup>7,57,58</sup>. However, upon addition of the FAK inhibitor, focal adhesion turnover was significantly inhibited, the rapid translocation of  $\beta$ -catenin was prevented, and osteoblastic differentiation was significantly downregulated. Indeed, cells cultured on POS in the absence of FAK inhibitor more closely mimicked cells cultured on TCPS in the absence of FAK inhibition.

## **MATERIALS AND METHODS**

### **Materials.**

All chemicals used for nanoparticle and substrate synthesis were obtained from Sigma-Aldrich (St. Louis, MO).

### **Substrate Synthesis.**

#### *Polycaprolactone and Hydroxyapatite Substrate Synthesis.*

To create a pro-osteogenic substrate (POS), we synthesized a substrate composed of PCL and hydroxyapatite particles in a ratio that was determined previously to be optimally osteogenic<sup>58</sup>. Briefly, five thousand molecular weight PCL was suspended at a 2.5% wt./vol. ratio in chloroform. The mixture was then homogenized until all PCL was dissolved into solution. After homogenization, 500nm HAp was added to the solution at a ratio of 30% wt./wt. with the PCL. Using a dip-coating technique, 22 mm coverslips were

coated and allowed to dry at room temperature for 24 hours. Prior to use all substrates were submerged in 70% ethanol for 5 minutes before the ethanol was aspirated and samples allowed to air dry. After drying samples were exposed to ultraviolet light for 1 hour.

### **Cell Characterization.**

#### *Osteoblast Cell Culture.*

To assess osteogenesis, the differentiation capacity of human fetal osteoblasts (hFOB 1.19 cells), a preosteoblastic cell line, was assessed as previously described. Briefly, for proliferation of hFOB 1.19 cells, cells were cultured at 33.5°C with 5% CO<sub>2</sub> to 80% confluence in standard DMEM:F12 media supplemented with 10% fetal bovine serum (Gibco, Gaithersburg, MD) and 1% Penicillin/Streptomycin mixture (Sigma, St. Louis, MO). To induce differentiation of the hFOB 1.19 cells, the standard media was supplemented with 100µg/mL ascorbic acid, 10<sup>-8</sup> M menadione, and 10<sup>-8</sup> M dihydroxy-vitamin D3 (Sigma, St. Louis, MO), and the cells were cultured at 39.5°C with 5% CO<sub>2</sub> until the desired timepoint. In experiments where we focal adhesion kinase (FAK) inhibitor, PF-573228, which is known to inhibit focal adhesion turnover *in vitro*<sup>58</sup>, was suspended in dimethyl sulfoxide (DMSO), and added to differentiation media at a molar concentration of 200nM. This concentration was determined based on levels of focal adhesion kinase phosphorylation activity at varying FAK inhibitor concentrations (Supplemental Figure S7). In addition, an identical amount of DMSO without FAK inhibitor was added to control media. Media was changed every 3 days unless otherwise stated for all experimental methods.

#### *Alkaline Phosphatase (AP) Activity.*

hFOB 1.19 cells were cultured on either TCPS or the pro-osteogenic substrate in either the presence or absence of the FAK inhibitor PF-573228 at 15,000 cells/cm and cultured under differentiation conditions for 7 days. Differentiation was evaluated using a colorimetric AP enzymatic activity assay as previously described. Briefly, cells were freeze thawed in 400µL of 0.05% Triton X-100 in phosphate buffered saline twice and then the cell lysate collected. 10µL of each sample lysate was removed and used to

quantify total protein concentration using Pierce BCA protein assay kit (Thermo Fisher, Waltham, MA). AP enzymatic activity was then determined by conversion of p-nitrophenyl phosphate to p-nitrophenol. 200 $\mu$ L of AP reaction buffer was then added to each sample and incubated at room temperature for 30 minutes. After incubation 50 $\mu$ L of each sample was placed in 200 $\mu$ L of 0.1 NaOH in a 96 well-plate to quench the reaction. All samples were then assessed at 410nm and SIGMA units calculated based on the standard curve. All readings were then normalized to total protein concentration to control for variations in cell number between samples.

#### *Osteoblastic Gene Expression.*

hFOB 1.19 cells were seeded on TCPS or the POS in either the presence or absence of the FAK inhibitor PF-573228 at 100,000 cells/cm<sup>2</sup> and cultured under differentiation conditions for 1 and 7 days. At each time point RNA was isolated using a RNeasy Mini Kit (Qiagen, Hilden, Germany). Quantitative real time PCR (RT-qPCR) was performed using a C1000 Touch Thermal Cycler with CFX96 Real-Time System (Bio-Rad Laboratories, Hercules, CA). PowerUp Sybr Green Master Mix was used to quantify gene expression (Thermo Fisher Scientific). The genes we evaluated are associated with the various stages of osteoblastic differentiation and are as follows; alkaline phosphatase (*ALPL*), Osteocalcin (*BGLAP*), Collagen1-A1 (*COL1A1*), Runt related transcription factor-2 (*RUNX2*), and Sp7 Transcription Factor (*SP7*). Glyceraldehyde-3-Phosphate Dehydrogenase (*GAPDH*) was used as a reference gene for all samples. All primers used in this study were PrimePCR Sybr Green Assay Primers (Bio-Rad Laboratories, Hercules, CA) and the unique assay ID numbers are provided in Table 5. The  $\Delta\Delta$ Ct method was used to quantify fold-change in gene expression relative to the housekeeping gene *GAPDH*, as previously described.

#### *Focal Adhesion Kinase Activity.*

hFOB 1.19 cells were cultured on either TCPS or the pro-osteogenic substrate at 100,000 cells/cm and cultured under differentiation conditions for 12 hours, 24 hours, 48 hours, 72 hours, or 96 hours. At each time point protein was harvested as previously described. Briefly, 400 $\mu$ L of a solution of 1x RIPA buffer and protease inhibitor cocktail (Thermo



Fisher, Waltham, MA) was placed into each well for 15 minutes on ice. After 15 minutes, the wells were scrapped using a cell scrapper and the cell slurry was then moved to a 1.5mL conical tube. The cells were then lysed further by pipetting cells 10 times through a 21-gauge needle. Cells were then centrifuged at 13,000 RPM for 20 minutes and the supernatant harvested. Cell lysate was then analyzed for focal adhesion kinase activity using FAK (Total) Human ELISA Kit and FAK (Phospho)[pY397] Human ELISA Kit (Thermo Fisher, Waltham, MA). Phosphorylated FAK was normalized to total FAK in each sample.

#### *Focal Adhesion Staining.*

hFOB 1.19 cells were cultured on TCPS or the POS in either the presence or absence of the FAK inhibitor PF-573228 at 15,000 cells/cm and cultured under differentiation conditions for 12 hours, 24 hours, 48 hours, 72 hours, or 96 hours. At the selected time point, cells were stained using ab196454, an anti-vinculin antibody conjugated to AlexaFluor 488 (Abcam, Cambridge, United Kingdom). Briefly, cell culture medium was removed, and cells were fixed in 4% paraformaldehyde for 15 min at room temperature. After fixation, cells were washed twice with wash buffer consisting of 0.05% Tween-20 in PBS. Cells were then permeabilized with 0.1% Triton-X100 in PBS for 5 minutes. After permeabilization cells were washed twice with wash buffer and then blocked for 1 hour at room temperature in Odyssey Blocking Buffer (Thermo Fisher Scientific, Waltham, MA). After blocking anti-vinculin antibody was diluted to 1:250 in blocking buffer and incubated overnight at room temperature. Cells were then washed three times in wash buffer. DAPI stain, diluted at 1:1,000 in PBS, was added and incubated at room temperature for 5 minutes. After incubation samples were mounted on glass slides using ProGold Antifade Mounting Solution (Thermo Fisher Scientific, Waltham, MA). Representative images for each group and timepoint are shown in supplemental figure S8.

#### *Focal Adhesion Characterization.*

Confocal images of the various samples were gathered using an LSM 710 Confocal Microscope (Zeiss, Jena, Germany). Using custom MATLAB-based software, images were analyzed for focal adhesion size and morphology, and number normalized to cell

number. A contrast threshold of 0.450 was selected and applied to all images allowing segmentation of the individual focal adhesions. If the segmentation did not accurately represent the original image, a different threshold value was chosen manually until segmentation of the focal adhesions was representative of the original images. Thresholding analysis was then performed and focal adhesion number, length and width dimensions ( $\mu\text{m}$ ), and area ( $\mu\text{m}^2$ ) were output and recorded.

#### *GTPase Activity.*

hFOB 1.19 cells were seeded on the pro-osteogenic substrate at 100,000 cells/cm<sup>2</sup> and cultured under differentiation conditions for 4 hours, 12 hours, 24 hours, 48 hours, and 72 hours. After culture, cells were lysed in accordance with the protocol from the G-LISA Activation Assay Kit (Cytoskeleton Inc., Denver, CO) for RhoA, Rac1, or Cd42. 10 $\mu\text{L}$  of each sample lysate was removed and used to quantify total protein concentration using Pierce BCA protein assay kit (Thermo Fisher, Waltham, MA). Cell lysates were then examined using either the RhoA, Rac1, or Cd42 G-LISA activation assay kits as per the designated protocol and GTPase activity quantified. All cell fractions were normalized to total protein content.

#### *$\beta$ -Catenin Cellular Dynamics.*

hFOB 1.19 cells were seeded on TCPS or the pro-osteogenic substrate in either the presence or absence of the FAK inhibitor PF-573228 at 100,000 cells/cm<sup>2</sup> and cultured under differentiation conditions for 4, 12, 24, 48, 72, or 96 hours. After culture, cells underwent protein fractionation using the Subcellular Protein Fractionation kit for Cultured Cells (Thermo Fisher Scientific, Waltham, MA). After fractionation, 10 $\mu\text{L}$  of cell lysate from each fraction was removed and used to quantify total protein concentration using a Pierce BCA protein assay kit (Thermo Fisher, Waltham, MA). 25 $\mu\text{g}$  of total protein from each cell fraction at the various time points was then used to quantify total  $\beta$ -catenin protein concentration in the various cell fractions over time using a Human Total  $\beta$ -catenin DuoSet IC ELISA (R&D Biosystems, Minneapolis, MN). All cell fractions were then normalized to total  $\beta$ -catenin concentration at the respective timepoints.

### *Luciferase Based $\beta$ -Catenin Translocation Reporter Assay.*

To validate nuclear  $\beta$ -catenin translocation and activity from cell fractionation experiments, hFOB 1.19 cells were examined using a luciferase-based reporter assay (Promega Corporation, Madison, WI) as previously described. Briefly, hFOB1.19 cells were transiently transfected with either a TOPFLASH reporter construct, which contains a firefly luciferase reporter that is activated by TCF/LEF binding or a FOPFLASH reporter construct, which has a mutated TCF/LEF protein that prevents  $\beta$ -catenin activation of the firefly reporter. After 24 hours, 100,000/cm<sup>2</sup> cells were seeded onto either TCPS or the pro-osteogenic substrate in the presence or absence of the FAK inhibitor, PF-573228, and cultured for 12 hours, 24 hours, 48 hours, 72 hours or 96 hours. After culture, the cells were lysed and a TOPFLASH/FOPFLASH quantified.  $\beta$ -catenin translocation and activity in cells on TCPS or the pro-osteogenic substrate in the presence or absence of the FAK inhibitor was then calculated.

## **RESULTS**

### **Osteoblastic Differentiation and FAK Activity are Increased in Cells Cultured on POS in the Absence of Focal Adhesion Kinase Inhibitor.**

We first wanted to corroborate previous findings demonstrating that cells cultured on POS display greater osteoblastic differentiation than cells cultured on TCPS. hFOB1.19 cells were cultured on TCPS or POS in the absence of FAK inhibitor and AP enzymatic activity quantified at 1, 3, and 7 days (Figure 17). After 1 day in culture, cells cultured on POS exhibited a significant 1-fold increase in AP enzymatic activity compared to cells cultured on TCPS. After 3 and 7 days in culture, cells cultured on POS again exhibited a significantly greater 2-fold and 1-fold increase in AP enzymatic activity, respectively, compared to cells cultured on TCPS. Moreover, the total increase in AP enzymatic activity from day 1 to day 7 was greater in cells cultured on POS (.069 U/ $\mu$ G) compared a in cells cultured on TCPS (.039 U/ $\mu$ G) suggesting greater osteoblastic differentiation in cells culture on POS overall.

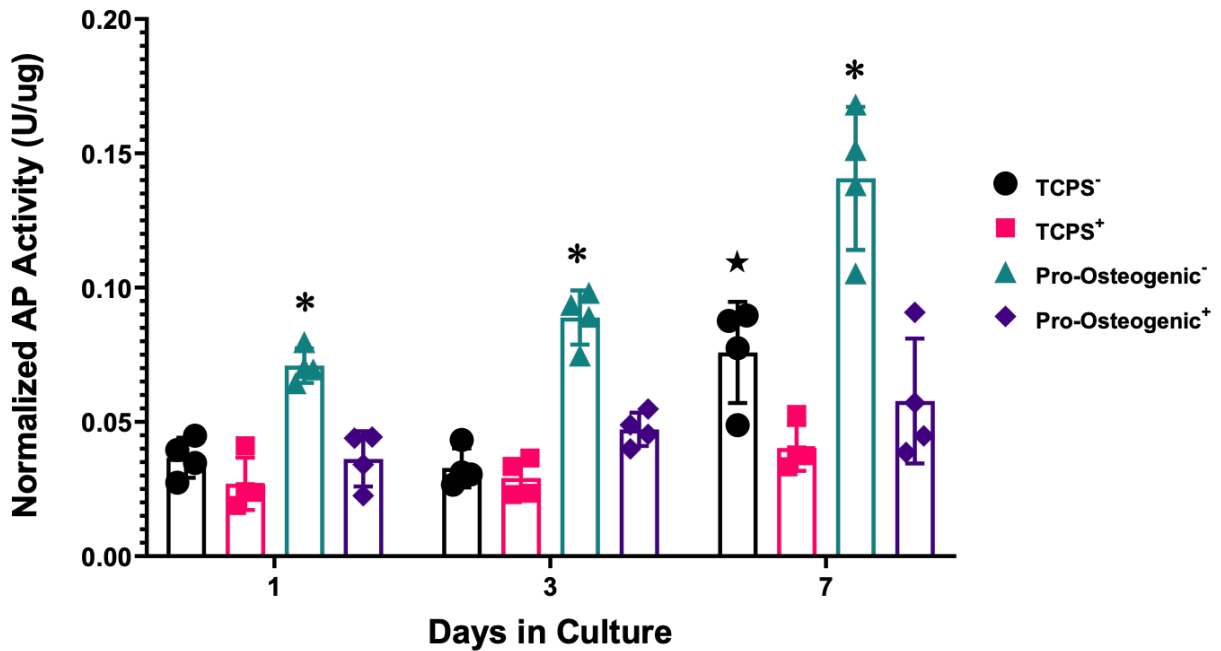


**Figure 17.** Normalized alkaline phosphatase enzymatic activity of hFOB 1.19 preosteoblastic cells cultured on TCPS or Pro-Osteogenic substrate in the presence (+) or absence (-) of FAK inhibitor PF-573228 after 1, 3, and 7 days in culture. Significance is considered  $p < 0.05$  only within the same timepoint. \* = significantly different than all other groups, \$ = significantly different than TCPS<sup>-</sup>, ★ = significantly different than TCPS<sup>+</sup>, x = significantly different than Pro-Osteogenic<sup>+</sup>.  $n = 4$  samples with each sample being the average of two replicates.

We then assessed gene expression of key osteoblastic differentiation markers after 1 and 7 days in culture in cells cultured on TCPS or POS in the absence of FAK inhibitor (Figure 18). At day 1 no significant differences were observed between cells cultured on TCPS and cells cultured on POS in the absence of FAK inhibitor. At day 7, gene expression of *ALPL*, *COL1A1*, *RUNX2* was significantly increased in cells cultured on POS compared to cells cultured on TCPS in the absence of FAK inhibitor, similar to what has been observed previously. The roughly 1-fold increase in expression observed in *ALPL*, *BGLAP*, and *RUNX2* also suggest a greater maturation of osteoblasts cultured on POS compared to those cultured on TCPS, as these markers are indicative of mature osteoblast differentiation.

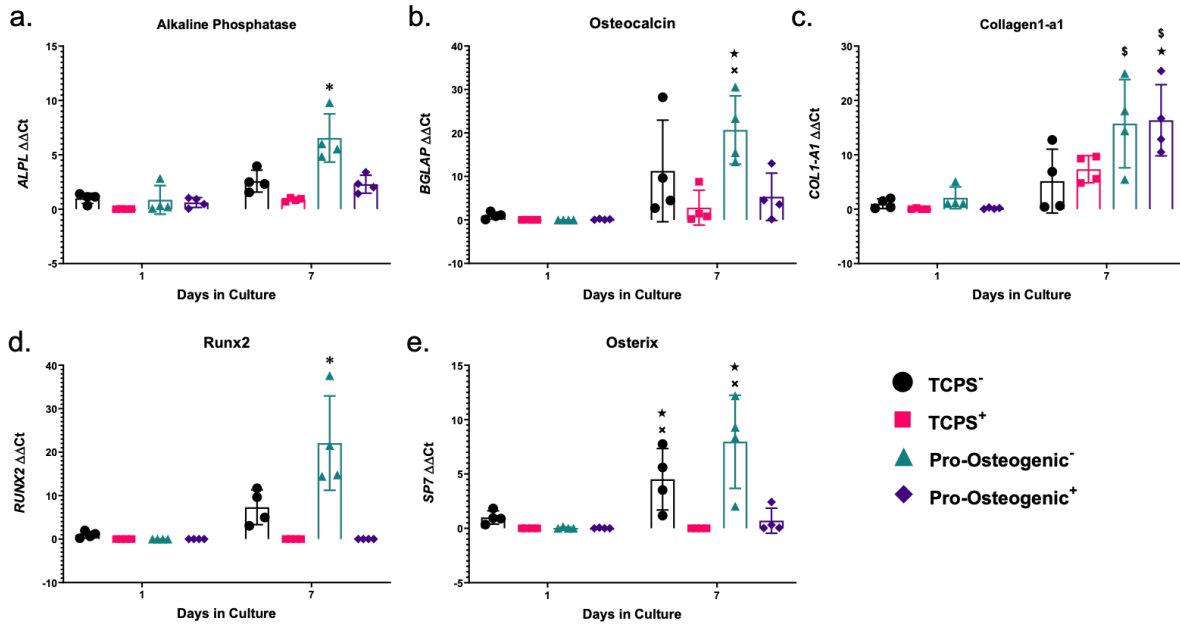


**Figure 18.** Osteoblastic gene expression on TCPS or Pro-Osteogenic substrate in the presence (+) or absence (-) of FAK inhibitor PF-573228. Evaluation of osteoblastic gene expression of (a) Alkaline Phosphatase (*ALPL*), (b) Osteocalcin (*BGLAP*), (c) Collagen1-a1 (*COL1A1*), (d) *RUNX2*, and (e) Osterix (*SP7*) at 1 and 7 days in culture. Significance is considered  $p < 0.05$  only within the same timepoint. \* = significantly different than all other groups, \$ = significantly different than TCPS<sup>-</sup>, ★ = significantly different than TCPS<sup>+</sup>, x = significantly different than Pro-Osteogenic<sup>+</sup>. n = 4 samples with each sample being the average of two replicates.

To determine if the observed changes in gene expression correlated to changes in protein expression, we examined the expression of key proteins indicative of osteoblastic differentiation in cells cultured on TCPS and POS in the absence of FAK inhibitor (Figure 19). At day 1, no significant differences, in any protein examined, was observed between cells cultured on TCPS and cells cultured on POS. At day 3 however, cells cultured on POS exhibited a 3-fold increase in the COL1A1 protein expression (Figure 19a), a marker of early commitment to the osteoblastic lineage. Neither Osteocalcin (OCN) nor Osteopontin (OPN) were significantly regulated at day 3 between cells cultured on POS and cells cultured on TCPS. At day 7 all proteins examined were significantly upregulated in cells cultured on POS compared to cells cultured on TCPS. Cells cultured on POS in the absence of FAK inhibitor exhibited a roughly 1-fold increase in both OCN (Figure 19b) and OPN (Figure 19c), both indicative of mature osteoblastic differentiation, and a 0.5-

fold increase in COL1A1 protein expression compared to cells cultured on TCPS. These data coupled with both the AP enzymatic activity and gene expression data confirms that cells cultured on the POS differentiate significantly more compared to cells cultured on TCPS as previously observed<sup>58</sup>.

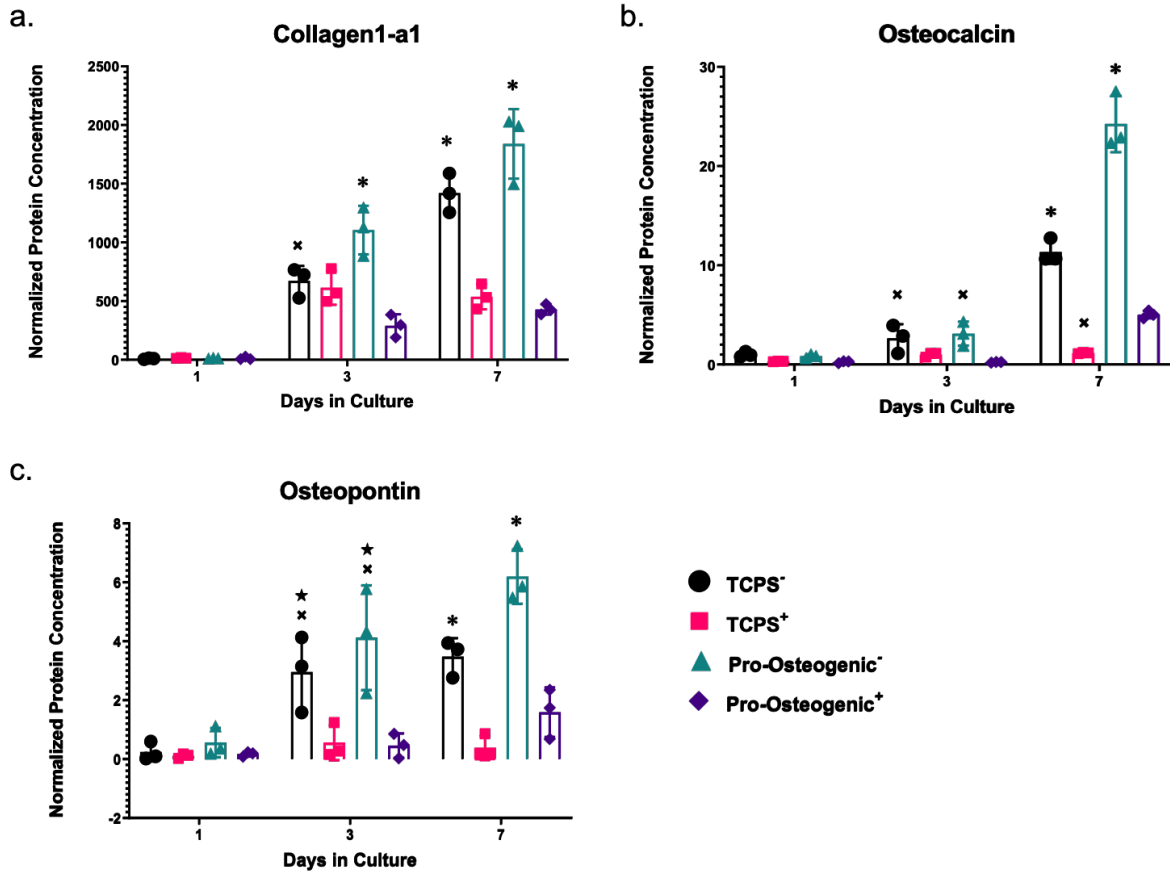


**Figure 19.** Osteoblastic protein expression on TCPS or Pro-Osteogenic substrate in the presence (+) or absence (-) of FAK inhibitor PF-573228. Evaluation of normalized expression of proteins related to osteoblastic differentiation (a) Collagen1-a1 (COL1A1), (b) Osteocalcin (OCN), and (c) Osteopontin (OPN) at 1, 3 and 7 days in culture. Significance is considered  $p < 0.05$  only within the same timepoint. \* = significantly different than all other groups, \$ = significantly different than TCPS-, ★ = significantly different than TCPS+, x = significantly different than Pro-Osteogenic+. n = 3-4 samples with each sample being the average of three replicates.

After confirming that POS induced significantly greater osteoblastic differentiation compared to TCPS, we then examined FAK activity (Figure 20). Normalized FAK activity was quantified by examining concentration of phosphorylated FAK divided by total

concentration of FAK over time in cells cultured on TCPS and cells cultured on POS in the absence of FAK inhibitor. We observed significant increases in normalized FAK phosphorylation at 24 hours in cells cultured on POS compared to cells cultured on TCPS. The observed increase remained until 72 hours, where normalized FAK phosphorylation then decreased and was significantly less in cells cultured on POS relative to cells cultured on TCPS. Interestingly, cells cultured on POS and TCPS followed a similar trend. Normalized FAK phosphorylation over time increased and remained elevated for 48 hours before returning to basal level, with the POS inducing a more rapid increase in FAK phosphorylation. Interestingly, activation levels of Rac1, Cd42, and RhoA, GTPases, which participate in actin cytoskeleton and focal adhesion formation<sup>51</sup>, were unchanged over the course of 72 hours (Supplemental Figure S9).

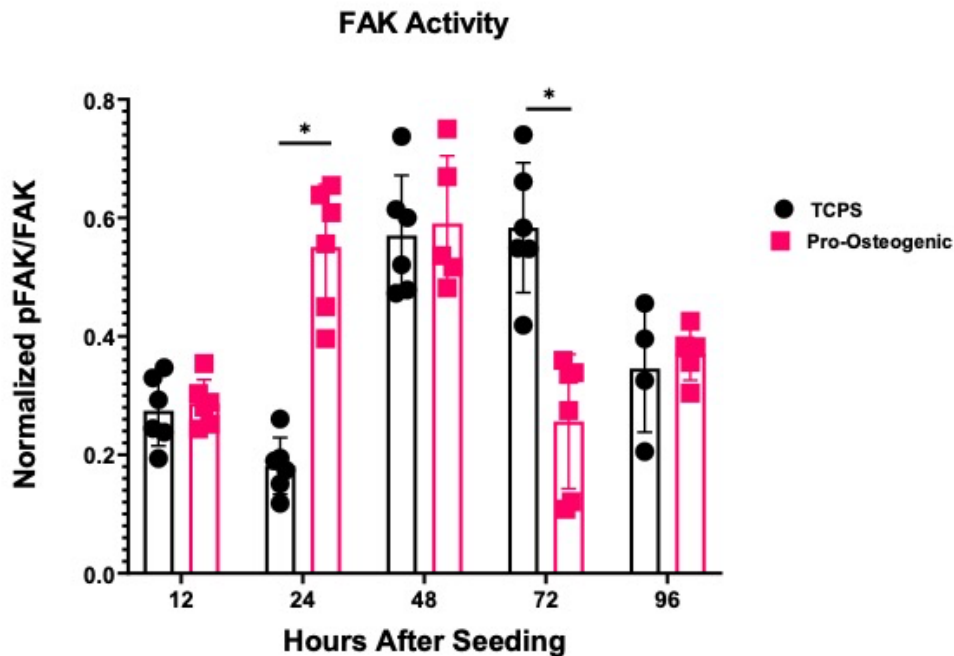


**Figure 20.** Focal adhesion kinase activity over 96 hours in hFOB 1.19 cells cultured on either TCPS or Pro-Osteogenic substrate. Significance is considered  $p < 0.05$  only within the same timepoint.  $n = 6$  samples.

### Inhibition of Focal Adhesion Turnover Prevents Pro-Osteogenic Substrate Induced Increase in Osteoblastic Differentiation.

To examine the role of focal adhesion turnover in the proposed mechanism, we exposed cells to the FAK inhibitor, PF-573228, that prevents focal adhesion turnover *in vitro*<sup>58</sup>. To

confirm the concentration of inhibitor necessary to prevent FAK phosphorylation we examined FAK phosphorylation using ELISA at 3 different concentrations 100nM, 150nM, and 200nM in cells cultured on TCPS (Supplemental Figure S7). We observed significant decreases in normalized FAK phosphorylation at a 200nM concentration and therefore 200nM was used for all following experiments.

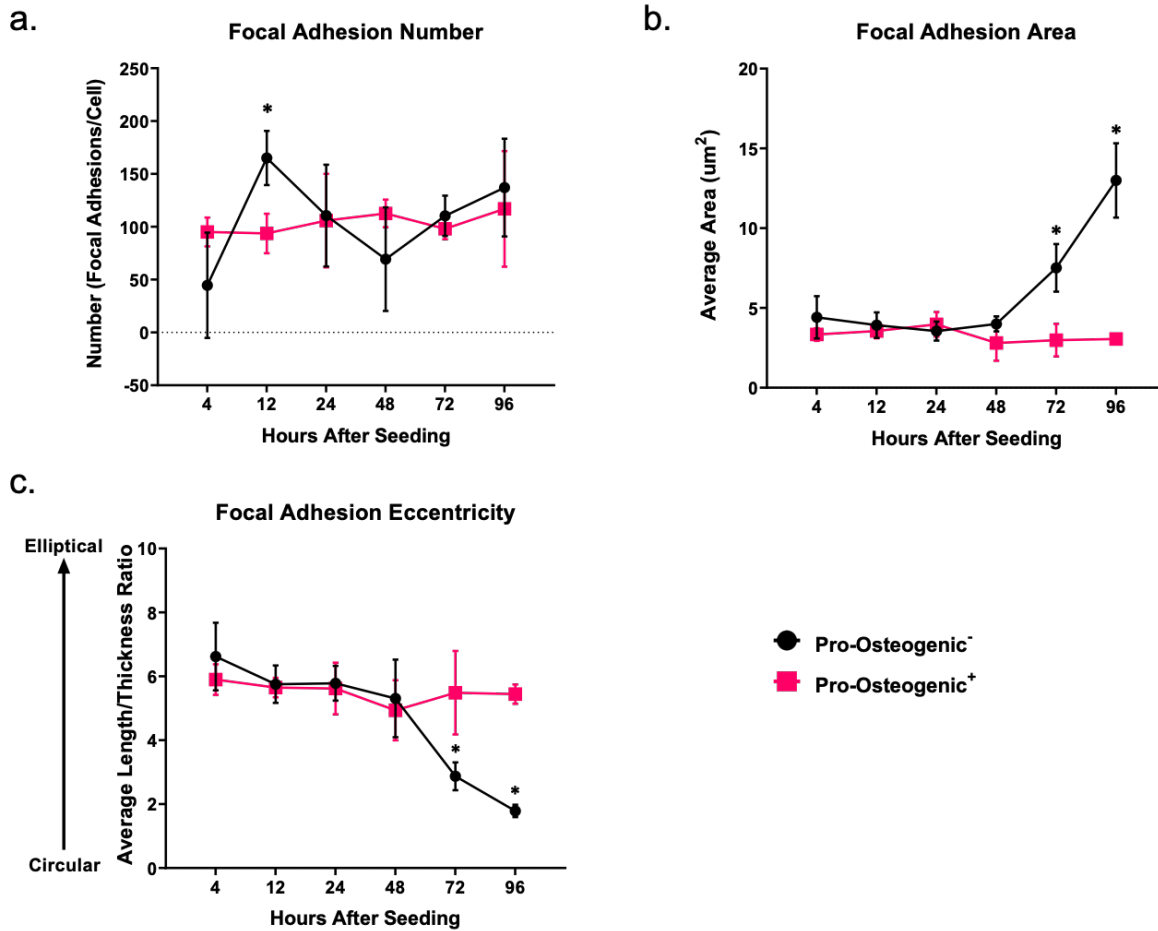


**Figure 21.** Focal adhesion number, size, and morphology over time in hFOB 1.19 cells cultured on either TCPS or Pro-Osteogenic substrate in the presence (+) or absence (-) of FAK inhibitor PF-573228. (a) number, (b) area, and (c) eccentricity of focal adhesions examined. Significance is considered  $p < 0.05$  only within the same timepoint. \* = significantly different than all other groups.  $n = 3$  samples with each sample consisting of 2-3 replicates. Each image consists of 500-5000 focal adhesions and between 5-50 cells per image.

To evaluate changes in focal adhesion turnover and maturation, we first examined how introduction of FAK inhibitor to cells cultured on POS would affect focal adhesion number,



area, and eccentricity over time. We observed that from 4 hours to 12 hours after seeding in cells cultured on POS in the absence of FAK inhibitor that a significant increase (approximately 100 adhesions per cell) in focal adhesion number occurred (Figure 21a). This number then decreased over the next 36 hours to roughly 75 adhesions per cell before again increasing to approximately 150 adhesions/cell. As expected, this cyclical pattern was not observed in cells cultured on POS in the presence of FAK inhibitor where the number of focal adhesions over time remained relatively stable at 100 adhesions per cell. In addition, cells cultured on POS in the absence of FAK inhibitor became significantly larger between 48 hours and 96 hours, increasing in size roughly 10 $\mu$ m (Figure 21b). This increase in area was not observed in cells cultured on POS in the presence of FAK inhibitor, with significantly smaller adhesions being present at 72 hours and 96 hours after cell seeding compared to cells cultured in the absence of FAK inhibitor. Moreover, as previously reported<sup>58</sup>, adhesion eccentricity decreased (became more circular) in cells cultured on POS in the absence of FAK inhibitor at 72 hours and 96 hours after cell seeding compared to cells cultured in the presence of FAK inhibitor (Figure 21c). These data suggests that the FAK inhibitor was preventing focal adhesion turnover and maturation over time, as typically resulted from culturing of cells on the POS.

Following the observation that FAK inhibitor was in fact, preventing focal adhesion turnover and maturation, we then wanted to examine how the introduction of FAK inhibitor to cells cultured on POS affected osteoblastic differentiation. We observed, in cells cultured in the presence of FAK inhibitor on POS, a significant reduction in AP enzymatic activity at all timepoints compared to cells cultured on POS in the absence of FAK inhibitor (Figure 19). In addition, AP enzymatic activity was not significantly different in cells cultured on POS in the presence of FAK inhibitor and cells cultured on TCPS in the absence of inhibitor. This suggests that inhibition of FAK mitigates the positive effects POS has on AP enzymatic activity. Interestingly, introduction of FAK inhibitor to cells cultured on TCPS did not result in a significant change in AP activity compared to cells cultured on TCPS in the absence of the inhibitor.

We next examined osteoblastic gene expression in the presence and absence of FAK inhibitor. At day 1 no differences were observed in cells cultured on TCPS or POS regardless of the presence or absence of FAK inhibitor. However, at day 7 gene expression for *ALPL*, *OCN*, *RUNX2*, and *SP7* in cells cultured in the presence of FAK inhibitor on the POS was significantly reduced compared to cells cultured on POS in the absence of FAK inhibitor. Unlike all other genes examined, *COL1A1* gene expression was upregulated in cells cultured on both TCPS and POS in the presence of FAK inhibitor at day 7 to levels similar to, if not slight greater, those observed in cells cultured on the same substrate in the absence of FAK inhibitor.

Lastly, we examined expression of key osteoblastic proteins over time in cells cultured on TCPS and POS in the presence and absence of FAK inhibitor. In cells cultured on POS in the presence of FAK inhibitor compared to cells cultured on POS in the absence of FAK inhibitor at day 3 we observed a significant 3-fold, 3-fold, and 4-fold reduction of *COL1A1*, *OCN*, and *OPN* protein expression, respectively. In cells cultured on TCPS, only *OPN* was significantly downregulated by the presence of FAK inhibitor at day 3. At day 7, similar to what we observed in osteoblastic gene expression, we observed a significant 4-fold and 3-fold reduction in *OCN* and *OPN*, respectively, in cells culture on POS in the presence of FAK inhibitor compared to cells cultured on POS in the absence of FAK inhibitor. We observed similar results in cells cultured on TCPS in the presence of FAK inhibitor at day 7, with a significant reduction in protein expression in both *OCN* and *OPN* compared to cells cultured in the absence of FAK inhibitor. Interestingly, conversely to what was observed in gene expression, *COL1A1* protein expression was significantly downregulated (4-fold) in cells cultured on POS in the presence of FAK inhibitor compared to cells cultured on POS in the absence of FAK inhibitor.

### **Rapid $\beta$ -catenin Translocation and Nuclear Activity are Reduced by FAK Inhibition.**

To evaluate how inhibiting FAK turnover affects  $\beta$ -catenin localization and activity over time we examined  $\beta$ -catenin localization in cells on POS and TCPS in the presence and absence of FAK inhibitor. We observed, in the absence of FAK inhibitor, a more rapid (24

hours) translocation of  $\beta$ -catenin from the membrane bound fraction to the nucleus in cells cultured on POS compared to cells cultured on TCPS. In cells cultured on POS in the absence of FAK inhibitor  $\beta$ -catenin concentration was significantly increased in the membrane fraction 48 hours after cell seeding while nuclear  $\beta$ -catenin concentration remained low (Figure 22a, b). 72 hours after seeding,  $\beta$ -catenin concentration within the membrane bound fraction decreased while  $\beta$ -catenin concentration in the nuclear fraction significantly increased before the concentration of  $\beta$ -catenin in both the membrane and nuclear fraction returned to basal levels at 96 hours. Cells cultured on TCPS in the absence of FAK inhibitor followed an identical trend of  $\beta$ -catenin translocation, although the process was delayed roughly 24 hours, beginning at 72 hours. We corroborated the observed  $\beta$ -catenin translocation using a luciferase-based reporter assay and observed a similar 24-hour delay in the nuclear translocation of  $\beta$ -catenin in cells cultured on TCPS in the absence of FAK inhibitor compared to cells cultured in the absence of FAK inhibitor on POS. In addition, nuclear activity was significantly greater at 24 hours, 48 hours, and 72 hours in cells cultured on POS in the absence of FAK inhibitor compared to cells cultured in the absence of FAK inhibitor on TCPS (Figure 22d). This is also indicative of the previously observed increases in osteoblastic differentiation, as nuclear activity of  $\beta$ -catenin is known to upregulated various osteogenic pathways such as the Wnt signaling pathway<sup>166</sup>.

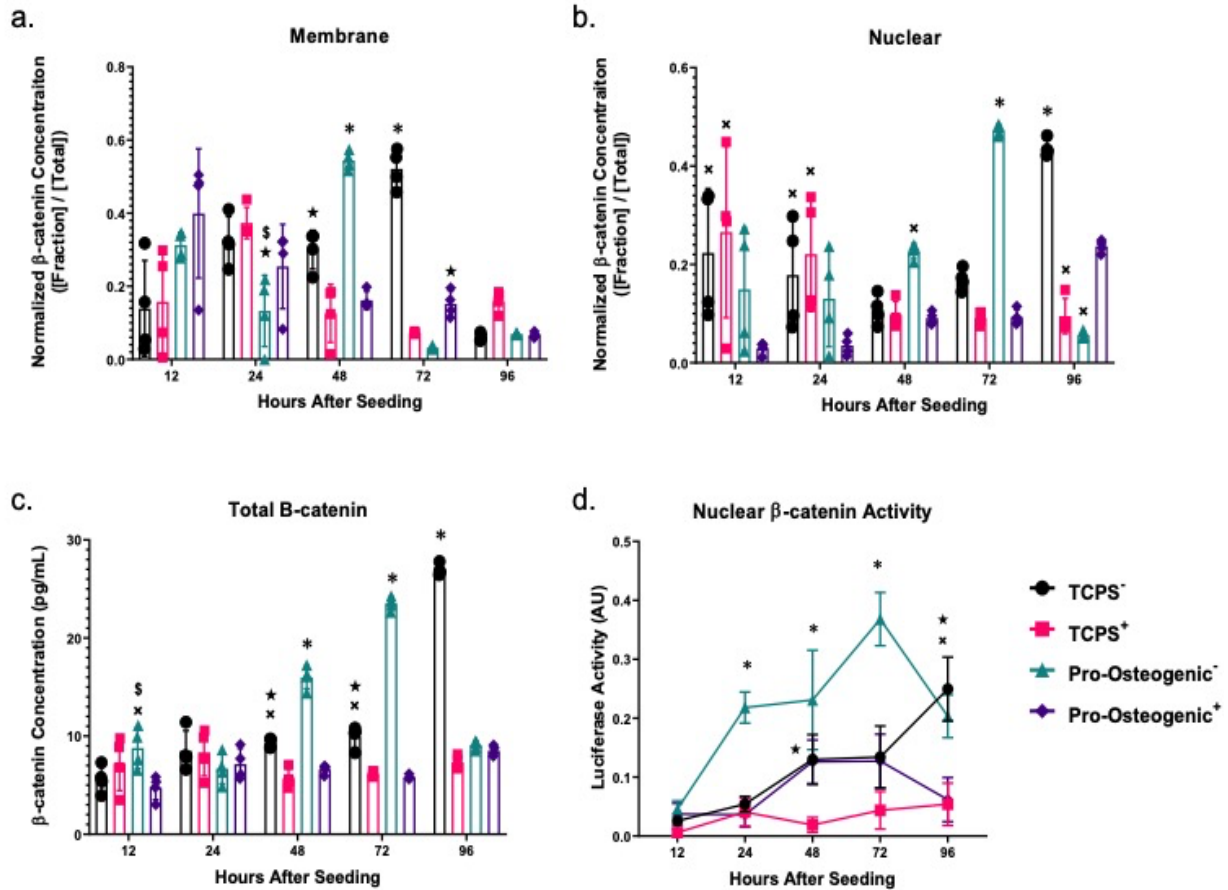


**Figure 22.**  $\beta$ -catenin localization, total  $\beta$ -catenin concentration, and  $\beta$ -catenin transcriptional activity over 96 hours in hFOB 1.19 cells cultured on either TCPS or Pro-Osteogenic substrate in the presence (+) or absence (-) of FAK inhibitor PF-573228. Quantification of normalized  $\beta$ -catenin concentration in either the (a) membrane bound cell fraction, (b) nuclear cell fraction, or (c) total  $\beta$ -catenin concentration. (d) Nuclear  $\beta$ -catenin activity quantified by TOPFLASH activity. Significance is considered  $p < 0.05$  only within the same timepoint. \* = significantly different than all other groups, \$ = significantly different than TCPS-, ★ = significantly different than TCPS+, x = significantly different than Pro-Osteogenic+. Membrane, Nuclear, and Total  $\beta$ -catenin,  $n=4$ . Nuclear activity,  $n= 3-4$  samples, with each sample being the average of 2 replicates.

Conversely, addition of FAK inhibitor to cells cultured on POS resulted in a significant reduction in  $\beta$ -catenin concentration and rate of translocation compared to cells cultured in the absence of FAK inhibitor. A 3-fold reduction  $\beta$ -catenin concentration in the membrane-bound fraction  $\beta$ -catenin (Figure 22a) and a roughly 1.5-fold reduction in  $\beta$ -catenin concentration within the nuclear fraction was observed at 48 hours in cell cultured

on POS in the presence of FAK inhibitor compared to cells cultured on POS without FAK inhibitor (Figure 22b). Interestingly, the addition of FAK inhibitor to cells cultured on TCPS did not significantly reduce the  $\beta$ -catenin concentration within the membrane-bound fraction at 48 hours, although it was decreased.  $\beta$ -catenin concentration in the nuclear fraction was unchanged at 48 hours in cells cultured on TCPS in absence of FAK inhibitor compared to cells cultured on TPCS or POS in the presence of FAK inhibitor. 72 hours after cell seeding,  $\beta$ -catenin concentration in the membrane-bound fraction was significantly increased in cells cultured on POS in the presence of FAK inhibitor compared to compared to cells cultured on POS in the absence of FAK inhibitor. In the nuclear fraction, the presence of FAK inhibitor significantly reduced (5-fold) the concentration of  $\beta$ -catenin compared to cells cultured on POS in the absence of FAK inhibitor.  $\beta$ -catenin concentration in the membrane-bound fraction of cells cultured on POS in the presence of FAK inhibitor was significantly reduced (5-fold) compared to cells cultured on TCPS in the absence of FAK inhibitor. In the nuclear fraction at 72 hours,  $\beta$ -catenin concentration was not significantly different in cells cultured on TCPS in the absence of FAK inhibitor compared to cells cultured on POS or TCPS in the presence of FAK inhibitor. At 96 hours no significant changes in  $\beta$ -catenin concentration were observed in the membrane bound-fraction between any of the groups. In the nuclear fraction, cells cultured on POS in the presence of FAK inhibitor had a significantly greater  $\beta$ -catenin concentration compared to cells cultured on POS in the absence of FAK inhibitor and cells cultured on TCPS in the presence of FAK inhibitor. In cells cultured on TCPS in the absence of FAK inhibitor we observed significantly 4-fold, 4.5-fold, and 1-fold increase in  $\beta$ -catenin concentration compared TCPS in the presence of FAK inhibitor, POS in the absence of FAK inhibitor, and POS in the presence of FAK inhibitor respectively. Interestingly, introduction of FAK inhibitor to cells cultured on POS resulted in a 24-hour delay more similar to that of cells cultured on TCPS in the absence of FAK inhibitor compared to cells cultured on POS in the absence of FAK inhibitor.

We again corroborated the observed  $\beta$ -catenin translocation with a luciferase-based reporter assay. We observed similar trends to those observed previously. Nuclear activity in cells cultured on POS in the absence of FAK inhibitor was significantly greater than all

other groups at 24 hours, 48 hours and 72 hours (Figure 22d). At 48 hours, nuclear activity was significantly greater in cells cultured on TCPS in the absence and cells cultured in POS in the absence of FAK inhibitor compared to cells cultured on TCPS in the absence of FAK inhibitor. At 96 hours, cells cultured on TCPS in the absence of FAK inhibitor possessed significantly greater nuclear activity compared to cells cultured on TCPS or POS in the absence of FAK inhibitor. However, this result was not corroborated by  $\beta$ -catenin concentration in the nuclear fraction, suggesting a difference between the localization of  $\beta$ -catenin and the nuclear activity.

Total  $\beta$ -catenin concentration varied significantly over time between the observed groups exhibiting the importance of normalizing all fractions to the total  $\beta$ -catenin concentration (Figure 22c). At 12 hours cells cultured on POS in the absence of FAK inhibitor expressed greater amounts of  $\beta$ -catenin compared to cells cultured on TCPS in the presence and absence of FAK inhibitor. No differences were observed at 24 hours between any of the groups. At 48 hours and 72 hours cells cultured on POS in the absence of FAK inhibitor expressed significantly greater total  $\beta$ -catenin concentration compared to all other groups. Total  $\beta$ -catenin concentration was also significantly greater in cells cultured on TCPS in the absence of FAK inhibitor compared to cells cultured on TCPS and POS in the presence of FAK inhibitor. At 96 hours, cells cultured on TCPS in the absence of FAK inhibitor expressed significantly greater total  $\beta$ -catenin concentration compared to all other groups.

## **DISCUSSION**

Determining a mechanism by which substrate surface characteristics are transduced by osteoblastic cells and their progenitors would provide avenues for the further optimization of bone implants and novel biomaterials for use in bone tissue engineering. Previous research by our group determined that cells cultured on POS exhibit greater osteoblastic differentiation, focal adhesion maturation, and focal adhesion turnover<sup>58</sup>. This turnover correlated with a more rapid translocation of  $\beta$ -catenin from the membrane bound fraction to the nuclear fraction<sup>58</sup>. Upon inhibition of  $\beta$ -catenin binding to TCF/LEF,

the observed increases in osteoblastic differentiation caused by the POS were abrogated<sup>58</sup>. This data led us to propose a focal adhesion initiated,  $\beta$ -catenin mediated mechanism by which substrate surface characteristics are transduced. The mechanism we proposed suggests that  $\beta$ -catenin, which is localized at the focal adhesion complex, is liberated upon focal adhesion turnover where it can then translocate and participate in the regulation of osteogenesis. While previous results suggest that  $\beta$ -catenin is liberated from focal adhesions and then participates in osteogenic regulation after nuclear translocation, we were unable to determine conclusively if the translocation was a result of focal adhesion turnover. Through the inhibition of FAK, we were able to determine the role focal adhesion turnover plays in the observed changes in  $\beta$ -catenin translocation, nuclear activity, and osteoblastic differentiation.

We hypothesized that inhibition of focal adhesion turnover in cells cultured on POS would result in a delay in the translocation of  $\beta$ -catenin from the membrane-bound protein fraction to the nucleus, a decrease in nuclear activity, and a decrease in the resulting increase in osteoblastic differentiation compared to cells cultured on POS without FAK inhibition.

We observed, as previously reported<sup>203</sup>, in cells cultured on POS in the absence of FAK inhibitor that a significant increase in osteoblastic differentiation occurred as measured by increases in the expression of key osteoblastic genes (Figure 18) and proteins (Figure 19) as well as increases in AP activity (Figure 17) compared to cells cultured on TCPS. In addition, cells cultured on POS in the absence of FAK inhibitor exhibited greater focal adhesion activity, as measured by an increase in FAK phosphorylation, which suggests an increase in focal adhesion turnover compared to cells cultured on TCPS in the absence of FAK inhibitor, which was observed in previous study by our group<sup>203</sup>. Moreover, a more rapid (24 hours) translocation of  $\beta$ -catenin from the membrane-bound protein fraction to the nucleus and greater nuclear activity was also observed (Figure 22). Study by Xie *et al.* observed that in adipose-derived stem cells cultured on POS of increasing substrate composed of polydimethylsiloxane, commitment to the osteogenic lineage was increased<sup>204</sup>.  $\beta$ -catenin nuclear translocation

was also upregulated on POS of increasing stiffness<sup>204</sup>. They also observed increased vinculin protein expression (~30%), suggesting greater focal adhesion formation in conjunction with the enhanced  $\beta$ -catenin nuclear translocation<sup>204</sup>. Study by Hamilton *et al.* also came to a similar conclusion. FAK activity and focal adhesion formation were both upregulated on a grooved pro-osteogenic substrate but were not observed on smooth non-pro-osteogenic substrates<sup>205</sup>. These studies suggest that focal adhesions and FAK are key mediators of substrate surface characteristics and help drive commitment to osteoblastic differentiation.

in the study presented here, addition of the FAK inhibitor to cells cultured on POS resulted in an observed decrease in the previous increases in osteoblastic differentiation caused by culture on the POS (Figure 17,18,19). AP activity of cells cultured on POS in the presence of FAK inhibitor at day 7 more closely resembled AP activity of cells cultured on TCPS in the absence of FAK inhibitor, suggesting that inhibition of FAK may inhibit transduction of the pro-osteogenic substrate. Again, Hamilton *et al.* observed a similar result. Upon inhibition of FAK phosphorylation, the previously observed increase in osteoblastic differentiation, as measured by RUNX2 nuclear translocation, on the grooved POS was inhibited<sup>205</sup>. In addition, Sun *et al.* and Rajshankar *et al.* both reported that in mice lacking FAK in osteoblast and pre-osteoblastic cells, a low bone mass phenotype and increased marrow adiposity was observed<sup>206,207</sup>. This was attributed to decreased osteoblastic proliferation, differentiation, and mesenchymal commitment to the osteoblastic lineage, thus reaffirming the results presented here that FAK, and therefore focal adhesion formation and turnover regulate osteoblastic differentiation<sup>206</sup>. It is worth noting, that in both cells cultured on POS or TCPS in the presence of FAK inhibitor, gene expression of *ALPL*, *RUNX2*, *SP7* were significantly down regulated, however *COL1A1* gene expression was not. *COL1A1* gene expression was the same if not slightly elevated in cells on both substrates when FAK inhibitor was introduced. This observed increase was not mirrored in protein expression after 7 days, with *COL1A1* protein significantly downregulated in cells cultured in the presence of FAK inhibitor compared to cells cultured in the absence of FAK inhibitor on POS. A previous study by Hori *et al.* reported similar protein



expression findings in fibroblasts<sup>58</sup>. They reported that increases in FAK (Tyr397) phosphorylation resulted in increases in collagen-I expression. Upon inhibition of FAK phosphorylation using PF-573228, the same inhibitor used in this study, collagen-I protein expression was significantly decreased<sup>58</sup>. We hypothesize that the increased *COL1A1* may be a direct result of the lack of *COL1A1* protein expression. Because the cell is unable to form a stable adhesion and because it cannot deposit collagen to form a stable extracellular matrix to adhere to, it upregulates gene expression *COL1A1* in an attempt to compensate for the dysregulation caused by the addition of FAK inhibitor. Rajshankar *et al.* also postulated a similar hypothesis, as dysregulation of FAK *in vivo* resulted in significant collagen deficiencies, as well as poor bone phenotype as a result of decreased osteoblastic differentiation and bone formation<sup>207</sup>.

$\beta$ -catenin translocation was also significantly affected by the addition of FAK inhibitor. The more rapid translocation (12 hours prior to TCPS) of  $\beta$ -catenin (Figure 22a,c), and the significant increase in nuclear transcriptional activity (Figure 22d) were no longer observed after the addition of FAK inhibitor. Instead, we observed that cells cultured on POS in the presence of FAK inhibitor appeared to also have the same 24-hour delay in  $\beta$ -catenin translocation from the membrane-bound protein fraction to the nuclear fraction that was observed in cells cultured on TCPS in the absence of FAK inhibitor.

Transcriptional activity of  $\beta$ -catenin in cells cultured on POS in the presence of FAK inhibitor mirrored the transcriptional activity of cells cultured on TCPS in the absence of FAK inhibitor almost identically. However, at 96 hours, we observed a decrease in transcriptional activity in cells cultured on POS in the presence of FAK inhibitor compared to the increase observed in cells cultured in the absence of FAK inhibitor in on TCPS or POS. Taken together, data presented here, and previously<sup>12,204–206</sup>, suggests that focal adhesion turnover plays a critical role in the observed increase in  $\beta$ -catenin translocation and transcriptional activity that results in the increased osteoblastic differentiation in response to the POS.

The study presented here and previously<sup>12</sup>, also seeks to answer the question posed by Jamora and Fuchs. The question is as follows, it is known that disassociation of

adhesion complexes occurs in response to various stimuli, but what happens to the proteins, such as  $\beta$ -catenin, that make up the adhesion complex after disassociation<sup>208</sup>? Do they participate in other facets of cell mechanotransduction or are they broken down and recycled<sup>208</sup>? We observed that inhibition of focal adhesion turnover prevented the previously observed increase in  $\beta$ -catenin translocation and upregulation of transcriptional activity it is reasonable to suggest that the changes are a direct result of focal adhesion turnover. This supports the conclusion that  $\beta$ -catenin does participate in other facets of cell mechanotransduction after focal adhesion turnover. A study by Kam and Quaranta has also provided evidence to suggest a similar conclusion<sup>208</sup>. By labeling  $\beta$ -catenin with a GFP+ fluorophore they concluded that in E-cadherins, a similar adhesion junction, disassembly allowed for the accumulation of GFP+  $\beta$ -catenin in the endocytic recycling compartment<sup>13,15,66,208</sup>. GFP+  $\beta$ -catenin then participated in nuclear translocation, increasing transcriptional activity as measured by TOPFLASH reporter<sup>15</sup>. Various other studies have also suggested a similar result, although these studies evaluated  $\beta$ -catenin translocation from cadherin complexes as well<sup>13,15,66</sup>. It has also been noted in previous studies that  $\beta$ -catenin is sequestered by both adhesions and the transcriptional pool, and therefore when decreases in adhesions occur, upregulation of  $\beta$ -catenin transcriptional activity can occur<sup>193,201,209</sup>. This has led to the suggestion that adhesions function as a reservoir for  $\beta$ -catenin, allowing rapid increases in intracellular  $\beta$ -catenin concentration in response to various stimuli<sup>210</sup>, a similar mechanism to what is proposed in this study.

While these data provide support for the proposed focal adhesion initiated,  $\beta$ -catenin mediate mechanism of substrate transduction further research is needed. FAK actively participates in numerous cellular pathways, making it difficult to determine if the observed changes are due strictly to  $\beta$ -catenin liberation from focal adhesion or due to changes in other proteins affected by FAK by these data alone<sup>192</sup>. For example, one downstream pathway directly affected by changes in FAK is the ak strain transforming/mammalian mechanistic target of rapamycin (AKT/mTORC) pathway. Upon phosphorylation, FAK stimulates the phosphorylation of AKT<sup>16,192</sup>. In addition, tension developed within the cytoskeleton during focal adhesion maturation can

increase mTORC2 activity which results in the phosphorylation of AKT and an upregulation in its activity<sup>192</sup>. Significantly, AKT is a potent inactivator of GSK-3 $\beta$ , which phosphorylates  $\beta$ -catenin in the cytoplasm and leads to its eventual degradation, providing a potential mechanism by which changes in FAK activity can regulate  $\beta$ -catenin activity<sup>210</sup>. Moreover, studies have determined that upon activation of mTORC2 through increased cell tension, significant increases in  $\beta$ -catenin concentration in the cytoplasm occurs<sup>211</sup>. However, mTORC2 is predominately located in the endoplasmic reticulum<sup>1,40,41,68</sup>, suggesting it may not be responsible for the rapid changes we observed in response to pro-osteogenic substrates but may instead work at a distance well after adhesions have formed. Additionally, in various cancers, such as ovarian, colon, and intestinal cancer, where focal adhesions play a critical role in tumor metastasis, it has been observed that FAK directly influences the  $\beta$ -catenin activity<sup>201,212,213</sup>. It does so through phosphorylation of GSK-3 $\beta$  by upregulating AKT phosphorylation and proline rich-tyrosine kinase 2 (PYK2) activity, which directly inhibit GSK-3 $\beta$ <sup>212,213</sup>. Taken together, it is clear further studies that evaluate  $\beta$ -catenin bound directly at the focal adhesion are necessary to determine that the observed changes are not due to other contributing factors.

The mechanism by which the transduction of substrate characteristics occurs is highly complex and it is challenging to segregate the numerous effects of proteins such as  $\beta$ -catenin and FAK which may participate in cell transduction. The study presented here evaluated the effect of focal adhesion turnover on  $\beta$ -catenin localization, transcriptional activity and osteoblastic differentiation to evaluate a proposed focal adhesion initiated,  $\beta$ -catenin mediated mechanism of substrate transduction. The evidence suggests that focal adhesion turnover and the observed changes in  $\beta$ -catenin translocation are related, however further study is needed to discern whether the  $\beta$ -catenin translocating is localized at focal adhesions specifically or a result of other cellular pathways.

## CONCLUSION

This study examined how inhibition of focal adhesion turnover affects  $\beta$ -catenin translocation,  $\beta$ -catenin transcriptional activity, and the resulting osteoblastic differentiation to evaluate the proposed focal adhesion initiated,  $\beta$ -catenin mediated mechanism of substrate surface transduction. To evaluate if the previously observed translocation and increase in transcriptional activity was a result of focal adhesion turnover, inhibiting focal adhesion turnover was required. We found that introduction of PF-573228, an inhibitor of FAK that reduces focal adhesion turnover *in vitro*, to cells cultured on pro-osteogenic substrate significantly reduced osteogenic differentiation induced by the pro-osteogenic substrate compared to cells cultured on pro-osteogenic substrate in the absence of FAK inhibitor. In addition, the more rapid translocation of  $\beta$ -catenin and increase in transcriptional activity observed in cells cultured in the absence of FAK inhibitor was abrogated when cells were cultured in the presence of FAK inhibitor, resulting in a translocation more similar to cells cultured on tissue culture polystyrene.

This evidence provides support for the hypothesis that the observed changes in  $\beta$ -catenin translocation, transcriptional activity, and the resulting osteoblastic differentiation are directly related to the more rapid turnover in focal adhesions caused by the pro-osteogenic substrate. Furthermore, the data presented here and previously by our group provides evidence for the support of our proposed mechanism of substrate surface transduction, in which focal adhesion turnover liberates  $\beta$ -catenin from the focal adhesion complex, allowing it to then translocate to the nucleus where it can participate in the transcriptional regulation of osteogenesis. However, more study is needed to determine if the  $\beta$ -catenin we observe translocating is specifically released from the focal adhesion complex itself or is a result of changes in other cell pathways such as the AKT/mTORC which can be regulated by FAK as well.

## **CHAPTER 7. Conclusions and Future Perspectives**

## **CONCLUSION**

The study presented here evaluated a novel aptamer-functionalized fibrin hydrogel and proposed and evaluated a focal adhesion initiated,  $\beta$ -catenin mediated, mechanism by which osteoblastic cells may transduce biomaterial substrate surfaces.

We demonstrated successfully that our novel hydrogel functionalized with a VEGF-specific aptamer significantly improved angiogenesis and osteogenesis in a critically sized cranial defect. The aptamer functionalized hydrogel release kinetics were significantly improved while maintaining the structural and mechanical properties of the native fibrin. The anti-VEGF DNA aptamer retained and released VEGF over the course of 15 days compared to 5 days in unfunctionalized fibrin hydrogels. The improved release kinetics resulted in a significant overall increase in angiogenesis, an increase in vessel density, and a decrease in separation of the blood vessels within the critically sized cranial defect. The aptamer functionalized hydrogel also elicited a significant, but limited improvement in osteogenesis. The limited healing of the bone tissue could be due to the time points examined during this study, but it could also be a consequence of poor interaction between the hydrogel and the cells themselves. Moreover, the hydrogel used in this study is only applicable to non-load bearing defects due to its mechanical incompetence. This is a significant limitation, as most bones within the body are load bearing and therefore necessitate a material or implant that can withstand the required mechanical loads. One way to overcome these limitations is to load the hydrogel with an osteoconductive material, such as hydroxyapatite.

To address these limitations, we first had to synthesize and characterize hydroxyapatite particles. Using a nanoemulsion methodology and by controlling pH of the source solutions, we successfully synthesized carbonated hydroxyapatite particles of varying sizes. The hydroxyapatite synthesized was biologically similar, with a crystallinity of roughly 70%, a size of 200nm to 900nm, and a chemical composition that mimicked biological apatite. In addition, we also observed that the synthesized hydroxyapatite was non-cytotoxic and that 500nm particles induced significantly greater osteoblastic

differentiation of hFOB1.19 preosteoblastic cells. After successful synthesis of hydroxyapatite particles, we then sought to understand how preosteoblastic cells are interacting with these particles and the biomaterial substrate. Unfortunately, the mechanisms by which bone cells transduce substrate surfaces are not fully understood. This gap in understanding led us to propose a mechanism by which bone cells, specifically osteoblasts, transduce substrate surface characteristics and how these surface characteristics induce osteogenesis.

The mechanism proposed in these studies is a focal adhesion initiated  $\beta$ -catenin mediated mechanism. To evaluate this mechanism, we developed a pro-osteogenic substrate composed of a PCL and the synthesized HAp at 30% wt/wt HAp/PCL. This substrate induced significantly greater osteoblastic differentiation in pre-osteoblastic cells compared to pre-osteoblastic cells grown on TCPS or other PCL/HAp substrates. In addition, this substrate induced significantly greater focal adhesion maturation, increased focal adhesion kinase phosphorylation, more rapid  $\beta$ -catenin translocation from the membrane to the nucleus, and significantly more  $\beta$ -catenin nuclear activity. Moreover, inhibition of  $\beta$ -catenin binding to TCF/LEF, upstream promoters of osteogenic genes, within the nucleus prevented the observed increase in osteoblastic differentiation and nuclear activity of  $\beta$ -catenin in cells grown on the pro-osteogenic substrate.

Further, to evaluate the role of focal adhesions in this mechanism we inhibited focal adhesion kinase, with an PF-573228, which is shown to also inhibit focal adhesion turnover *in vitro*. Inhibition of focal adhesion turnover caused a significant decrease in osteoblastic differentiation on the pro-osteogenic substrate. In addition,  $\beta$ -catenin translocation to the nucleus from the membrane and nuclear activity were both significantly downregulated. This suggests that focal adhesions play a critical role in the proposed mechanism of substrate surface transduction. Moreover, the data presented here provides evidence supporting the mechanism in which  $\beta$ -catenin is liberated from focal adhesions during turnover in response to pro-osteogenic substrates. After liberation  $\beta$ -catenin can actively translocate to the nucleus where, after binding to

TCF/LEF, it regulates osteogenic gene expression. This results in an overall increase in osteogenic commitment and differentiation in response to the pro-osteogenic substrate.

## **FUTURE PERSPECTIVES**

While the studies presented here provide evidence supporting the use of anti-VEGF aptamer functionalized hydrogel for critically sized cranial defects and a proposed focal adhesion initiated,  $\beta$ -catenin mediated mechanism of substrate surface transduction, many questions remain unanswered.

The aptamer functionalized hydrogel, while successful, did not induce complete bone healing of the defect. While this is likely due, in part, to the time points examined, the possibility that the hydrogel may not be ideal for bone growth cannot be ignored. VEGF is known to increase mesenchymal recruitment and has been shown to play a synergistic role with BMP4 in inducing bone formation<sup>1</sup>. The high specificity of the aptamers used in this study would allow for multiple factors to be delivered at once or allow for a more osteogenic factor to be used. Continued efforts are needed to examine the effect of coupling VEGF delivery with other growth factors such as BMPs, PTH, and PRP has on bone healing in critical sized cranial defects. Interestingly, regulation of the Semaphorin-3A (SEMA3A), which has been shown to regulate bone homeostasis, and VEGF are both regulated by Neuropilin-1 (NRP1), making it an attractive target for bone regeneration<sup>214</sup>. Specifically, NRP1 causes an upregulation of SEMA3A which has been observed to regulate bone homeostasis by inhibiting osteoclastic bone resorption and promoting osteoblastic bone formation through the Wnt/ $\beta$ -catenin signaling pathway. In addition, NRP1 upregulates VEGF receptor-2 (VEGFR2), promoting angiogenesis<sup>214</sup>. Continued study would allow evaluation of attractive proteins such as NRP1 or combinations of VEGF with other osteogenic agents to be evaluated.

Further, focal adhesions and FAK play a significant role in the transduction of substrate surface characteristics and in inducing osteoblastic differentiation. For this reason, it would also be conducive to evaluate the introduction of aptamers tailored towards



proteins like FAK to which promote increased turnover and maturation of focal adhesions. Previous studies have shown the importance of integrin binding in the promotion of focal adhesion turnover and maturation. These studies have also highlighted that integrin response is highly dependent on the extracellular matrix and the proteins that are coating it, such as laminins, fibrinogen, and collagens<sup>11,54,215</sup>. Based on these observations, novel aptamers for proteins such as fibrinogen, which promote integrin binding, would be attractive targets to increase the overall osteogenic nature of the AFH.

In addition, improving the mechanical properties of the hydrogel may also improve the osteogenic properties of the hydrogel overall. Numerous reviews summarize the ongoing research to develop combination biomaterials<sup>216</sup>. Attempts at integrating hydrogels and polymeric scaffolds have produced promising results. The polymers provide the mechanical stability and support required for bone applications while the hydrogels create a biomimetic environment that can be readily adapted to increase the overall osteoconductive properties of the material. Moreover, incorporation of osteoconductive materials themselves appears to be a promising avenue of study<sup>217</sup>.

As we have demonstrated in this study, carbonated hydroxyapatite particles can induce significantly greater osteoblastic differentiation *in vitro* when incorporated in PCL. Carles-Carner *et al.* reported similar observations<sup>67,218</sup>. They observed that incorporation of hydroxyapatite nanoparticles into polyethylene glycol (PEG) hydrogels, *in vitro*, upregulated osteoblastic differentiation roughly one-fold compared to non-hydroxyapatite loaded hydrogels<sup>67</sup>. Dhivya *et al.* also observed that incorporation of similar hydroxyapatite particles into a chitosan hydrogel, *in vivo*, yields a similar trend resulting in an overall increase in bone formation in a critically sized bone defect compared to non-hydroxyapatite loaded hydrogel groups<sup>66,219</sup>. Incorporation of hydroxyapatite particles into a hydrogel scaffold also provides mechanical support, allowing for hydrogels to be synthesized with improved compressive strength<sup>59,173,220</sup>. Taken together, this information suggests that incorporation of hydroxyapatite particles into a VEGF specific aptamer-functionalized hydrogel would significantly increase the overall osteogenic potential of the hydrogel itself. However, incorporation of osteoconductive particles may also cause

negative changes in hydrogel load efficiency, diffusion rate, and release kinetics and therefore warrants further study.

Optimization of the hydrogel or biomaterial surface characteristics to promote osteogenesis would also be one avenue to pursue further. This approach is made possible by understanding how bone cells and their progenitors transduce surface characteristics and provides novel targets to increase osteogenesis. The study presented here provided evidence for a focal adhesion initiated,  $\beta$ -catenin mediated mechanism of substrate surface transduction. However, more evidence to support our proposed mechanism is still need and significant questions still need to be answered. One of the most important questions is whether  $\beta$ -catenin is bound at the focal adhesion complex.  $\beta$ -catenin most likely binds with  $\alpha$ -catenin at focal adhesion complexes, similar to what has been observed at adherens junctions. This is further supported by a recent study which observed that BCL9-2, mammalian relative of the Wnt signaling component, Legless, is integral for the function of activated  $\beta$ -catenin in the transcription of Wnt target genes during fly and fish development<sup>221</sup>. They observed that when BCL9-2 was overexpressed, focal adhesion formation was significantly downregulated<sup>221</sup>. They also noted that BCL9-2 directly overlaps the known binding site of  $\beta$ -catenin and  $\alpha$ -catenin<sup>221</sup>. This suggests that inhibition of  $\alpha$ -catenin binding to  $\beta$ -catenin significantly affects focal adhesion formation and a competitive interaction between  $\alpha$ -catenin and BCL9-2 may play a role in  $\beta$ -catenin's ability to localize at the membrane or the nucleus. Unfortunately, co-immunoprecipitation of  $\beta$ -catenin with  $\alpha$ -catenin, paxillin, or vinculin would not provide the necessary evidence to determine if  $\beta$ -catenin is bound at focal adhesion complexes. Because these proteins are localized at both focal adhesions and adhesion junction's co-immunoprecipitation would not provide the necessary information to discriminate between  $\beta$ -catenin at a focal adhesion or an adhesion junction<sup>221</sup>. In addition, co-immunoprecipitation would also not provide evidence for whether the bound  $\beta$ -catenin is translocating to the nucleus. To overcome this, we propose using both live cell imaging and a fluorescence resonance energy transfer (FRET). Labeling of FAK with a donor fluorophore would allow activation of  $\beta$ -catenin with an acceptor fluorophore to be activated when the two proteins are localized within the same vicinity<sup>221</sup>. This would

provide evidence of  $\beta$ -catenin localization to the focal adhesion complex. In addition, by fluorescently labeling FAK and  $\beta$ -catenin with a photo-switchable fluorophore,  $\beta$ -catenin that co-localizes with FAK could be switched and the labeled  $\beta$ -catenin tracked to determine if it then translocated to the nucleus. This would provide conclusive evidence of the mechanism proposed in this study.

The completion of the proposed studies would provide further avenues of research, as it would provide a mechanism by which substrates are transduced by cells. Using this information as well as the information gained by evaluating how incorporation of osteoconductive materials and other biological factors into the AFH effects osteogenesis, more specific modifications could be made to the novel AFH further optimizing the osteogenic potential.

## **VITA**

Otto John Juhl IV was born on September 21, 1993, in Newark, Delaware, and is an American citizen. He graduated from The Charter School of Wilmington, Wilmington, Delaware in 2012. He received his Bachelor of Science in Biomedical Engineering from The University of Delaware, Newark, Delaware in 2016. He received a Doctor of Philosophy in Biomedical Engineering from Virginia Commonwealth University, Richmond, Virginia in 2021. He is a member of the Biomedical Engineering Society, the Orthopedic Research Society, The American Association for the Advancement of Science, The Academic Honor Society, and The Scientific Research Honor Society. During his degree, Otto also worked as a Licensing Liaison at the Innovation Gateway at Virginia Commonwealth University, working to patent, license, and commercialize technologies developed at Virginia Commonwealth University. Through his academic experience, Otto's research has focused on tissue engineering, biomaterials, and cell mechanobiology both in cardiac tissue and bone tissue.

## REFERENCES

1. Amini AR, Laurencin CT, Nukavarapu SP. Bone tissue engineering: recent advances and challenges. *Critical reviews in biomedical engineering*. 2012;40(5):363-408. Accessed May 16, 2018. <http://www.ncbi.nlm.nih.gov/pubmed/23339648>
2. Wang W, Yeung KWK. Bone grafts and biomaterials substitutes for bone defect repair: A review. *Bioactive Materials*. 2017;2(4):224-247. doi:10.1016/j.bioactmat.2017.05.007
3. Bohner M. Resorbable biomaterials as bone graft substitutes. *Materials Today*. 2010;13(1):24-30. doi:10.1016/S1369-7021(10)70014-6
4. Dalby MJ, di Silvio L, Harper EJ, Bonfield W. Increasing hydroxyapatite incorporation into poly(methylmethacrylate) cement increases osteoblast adhesion and response. *Biomaterials*. 2002;23(2):569-576. doi:10.1016/S0142-9612(01)00139-9
5. Khang D, Choi J, Im Y-M, et al. Role of subnano-, nano- and submicron-surface features on osteoblast differentiation of bone marrow mesenchymal stem cells. *Biomaterials*. 2012;33:5997-6007. doi:10.1016/j.biomaterials.2012.05.005
6. Lim JY, Siedlecki CA, Donahue HJ. Nanotopographic Cell Culture Substrate: Polymer-Demixed Nanotextured Films Under Cell Culture Conditions. *BioResearch*. 2012;1:252-255. doi:10.1089/biores.2012.0255
7. Loisel AE, Wei L, Faryad M, et al. Specific biomimetic hydroxyapatite nanotopographies enhance osteoblastic differentiation and bone graft osteointegration. *Tissue engineering Part A*. 2013;19(15-16):1704-1712. doi:10.1089/ten.TEA.2012.0560
8. Park JH, Olivares-Navarrete R, Baier RE, et al. Effect of cleaning and sterilization on titanium implant surface properties and cellular response. *Acta Biomaterialia*. 2012;8(5):1966-1975. doi:10.1016/j.actbio.2011.11.026
9. Yul Lim J, Donahue HJ. Cell Sensing and Response to Micro-and Nanostructured Surfaces Produced by Chemical and Topographic Patterning. doi:10.1089/ten.2006.0154
10. Barradas AMC, Yuan H, van Blitterswijk CA, Habibovic P. Osteoinductive biomaterials: current knowledge of properties, experimental models and biological mechanisms. *European cells & materials*. 2011;21:407-429; discussion 429. Accessed April 5, 2017. <http://www.ncbi.nlm.nih.gov/pubmed/21604242>
11. Alenghat FJ, Ingber DE. Mechanotransduction: all signals point to cytoskeleton, matrix, and integrins. *Science's STKE: signal transduction knowledge environment*. 2002;2002(119):pe6. doi:10.1126/stke.2002.119.pe6
12. Jamora C, Fuchs E. Intercellular adhesion, signalling and the cytoskeleton. *NATURE CELL BIOLOGY*. 2002;4(4):E101-E108. doi:10.1038/ncb0402-e101
13. Nelson WJ, Nusse R. Convergence of Wnt,  $\beta$ -Catenin, and Cadherin Pathways. *Science*. Accessed June 27, 2018. <http://science.sciencemag.org/content/sci/303/5663/1483.full.pdf>
14. Thompson BJ, Giancotti FG. Editorial overview: Cell signalling: Signal transduction to the nucleus, cytoskeleton, and organelles. *Current Opinion in Cell Biology*. 2018;51:iv-vii. doi:10.1016/j.ceb.2018.04.005

15. Mbalaviele G, Shin CS, Civitelli R. Perspective: Cell-Cell Adhesion and Signaling Through Cadherins: Connecting Bone Cells in Their Microenvironment. *Journal of Bone and Mineral Research*. 2006;21(12):1821-1827. doi:10.1359/jbmr.060811
16. Baron R, Kneissel M. WNT signaling in bone homeostasis and disease: from human mutations to treatments. *Nature Medicine*. 2013;19(2):179. doi:10.1038/nm.3074
17. Perez-Moreno M, Jamora C, Fuchs E. Sticky Business: Orchestrating Cellular Signals at Adherens Junctions. *Cell*. 2003;112:535-548. Accessed June 27, 2018. [https://ac.els-cdn.com/S0092867403001089/1-s2.0-S0092867403001089-main.pdf?\\_tid=4438d551-250c-404d-9f64-7128f8c36d03&acdnat=1530215526\\_233a1d91b2e23634dc9ad504e2e8471a](https://ac.els-cdn.com/S0092867403001089/1-s2.0-S0092867403001089-main.pdf?_tid=4438d551-250c-404d-9f64-7128f8c36d03&acdnat=1530215526_233a1d91b2e23634dc9ad504e2e8471a)
18. Zhou WY, Wang AM, Cheung AWL, Guo ABC, Jia ADM. Synthesis of carbonated hydroxyapatite nanospheres through nanoemulsion. Published online 2007. doi:10.1007/s10856-007-3156-9
19. Kalfas IH. Principles of bone healing. *Neurosurgical Focus*. 2001;10(4):1-4. doi:10.3171/foc.2001.10.4.2
20. Clarke B. Normal Bone Anatomy and Physiology. *Clinical Journal of the American Society of Nephrology*. 2008;3(Supplement 3):S131-S139. doi:10.2215/CJN.04151206
21. Parithimarkalaignan S, Padmanabhan T v. Osseointegration: An Update. doi:10.1007/s13191-013-0252-z
22. Sakai T, Nakano H, Okunishi- K. X-ray diffraction and infrared spectroscopy analyses on the crystallinity of engineered biological hydroxyapatite for medical application. Accessed October 9, 2017. <http://iopscience.iop.org/article/10.1088/1757-899X/79/1/012028/pdf>
23. LeGeros RZ, Trautz OR, Klein E, LeGeros JP. Two types of carbonate substitution in the apatite structure. *Experientia*. 1969;25(1):5-7. Accessed August 9, 2017. <http://www.ncbi.nlm.nih.gov/pubmed/5766584>
24. Mohamed AMFS. An overview of bone cells and their regulating factors of differentiation. *Malaysian Journal of Medical Sciences*. 2008;15(1):4-12.
25. Schaffler MB, Cheung W-Y, Majeska R, Kennedy O. Osteocytes: master orchestrators of bone. *Calcified tissue international*. 2014;94(1):5-24. doi:10.1007/s00223-013-9790-y
26. Apostu D, Lucaciu O, Berce C, Lucaciu D, Cosma D. Current methods of preventing aseptic loosening and improving osseointegration of titanium implants in cementless total hip arthroplasty: a review. *Journal of International Medical Research*. 2018;46(6):2104-2119. doi:10.1177/0300060517732697
27. T. A, C. J. Osteoinduction, osteoconduction and osseointegration. *European Spine Journal*. 2001;10(0):S96-S101. doi:10.1007/s005860100282
28. Liu Y, Rath B, Tingart M, Eschweiler J. Role of implants surface modification in osseointegration: A systematic review. *Journal of Biomedical Materials Research - Part A*. 2020;108(3):470-484. doi:10.1002/jbm.a.36829
29. Parihar A, Madhuri S, Devanna R, Sharma G, Singh R, Shetty K. Assessment of failure rate of dental implants in medically compromised patients. *Journal of Family Medicine and Primary Care*. 2020;9(2):883. doi:10.4103/jfmpc.jfmpc\_989\_19

30. Annunziata M, Guida L. The Effect of Titanium Surface Modifications on Dental Implant Osseointegration. *Biomaterials for Oral and Craniomaxillofacial Applications*. 2015;17:62-77. doi:10.1159/000381694
31. Wennerberg A, Albrektsson T. Effects of titanium surface topography on bone integration: A systematic review. *Clinical Oral Implants Research*. 2009;20(SUPPL. 4):172-184. doi:10.1111/j.1600-0501.2009.01775.x
32. Dulgar-Tulloch AJ, Bizios R, Siegel RW. Human mesenchymal stem cell adhesion and proliferation in response to ceramic chemistry and nanoscale topography. *Journal of Biomedical Materials Research Part A*. 2009;90A(2):586-594. doi:10.1002/jbm.a.32116
33. Roberts TT, Rosenbaum AJ. Bone grafts, bone substitutes and orthobiologics: the bridge between basic science and clinical advancements in fracture healing. *Organogenesis*. 2012;8(4):114-124. doi:10.4161/org.23306
34. Loh QL, Choong C. Three-dimensional scaffolds for tissue engineering applications: role of porosity and pore size. *Tissue engineering Part B, Reviews*. 2013;19(6):485-502. doi:10.1089/ten.TEB.2012.0437
35. Stancu IC, Lungu A, Iovu H. Hydrogels for bone regeneration. *Biomaterials for Bone Regeneration*. Published online January 1, 2014:62-86. doi:10.1533/9780857098104.1.62
36. El-Sherbiny IM, Yacoub MH. Hydrogel scaffolds for tissue engineering: Progress and challenges. *Global cardiology science & practice*. 2013;2013(3):316-342. doi:10.5339/gcsp.2013.38
37. Bai X, Gao M, Syed S, Zhuang J, Xu X, Zhang X-Q. Bioactive hydrogels for bone regeneration. *Bioactive Materials*. 2018;3(4):401. doi:10.1016/J.BIOACTMAT.2018.05.006
38. Hoare TR, Kohane DS. Hydrogels in drug delivery: Progress and challenges. *Polymer*. 2008;49(8):1993-2007. doi:10.1016/J.POLYMER.2008.01.027
39. Drury JL, Mooney DJ. Hydrogels for tissue engineering: scaffold design variables and applications. *Biomaterials*. 2003;24(24):4337-4351. doi:10.1016/S0142-9612(03)00340-5
40. Burg KJ, Porter S, Kellam JF. Biomaterial developments for bone tissue engineering. *Biomaterials*. 2000;21(23):2347-2359. Accessed April 5, 2017. <http://www.ncbi.nlm.nih.gov/pubmed/11055282>
41. Rose FRAJ, Oreffo ROC. Bone Tissue Engineering: Hope vs Hype. doi:10.1006/bbrc.2002.6519
42. Black CRM, Goriainov V, Gibbs D, Kanczler J, Tare RS, Oreffo ROC. Bone Tissue Engineering. Published online 2015. doi:10.1007/s40610-015-0022-2
43. Pavalko FM, Norvell SM, Burr DB, Turner CH, Duncan RL, Bidwell JP. A Model for mechanotransduction in bone cells: The load-bearing mechanosomes. *Journal of Cellular Biochemistry*. 2003;88(1):104-112. doi:10.1002/jcb.10284
44. Kashte S, Amit Kumar Jaiswal B, Sachin Kadam B. Artificial Bone via Bone Tissue Engineering: Current Scenario and Challenges. doi:10.1007/s13770-016-0001-6
45. Shafrir Y, Forgacs G. Mechanotransduction through the cytoskeleton. Accessed May 16, 2018. <https://www.physiology.org/doi/pdf/10.1152/ajpcell.00394.2001>
46. Pavalko FM, Chen NX, Turner CH, et al. Fluid shear-induced mechanical signaling in MC3T3-E1 osteoblasts requires cytoskeleton-integrin interactions. *American*

- Journal of Physiology-Cell Physiology*. 1998;275(6):C1591-C1601. doi:10.1152/ajpcell.1998.275.6.C1591
47. Parsons JT, Horwitz AR, Schwartz MA. Cell adhesion: integrating cytoskeletal dynamics and cellular tension. *Nature reviews Molecular cell biology*. 2010;11(9):633-643. doi:10.1038/nrm2957
  48. Chicurel ME, Chen CS, Ingber DE. Cellular control lies in the balance of forces. *Current Opinion in Cell Biology*. 1998;10(2):232-239. doi:10.1016/S0955-0674(98)80145-2
  49. Ingber D. Cellular tensegrity: defining new rules of biological design that govern the cytoskeleton. *Cell Science*. 1993;104:613-627.
  50. Uzer G, Fuchs RK, Rubin J, Thompson WR. Concise Review: Plasma and Nuclear Membranes Convey Mechanical Information to Regulate Mesenchymal Stem Cell Lineage. *STEM CELLS*. 2016;34(6):1455-1463. doi:10.1002/stem.2342
  51. Sit S-T, Manser E. Rho GTPases and their role in organizing the actin cytoskeleton. *Journal of Cell Science*. 2011;124:679-683. doi:10.1242/jcs.064964
  52. Perez F, Nelson C. Editorial overview: Cell architecture: Physical connections that drive organization and signaling. *Current Opinion in Cell Biology*. Accessed February 19, 2019. [https://ac.els-cdn.com/S095506741830053X/1-s2.0-S095506741830053X-main.pdf?\\_tid=f3fec3b9-88a3-4b5f-a6ea-0c74a3ebd686&acdnat=1550685803\\_2e9ba96175db6ead5d8d7e2f59f252a3](https://ac.els-cdn.com/S095506741830053X/1-s2.0-S095506741830053X-main.pdf?_tid=f3fec3b9-88a3-4b5f-a6ea-0c74a3ebd686&acdnat=1550685803_2e9ba96175db6ead5d8d7e2f59f252a3)
  53. Ohashi K, Fujiwara S, Mizuno K. Roles of the cytoskeleton, cell adhesion and rho signaling in mechanosensing and mechanotransduction. *Journal of Biochemistry*. Published online 2016. Accessed November 5, 2018. [https://watermark.silverchair.com/mvw082.pdf?token=AQECAHi208BE49Ooan9kKhW\\_Ercy7Dm3ZL\\_9Cf3qfKAc485ysgAAAEwggJNBgkqhkiG9w0BBwagggI-MIIC0gIBADCCAjMGCSqGS1b3DQEHATAeBglghkgBZQMEAS4wEQQM-tJdAifUXFEEeITXAgEQgIICBMyNKvLXRR3PX6y1usRsG7ztFEzZFa\\_\\_AFdJ8OBE2tYdjlxq](https://watermark.silverchair.com/mvw082.pdf?token=AQECAHi208BE49Ooan9kKhW_Ercy7Dm3ZL_9Cf3qfKAc485ysgAAAEwggJNBgkqhkiG9w0BBwagggI-MIIC0gIBADCCAjMGCSqGS1b3DQEHATAeBglghkgBZQMEAS4wEQQM-tJdAifUXFEEeITXAgEQgIICBMyNKvLXRR3PX6y1usRsG7ztFEzZFa__AFdJ8OBE2tYdjlxq)
  54. Siebers M, Burgge P, Walboomers X, Jansen J. Integrins as linker proteins between osteoblasts and bone replacing materials. A critical review. *Biomaterials*. 2005;26:137-146. Accessed November 9, 2018. [https://ac.els-cdn.com/S0142961204001607/1-s2.0-S0142961204001607-main.pdf?\\_tid=27de4364-1df0-466c-a07c-64cfc1633a46&acdnat=1541873343\\_25222e333b66e93ee3d61871aeb051c](https://ac.els-cdn.com/S0142961204001607/1-s2.0-S0142961204001607-main.pdf?_tid=27de4364-1df0-466c-a07c-64cfc1633a46&acdnat=1541873343_25222e333b66e93ee3d61871aeb051c)
  55. Hyzy SL, Kajan I, Wilson DS, et al. Inhibition of angiogenesis impairs bone healing in an in vivo murine rapid resynostosis model. *Journal of Biomedical Materials Research Part A*. 2017;105(10):2742-2749. doi:10.1002/jbm.a.36137
  56. Olivares-Navarrete R, Rodil SE, Hyzy SL, et al. Role of integrin subunits in mesenchymal stem cell differentiation and osteoblast maturation on graphitic carbon-coated microstructured surfaces. *Biomaterials*. 2015;51:69-79. doi:10.1016/j.biomaterials.2015.01.035
  57. Lim Y, Donahue H. Influence of Substratum Surface Chemistry/Energy and Topography on the Human Fetal Osteoblastic Cell Line hFOB 1.19: Phenotypic and Genotypic Responses Observed In Vitro. *Biomaterials*. Published online 2007. Accessed July 20, 2017. <https://www.ncbi.nlm.nih.gov/pmc/articles/PMC2705827/pdf/nihms30081.pdf>



58. Juhl OJ, Merife A-B, Zhang Y, Lemmon CA, Donahue HJ. Hydroxyapatite Particle Density Regulates Osteoblastic Differentiation Through  $\beta$ -Catenin Translocation. *Frontiers in Bioengineering and Biotechnology*. 2021;8:591084. doi:10.3389/fbioe.2020.591084
59. Critchley DR. Focal adhesions – the cytoskeletal connection. *Current Opinion in Cell Biology*. 2000;12(1):133-139. doi:10.1016/S0955-0674(99)00067-8
60. Peng X, Cuff LE, Lawton CD, DeMali KA. Vinculin regulates cell-surface E-cadherin expression by binding to  $\beta$ -catenin. *Journal of Cell Science*. 2010;123(4):567-577. doi:10.1242/jcs.056432
61. Bertocchi C, Ravasio A, Ong HT, Toyama Y, Kanchanawong P. Mechanical Roles of Vinculin/ $\beta$ -catenin interaction in Adherens Junction. *bioRxiv*. Published online January 1, 2019:770735. doi:10.1101/770735
62. Gaur T, Lengner CJ, Hovhannisyan H, et al. Canonical WNT Signaling Promotes Osteogenesis by Directly Stimulating Runx2 Gene Expression \*. Published online 2005. doi:10.1074/jbc.M500608200
63. Hill TP, Später D, Taketo MM, Birchmeier W, Hartmann C. Canonical Wnt/ $\beta$ -Catenin Signaling Prevents Osteoblasts from Differentiating into Chondrocytes. *Developmental Cell*. 2005;8(5):727-738. doi:10.1016/J.DEVCEL.2005.02.013
64. Rodda SJ, McMahon AP. Distinct roles for Hedgehog and canonical Wnt signaling in specification, differentiation and maintenance of osteoblast progenitors. *Development*. 2006;133(16):3231-3244. doi:10.1242/dev.02480
65. Glass DA, Karsenty G. Molecular Bases of the Regulation of Bone Remodeling by the Canonical Wnt Signaling Pathway. *Current Topics in Developmental Biology*. 2006;73:43-84. doi:10.1016/S0070-2153(05)73002-7
66. Bienz M.  $\beta$ -catenin: A pivot between cell adhesion and Wnt signalling. *Current Biology*. 2005;15(2). doi:10.1016/j.cub.2004.12.058
67. Brembeck FH, Schwarz-Romond T, Bakkers J, Wilhelm S, Hammerschmidt M, Birchmeier W. Essential role of BCL9-2 in the switch between  $\beta$ -catenin's adhesive and transcriptional functions. *Genes and Development*. 2004;18(18):2225-2230. doi:10.1101/gad.317604
68. Winkler T, Sass FA, Duda GN, Schmidt-Bleek K. A review of biomaterials in bone defect healing, remaining shortcomings and future opportunities for bone tissue engineering: The unsolved challenge. *Bone & joint research*. 2018;7(3):232-243. doi:10.1302/2046-3758.73.BJR-2017-0270.R1
69. Dimitriou R, Jones E, McGonagle D, Giannoudis P v. Bone regeneration: current concepts and future directions. *BMC Medicine*. 2011;9(1):66. doi:10.1186/1741-7015-9-66
70. Townsend CM, Beauchamp RD, Evers BM, Mattox KL. *Sabiston Textbook of Surgery: The Biological Basis of Modern Surgical Practice*.
71. Sterling JA, Guelcher SA. Biomaterial scaffolds for treating osteoporotic bone. *Current osteoporosis reports*. 2014;12(1):48-54. doi:10.1007/s11914-014-0187-2
72. Bisicchia S, Tudisco C. Radial Head and Neck Allograft for Comminute Irreparable Fracture-Dislocations of the Elbow. *Orthopedics*. 2016;39(6):e1205-e1208. doi:10.3928/01477447-20160901-01
73. Moghaddam A, Ermisch C, Schmidmaier G. Non-Union Current Treatment Concept. *Shafa Ortho J*. 2016;3(1):4546. doi:10.17795/soj-4546

74. O'Brien FJ. Biomaterials & scaffolds for tissue engineering. *Materials Today*. 2011;14(3):88-95. doi:10.1016/S1369-7021(11)70058-X
75. Orth M, Shenar AK, Scheuer C, et al. VEGF-loaded mineral-coated microparticles improve bone repair and are associated with increased expression of epo and RUNX-2 in murine non-unions. *Journal of Orthopaedic Research®*. 2019;37(4):821-831. doi:10.1002/JOR.24267
76. Otterbein LE, Fan Z, Koulmanda M, Thronley T, Strom TB. Innate immunity for better or worse govern the allograft response. *Current opinion in organ transplantation*. 2015;20(1):8-12. doi:10.1097/MOT.000000000000152
77. Lichte P, Pape HC, Pufe T, Kobbe P, Fischer H. Scaffolds for bone healing: Concepts, materials and evidence. *Injury*. 2011;42(6):569-573. doi:10.1016/J.INJURY.2011.03.033
78. García JR, García AJ. Biomaterial-mediated strategies targeting vascularization for bone repair. *Drug delivery and translational research*. 2016;6(2):77-95. doi:10.1007/s13346-015-0236-0
79. Hankenson KD, Dishowitz M, Gray C, Schenker M. Angiogenesis in bone regeneration. *Injury*. 2011;42(6):556-561. doi:10.1016/j.injury.2011.03.035
80. Chen N, Zhang Z, Soontornworajit B, Zhou J, Wang Y. Cell adhesion on an artificial extracellular matrix using aptamer-functionalized PEG hydrogels. *Biomaterials*. 2012;33(5):1353-1362. doi:10.1016/J.BIOMATERIALS.2011.10.062
81. Maisani M, Pezzoli D, Chassande O, Mantovani D. Cellularizing hydrogel-based scaffolds to repair bone tissue: How to create a physiologically relevant micro-environment? *Journal of Tissue Engineering*. 2017;8:204173141771207. doi:10.1177/2041731417712073
82. Janmey PA, Winer JP, Weisel JW. Fibrin gels and their clinical and bioengineering applications. *Journal of the Royal Society, Interface*. 2009;6(30):1-10. doi:10.1098/rsif.2008.0327
83. Zhao N, Coyne J, Xu M, et al. Assembly of Bifunctional Aptamer–Fibrinogen Macromer for VEGF Delivery and Skin Wound Healing. Published online 2019. doi:10.1021/acs.chemmater.8b04486
84. Linnes MP, Ratner BD, Giachelli CM. A fibrinogen-based precision microporous scaffold for tissue engineering. *Biomaterials*. 2007;28(35):5298-5306. doi:10.1016/J.BIOMATERIALS.2007.08.020
85. Li Y, Meng H, Liu Y, Lee BP. Fibrin Gel as an Injectable Biodegradable Scaffold and Cell Carrier for Tissue Engineering. *The Scientific World Journal*. 2015;2015:1-10. doi:10.1155/2015/685690
86. Battig MR, Huang Y, Chen N, Wang Y. Aptamer-functionalized superporous hydrogels for sequestration and release of growth factors regulated via molecular recognition. *Biomaterials*. 2014;35(27):8040-8048. doi:10.1016/J.BIOMATERIALS.2014.06.001
87. Street J, Bao M, deGuzman L, et al. Vascular endothelial growth factor stimulates bone repair by promoting angiogenesis and bone turnover. *Proceedings of the National Academy of Sciences of the United States of America*. 2002;99(15):9656. doi:10.1073/PNAS.152324099
88. Young S, Patel ZS, Kretlow JD, et al. Dose Effect of Dual Delivery of Vascular Endothelial Growth Factor and Bone Morphogenetic Protein-2 on Bone

- Regeneration in a Rat Critical-Size Defect Model. *Tissue Engineering Part A*. 2009;15(9):2347-2362. doi:10.1089/ten.tea.2008.0510
89. Ritger PL, Peppas NA. A simple equation for description of solute release II. Fickian and anomalous release from swellable devices. *Journal of Controlled Release*. 1987;5(1):37-42. doi:10.1016/0168-3659(87)90035-6
90. Gordeladze JO, Haugen HJ, Lyngstadaas SP, Reseland JE. Bone Tissue Engineering: State of the Art, Challenges, and Prospects. In: *Tissue Engineering for Artificial Organs*. Wiley-VCH Verlag GmbH & Co. KGaA; 2017:525-551. doi:10.1002/9783527689934.ch16
91. Caliani SR, Burdick JA. A practical guide to hydrogels for cell culture. *Nature methods*. 2016;13(5):405-414. doi:10.1038/nmeth.3839
92. Claes L, Eckert-Hübner K, Augat P. The effect of mechanical stability on local vascularization and tissue differentiation in callus healing. *Journal of Orthopaedic Research*. 2002;20(5):1099-1105. doi:10.1016/S0736-0266(02)00044-X
93. Maes C, Carmeliet G. Vascular and Nonvascular Roles of VEGF in Bone Development. Published online 2013. Accessed April 22, 2019. <https://www.ncbi.nlm.nih.gov/books/NBK6134/>
94. Ogilvie CM, Lu C, Marcucio R, et al. Vascular endothelial growth factor improves bone repair in a murine nonunion model. *The Iowa orthopaedic journal*. 2012;32:90-94. Accessed April 22, 2019. <http://www.ncbi.nlm.nih.gov/pubmed/23576927>
95. Hu K, Olsen BR. The roles of vascular endothelial growth factor in bone repair and regeneration. *Bone*. 2016;91:30-38. doi:10.1016/j.bone.2016.06.013
96. Klein M, Stieger A, Stenger D, et al. Comparison of healing process in open osteotomy model and open fracture model: Delayed healing of osteotomies after intramedullary screw fixation. *Journal of Orthopaedic Research*. 2015;33(7):971-978. doi:10.1002/jor.22861
97. Peng H, Wright V, Usas A, et al. Synergistic enhancement of bone formation and healing by stem cell-expressed VEGF and bone morphogenetic protein-4. *The Journal of clinical investigation*. 2002;110(6):751-759. doi:10.1172/JCI15153
98. Novosel EC, Kleinhans C, Kluger PJ. Vascularization is the key challenge in tissue engineering. *Advanced Drug Delivery Reviews*. 2011;63(4-5):300-311. doi:10.1016/J.ADDR.2011.03.004
99. Tomlinson RE, Silva MJ. Skeletal Blood Flow in Bone Repair and Maintenance. *Bone research*. 2013;1(4):311-322. doi:10.4248/BR201304002
100. Wang H-K, Wang Y-X, Xue C-B, et al. Angiogenesis in tissue-engineered nerves evaluated objectively using MICROFIL perfusion and micro-CT scanning. *Neural regeneration research*. 2016;11(1):168-173. doi:10.4103/1673-5374.175065
101. Lim J, Loisel AE, Lee JS, Zhang Y, Salvi JD, Donahue HJ. Optimizing the Osteogenic Potential of Adult Stem Cells for Skeletal Regeneration. *Journal of Orthopaedic Research*. Published online 2011:1627-1633. doi:10.1002/jor.21441
102. Lybrand K, Bragdon B, Gerstenfeld L. Mouse models of bone healing: fracture, marrow ablation, and distraction osteogenesis. *Current protocols in mouse biology*. 2015;5(1):35-49. doi:10.1002/9780470942390.mo140161
103. Hsiong SX, Mooney DJ. Regeneration of vascularized bone. *Periodontology 2000*. 2006;41(1):109-122. doi:10.1111/j.1600-0757.2006.00158.x

104. de Witte T-M, Fratila-Apachitei LE, Zadpoor AA, Peppas NA. Bone tissue engineering via growth factor delivery: from scaffolds to complex matrices. *Regenerative Biomaterials*. 2018;5(4):197-211. doi:10.1093/rb/rby013
105. Devescovi V, Leonardi E, Ciapetti G, Cenni E. Growth factors in bone repair. *La Chirurgia degli Organi di Movimento*. 2008;92(3):161-168. doi:10.1007/s12306-008-0064-1
106. Zhou H, Lee J. Nanoscale hydroxyapatite particles for bone tissue engineering. *Acta Biomaterialia*. 2011;7(7):2769-2781. doi:10.1016/j.actbio.2011.03.019
107. Roveri N, Iafisco M. Evolving application of biomimetic nanostructured hydroxyapatite. *Nanotechnology, science and applications*. 2010;3:107-125. doi:10.2147/NSA.S9038
108. Size effect of hydroxyapatite nanoparticles on proliferation and apoptosis of osteoblast-like cells. *Acta Biomaterialia*. 2009;5(1):338-345. doi:10.1016/J.ACTBIO.2008.07.023
109. Liu Y, Wang G, Cai Y, et al. In vitro effects of nanophase hydroxyapatite particles on proliferation and osteogenic differentiation of bone marrow-derived mesenchymal stem cells. *Journal of Biomedical Materials Research Part A*. 2009;90A(4):1083-1091. doi:10.1002/jbm.a.32192
110. Roohani-Esfahani S-I, Nouri-Khorasani S, Lu Z, Appleyard R, Zreiqat H. The influence of hydroxyapatite nanoparticle shape and size on the properties of biphasic calcium phosphate scaffolds coated with hydroxyapatite PCL composites. *Biomaterials*. 2010;31:5498-5509. doi:10.1016/j.biomaterials.2010.03.058
111. Kalia P, Vizcay-Barrena G, Fan JP, Warley A, di Silvio L, Huang J. Nanohydroxyapatite shape and its potential role in bone formation: an analytical study. *Journal of the Royal Society, Interface*. 2014;11(93):20140004. doi:10.1098/rsif.2014.0004
112. Xu Z, Liu C, Wei J, Sun J. Effects of four types of hydroxyapatite nanoparticles with different nanocrystal morphologies and sizes on apoptosis in rat osteoblasts. *Journal of Applied Toxicology*. 2012;32(6):429-435. doi:10.1002/jat.1745
113. Lebre F, Sridharan R, Sawkins MJ, Kelly DJ, O'Brien FJ, Lavelle EC. The shape and size of hydroxyapatite particles dictate inflammatory responses following implantation. doi:10.1038/s41598-017-03086-0
114. Wang J, Yang G, Wang Y, et al. Chimeric protein template-induced shape control of bone mineral nanoparticles and its impact on mesenchymal stem cell fate. *Biomacromolecules*. 2015;16(7):1987-1996. doi:10.1021/acs.biomac.5b00419
115. Zhao X, Ng S, Boon , et al. Cytotoxicity of hydroxyapatite nanoparticles is shape and cell dependent. *Arch Toxicol*. 2013;87:1037-1052. doi:10.1007/s00204-012-0827-1
116. Lim J, Hansen JC, Siedlecki CA, Runt J, Donahue HJ. Human fetal osteoblastic cell response to polymer-demixed nanotopographic interfaces. *Journal of Royal Society Interface*. 2005;2(2):97-108. doi:10.1098/rsif.2004.0019
117. Faghihi F, Eslaminejad MB. The effect of nano-scale topography on osteogenic differentiation of mesenchymal stem cells. *Biomed Pap Med Fac Univ Palacky Olomouc Czech Repub*. 2014;158(1):5-16. doi:10.5507/bp.2013.013

118. Abagnale G, Steger M, Hoa Nguyen V, et al. Surface topography enhances differentiation of mesenchymal stem cells towards osteogenic and adipogenic lineages. *Biomaterials*. 2015;61:316-326. doi:10.1016/j.biomaterials.2015.05.030
119. Chuenjitkuntaworn B, Inrung W, Damrongsri D, Mekaapiruk K, Supaphol P, Pavasant P. Polycaprolactone/hydroxyapatite composite scaffolds: Preparation, characterization, and in vitro and in vivo biological responses of human primary bone cells. *Journal of Biomedical Materials Research Part A*. 2010;94A(1):241-251. doi:10.1002/jbm.a.32657
120. Domingos M, Gloria A, Coelho J, Bartolo P, Ciurana J. Three-dimensional printed bone scaffolds: The role of nano/micro-hydroxyapatite particles on the adhesion and differentiation of human mesenchymal stem cells. *Proceedings of the Institution of Mechanical Engineers, Part H: Journal of Engineering in Medicine*. Published online January 5, 2017:095441191668023. doi:10.1177/0954411916680236
121. Tautzenberger A, Kovtun A, Ignatius A. Nanoparticles and their potential application in bone. *International Journal of Nanomedicine*. 2012;7:4545-4557. doi:10.2147/IJN.S34127
122. Yang X, Li Y, Liu X, Zhang R, Feng Q. In Vitro Uptake of Hydroxyapatite Nanoparticles and Their Effect on Osteogenic Differentiation of Human Mesenchymal Stem Cells. *Stem Cells International*. 2018;2018. doi:10.1155/2018/2036176
123. Cai Y, Liu Y, Yan W, et al. Role of hydroxyapatite nanoparticle size in bone cell proliferation. *Journal of Materials Chemistry*. 2007;17(36):3780. doi:10.1039/b705129h
124. Wen Kuo C, Chueh D-Y, Chen P. Investigation of size-dependent cell adhesion on nanostructured interfaces. *Journal of Nanobiotechnology*. Published online 2014:1-10. doi:10.1186/s12951-014-0054-4
125. Nayak AK. Hydroxyapatite Synthesis Methodologies: An Overview. *International Journal of ChemTech Research*. 2(2):974-4290. Accessed August 2, 2017. <https://pdfs.semanticscholar.org/33ab/8d2c2b7dc9ee73c099c9a84ff9483146ab88.pdf>
126. Wang P, Li C, Gong H, Jiang X, Wang H, Li K. Effects of synthesis conditions on the morphology of hydroxyapatite nanoparticles produced by wet chemical process. *Powder Technology*. 2010;203(2):315-321. doi:10.1016/j.powtec.2010.05.023
127. Ferraz M, Monteiro F, Manuel C. Hydroxyapatite nanoparticles: A review of preparation methodologies. *Journal of Applied Biomaterials and Biomechanics*. Published online 2004. Accessed August 2, 2017. [https://www.researchgate.net/profile/Fernando\\_Monteiro2/publication/46037735\\_Hydroxyapatite\\_nanoparticles\\_A\\_review\\_of\\_preparation\\_methodologies/links/0fcfd507746dc59025000000.pdf](https://www.researchgate.net/profile/Fernando_Monteiro2/publication/46037735_Hydroxyapatite_nanoparticles_A_review_of_preparation_methodologies/links/0fcfd507746dc59025000000.pdf)
128. Lim GK, Wang J, Ng SC, Chew CH, Gan LM. Processing of hydroxyapatite via microemulsion and emulsion routes. *Biomaterials*. 1997;18(21):1433-1439. doi:10.1016/S0142-9612(97)00081-1
129. Motskin M, Wright DM, Muller K, et al. Hydroxyapatite nano and microparticles: Correlation of particle properties with cytotoxicity and biostability. *Biomaterials*. 2009;30:3307-3317. doi:10.1016/j.biomaterials.2009.02.044

130. Nelson DG, Featherstone JD. Preparation, analysis, and characterization of carbonated apatites. *Calcified tissue international*. 1982;34 Suppl 2:S69-81. Accessed August 2, 2017. <http://www.ncbi.nlm.nih.gov/pubmed/6293677>
131. Barralet J, Best S, Bonfield W. Carbonate substitution in precipitated hydroxyapatite: an investigation into the effects of reaction temperature and bicarbonate ion concentration. *Journal of biomedical materials research*. 1998;41(1):79-86. Accessed August 2, 2017. <http://www.ncbi.nlm.nih.gov/pubmed/9641627>
132. Barralet J, Knowles JC, Best S, Bonfield W. Thermal decomposition of synthesised carbonate hydroxyapatite. *Journal of materials science Materials in medicine*. 2002;13(6):529-533. Accessed August 2, 2017. <http://www.ncbi.nlm.nih.gov/pubmed/15348582>
133. Abidi SSA, Murtaza Q. Synthesis and Characterization of Nano-hydroxyapatite Powder Using Wet Chemical Precipitation Reaction. *Journal of Materials Science & Technology*. 2014;30(4):307-310. doi:10.1016/j.jmst.2013.10.011
134. Martinez-Castanon G, Hernandez-Martinez S, Nino-Martinez N, Ruiz F. Preparation and characterization of nanostructured powders of hydroxyapatite. *Surfaces and Vacuum* . 2012;25(2):101-105.
135. Salimi MN, Bridson RH, Grover LM, Leeke GA. Effect of processing conditions on the formation of hydroxyapatite nanoparticles. *Powder Technology*. 2012;218:109-118. doi:10.1016/j.powtec.2011.11.049
136. Elhendawi H, Felfel RM, Abd El-Hady BM, Reicha FM. Effect of Synthesis Temperature on the Crystallization and Growth of In Situ Prepared Nanohydroxyapatite in Chitosan Matrix. Published online 2014. doi:10.1155/2014/897468
137. Milev AS, Kannangara GSK, Ben-Nissan B, Wilson MA. Temperature effects on a hydroxyapatite precursor solution. *Journal of Physical Chemistry B*. 2004;108(18):5516-5521. doi:10.1021/jp035548h
138. Kumar R, Prakash KH, Cheang P, Khor KA. Temperature driven morphological changes of chemically precipitated hydroxyapatite nanoparticles. *Langmuir*. 2004;20(13):5196-5200. doi:10.1021/la049304f
139. Furuzono T, Walsh D, Sato K, Sonoda K, Tanaka J. *Effect of Reaction Temperature on the Morphology and Size of Hydroxyapatite Nanoparticles in an Emulsion System*.
140. Klug H, Alexander L. *Introduction to X-Ray Powder Diffractometry*. John Wiley & Sons; 2001. Accessed April 21, 2020. <http://chem.unt.edu/~tgolden/courses/Lecture1 XRD 2018.pdf>
141. Holzwarth U, Gibson N. The Scherrer equation versus the “Debye-Scherrer equation.” *Nature Nanotechnology*. 2011;6(9):534. doi:10.1038/nnano.2011.145
142. Latifi SM, Fathi MH, Golozar MA. Preparation and characterisation of bioactive hydroxyapatite–silica composite nanopowders via sol–gel method for medical applications. *Advances in Applied Ceramics*. 2011;110(1):8-14. doi:10.1179/174367510X12753884125325
143. Murugan R, Ramakrishna S. Bioresorbable composite bone paste using polysaccharide based nano hydroxyapatite. *Biomaterials*. 2004;25(17):3829-3835. doi:10.1016/J.BIOMATERIALS.2003.10.016

144. Schindelin J, Arganda-Carreras I, Frise E, et al. Fiji: An open-source platform for biological-image analysis. *Nature Methods*. 2012;9(7):676-682. doi:10.1038/nmeth.2019
145. Donahue HJ, Li Z, Zhou Z, Yellowley CE. Differentiation of human fetal osteoblastic cells and gap junctional intercellular communication. *American Journal of Physiology-Cell Physiology*. 2000;278(278):C315-C322. doi:10.1152/ajpcell.2000.278.2.C315
146. Ma T, Xia Z, Liao L. Effect of reaction systems and surfactant additives on the morphology evolution of hydroxyapatite nanorods obtained via a hydrothermal route. *Applied Surface Science*. 2011;257(9):4384-4388. doi:10.1016/J.APSUSC.2010.12.067
147. Kong L, Gao Y, Lu G, Gong Y, Zhao N, Zhang X. A study on the bioactivity of chitosan/nano-hydroxyapatite composite scaffolds for bone tissue engineering. *European Polymer Journal*. 2006;42(12):3171-3179. doi:10.1016/J.EURPOLYMJ.2006.08.009
148. Seckler MM, Danese M, Derenzo S, Valarelli J v, Giuliatti M, Rodríguez-Clemente R. Influence of Process Conditions on Hydroxyapatite Crystallinity Obtained by Direct Crystallization. Accessed August 9, 2017. <http://www.scielo.br/pdf/mr/v2n2/0009.pdf>
149. Chen W, Shao Y, Li X, Zhao G, Fu J. Nanotopographical surfaces for stem cell fate control: Engineering mechanobiology from the bottom. *Nano Today*. 2014;9(6):759-784. doi:10.1016/j.nantod.2014.12.002
150. Lee JH, Rim NG, Jung HS, Shin H. Control of Osteogenic Differentiation and Mineralization of Human Mesenchymal Stem Cells on Composite Nanofibers Containing Poly[lactic- co -(glycolic acid)] and Hydroxyapatite. *Macromolecular Bioscience*. 2010;10(2):173-182. doi:10.1002/mabi.200900169
151. Lü LX, Zhang XF, Wang YY, et al. Effects of hydroxyapatite-containing composite nanofibers on osteogenesis of mesenchymal stem cells in vitro and bone regeneration in vivo. *ACS Applied Materials and Interfaces*. 2013;5(2):319-330. doi:10.1021/am302146w
152. Ahn EH, Kim Y, Kshitiz, et al. Spatial control of adult stem cell fate using nanotopographic cues. *Biomaterials*. 2014;35(8):2401-2410. doi:10.1016/j.biomaterials.2013.11.037
153. Galow AM, Rebl A, Koczan D, Bonk SM, Baumann W, Gimsa J. Increased osteoblast viability at alkaline pH in vitro provides a new perspective on bone regeneration. *Biochemistry and Biophysics Reports*. 2017;10:17-25. doi:10.1016/j.bbrep.2017.02.001
154. Asami A, Nakamura M, Takeuchi M, et al. Effects of Heat Treatment of Hydroxyapatite on Osteoblast Differentiation. *Journal of Hard Tissue Biology*. 2008;17(2):37-46. doi:10.2485/jhtb.17.37
155. Liu H, Slamovich EB, Webster- TJ, et al. Mimicking the nanofeatures of bone increases bone-forming cell adhesion and proliferation Increased osteoblast functions on nanophase titania dispersed in PLGA composites Adhesion of *Pseudomonas fluorescens* onto nanophase materials Mimicking the nanofeatu. Published online 2005. doi:10.1088/0957-4484/16/9/069

156. Yim EKF, Darling EM, Kulangara K, Guilak F, Leong KW. Nanotopography-induced changes in focal adhesions, cytoskeletal organization, and mechanical properties of human mesenchymal stem cells. *Biomaterials*. 2010;31(6):1299-1306. doi:10.1016/j.biomaterials.2009.10.037
157. Lim JY, Hansen JC, Siedlecki CA, et al. Osteoblast Adhesion on Poly(L-lactic Acid)/Polystyrene Demixed Thin Film Blends: Effect of Nanotopography, Surface Chemistry, and Wettability. *Biomacromolecules*. 2005;6(6):3319-3327. doi:10.1021/bm0503423
158. Lossdörfer S, Schwartz Z, Wang L, et al. Microrough implant surface topographies increase osteogenesis by reducing osteoclast formation and activity. *Journal of Biomedical Materials Research Part A*. 2004;70A(3):361-369. doi:10.1002/jbm.a.30025
159. Deligianni DD, Katsala ND, Koutsoukos PG, Missirlis YF. Effect of surface roughness of hydroxyapatite on human bone marrow cell adhesion, proliferation, differentiation and detachment strength. *Biomaterials*. 2000;22(1):87-96. doi:10.1016/S0142-9612(00)00174-5
160. Mendonça G, Mendonça DBS, Simões LGP, et al. The effects of implant surface nanoscale features on osteoblast-specific gene expression. *Biomaterials*. 2009;30(25):4053-4062. doi:10.1016/J.BIOMATERIALS.2009.04.010
161. Legeros RZ, Trautz OR, Legeros JP, Klein E, Shirra WP. Apatite Crystallites: Effects of Carbonate on Morphology. *Science*. 1967;155(3768). Accessed August 9, 2017. <http://science.sciencemag.org/content/155/3768/1409.long>
162. Thomas V, Jagani S, Johnson K, et al. Electrospun bioactive nanocomposite scaffolds of polycaprolactone and nanohydroxyapatite for bone tissue engineering. *Journal of Nanoscience and Nanotechnology*. 2006;6(2):487-493. doi:10.1166/jnn.2006.097
163. Wu F, Lin DDW, Chang JH, Fischbach C, Estroff LA, Gourdon D. Effect of the materials properties of hydroxyapatite nanoparticles on fibronectin deposition and conformation. *Crystal Growth and Design*. 2015;15(5):2452-2460. doi:10.1021/acs.cgd.5b00231
164. Bovand D, Allazadeh MR, Rasouli S, Khodadad E, Borhani E. Studying the effect of hydroxyapatite particles in osteoconductivity of Ti-HA bioceramic. *Journal of the Australian Ceramic Society*. 2019;55(2):395-403. doi:10.1007/s41779-018-0247-7
165. Schaffler MB, Kennedy OD. Osteocyte Signaling in Bone. doi:10.1007/s11914-012-0105-4
166. Cadigan KM, Waterman ML. TCF/LEFs and Wnt signaling in the nucleus. *Cold Spring Harbor perspectives in biology*. 2012;4(11). doi:10.1101/cshperspect.a007906
167. Thompson WR, Rubin CT, Rubin J. Mechanical regulation of signaling pathways in bone. *Gene*. 2012;503(2):179-193. doi:10.1016/J.GENE.2012.04.076
168. Kanchanawong P, Shtengel G, Pasapera AM, et al. Nanoscale architecture of integrin-based cell adhesions. *Nature*. 2010;468(7323):580-584. doi:10.1038/nature09621
169. Zamir E, Geiger B. Molecular complexity and dynamics of cell-matrix adhesions. *Journal of Cell Science* . 2001;14(114):3583-3590.



170. Kim DH, Wirtz D. Focal adhesion size uniquely predicts cell migration. *FASEB Journal*. 2013;27(4):1351-1361. doi:10.1096/fj.12-220160
171. Besser A, Safran SA. Force-induced adsorption and anisotropic growth of focal adhesions. *Biophysical Journal*. 2006;90(10):3469-3484. doi:10.1529/biophysj.105.074377
172. Geiger B, Spatz JP, Bershadsky AD. Extracellular matrix Environmental sensing through focal adhesions. Published online 2009. doi:10.1038/nrm2593
173. Kuo J-C. Focal Adhesions Function as a Mechanosensor. *Progress in Molecular Biology and Translational Science*. 2014;126:55-73. doi:10.1016/B978-0-12-394624-9.00003-8
174. di Cio S, Gautrot JE. Cell sensing of physical properties at the nanoscale: Mechanisms and control of cell adhesion and phenotype. *Acta Biomaterialia*. 2016;30:26-48. doi:10.1016/J.ACTBIO.2015.11.027
175. Dubrovskiy O, Tian X, Poroyko V, Yakubov B, Birukova AA, Birukov KG. Identification of paxilin domains interacting with  $\beta$ -catenin. 2013;586(16):2294-2299. doi:10.1016/j.febslet.2012.06.016.Identification
176. Marie PJ, Hay E, Modrowski D, Revollo L, Mbalaviele G, Civitelli R. Cadherin-mediated cell-cell adhesion and signaling in the skeleton. *Calcified tissue international*. 2014;94(1):46-54. doi:10.1007/s00223-013-9733-7
177. Tarkkonen K, Hieta R, Kytölä V, Nykter M, Kiviranta R. Comparative analysis of osteoblast gene expression profiles and Runx2 genomic occupancy of mouse and human osteoblasts in vitro. *Gene*. 2017;626:119-131. doi:10.1016/j.gene.2017.05.028
178. Gupta A, Chatree S, Buo AM, Moorer MC, Stains JP. Connexin43 enhances Wnt and PGE2-dependent activation of  $\beta$ -catenin in osteoblasts. *Pflugers Archiv European Journal of Physiology*. 2019;471(9):1235-1243. doi:10.1007/s00424-019-02295-y
179. Yan M, Li G, An J. Discovery of small molecule inhibitors of the Wnt/ $\beta$ -catenin signaling pathway by targeting  $\beta$ -catenin/Tcf4 interactions. *Experimental Biology and Medicine*. 2017;242(11):1185-1197. doi:10.1177/1535370217708198
180. Leung JY, Kolligs FT, Wu R, et al. Activation of AXIN2 expression by  $\beta$ -catenin-T cell factor: A feedback repressor pathway regulating Wnt signaling. *Journal of Biological Chemistry*. 2002;277(24):21657-21665. doi:10.1074/jbc.M200139200
181. Li Z, Xu Z, Duan C, Liu W, Sun J, Han B. Role of TCF/LEF transcription factors in bone development and osteogenesis. *International Journal of Medical Sciences*. 2018;15(12):1415-1422. doi:10.7150/ijms.26741
182. Rao X, Huang X, Zhou Z, Lin X. An improvement of the  $2^{-\Delta\Delta CT}$  method for quantitative real-time polymerase chain reaction data analysis. *Biostatistics, bioinformatics and biomathematics*. 2013;3(3):71-85. Accessed May 20, 2020. <http://www.ncbi.nlm.nih.gov/pubmed/25558171>
183. Virtanen P, Isotupa K. Staining properties of alizarin red S for growing bone in vitro. *Cells Tissues Organs*. 1980;108(2):202-207. doi:10.1159/000145301
184. Biggs MJPP, Dalby MJ. Focal adhesions in osteoneogenesis. In: *Proceedings of the Institution of Mechanical Engineers, Part H: Journal of Engineering in Medicine*. Vol 224. ; 2010:1441-1453. doi:10.1243/09544119JEIM775

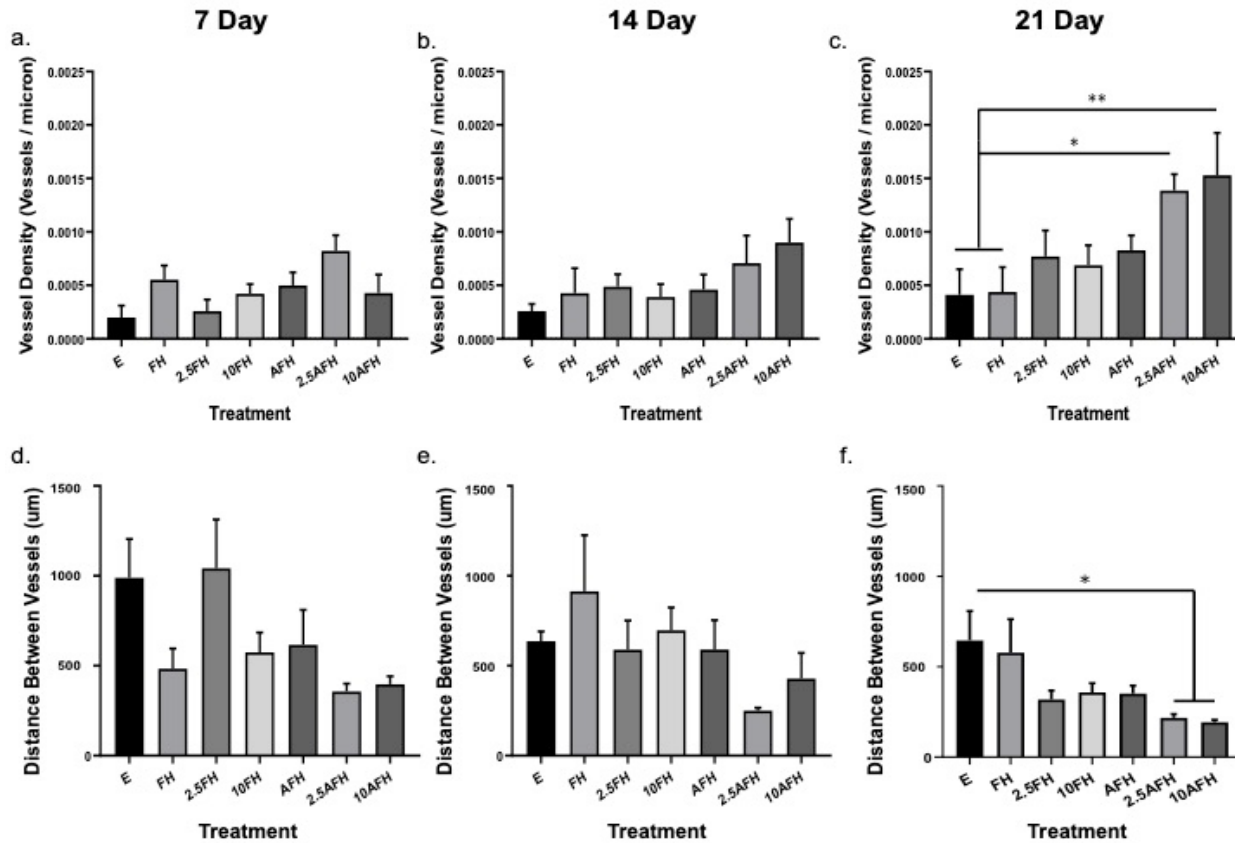
185. Lim J, Taylor AF, Vogler EA, Donahue HJ. Integrin Expression and Osteopontin Regulation in Human Fetal Osteoblastic Cells Mediated by Substratum Surface Characteristics. *Tissue Engineering*. 2005;11(12). Accessed July 20, 2017. <http://online.liebertpub.com/doi/pdf/10.1089/ten.2005.11.19>
186. Lim J, Dreiss AD, Zhou Z, et al. The regulation of integrin-mediated osteoblast focal adhesion and focal adhesion kinase expression by nanoscale topography. *Biomaterials*. 2007;28:1787-1797. doi:10.1016/j.biomaterials.2006.12.020
187. Galli C, Piemontese M, Lumetti S, Ravanetti F, Macaluso GMM, Passeri G. Actin cytoskeleton controls activation of Wnt/ $\beta$ -catenin signaling in mesenchymal cells on implant surfaces with different topographies. *Acta Biomaterialia*. 2012;8(8):2963-2968. doi:10.1016/J.ACTBIO.2012.04.043
188. Kale GR, Yang X, Philippe JM, Mani M, Lenne PF, Lecuit T. Distinct contributions of tensile and shear stress on E-cadherin levels during morphogenesis. *Nature Communications*. 2018;9(1). doi:10.1038/s41467-018-07448-8
189. Birukova AA, Malyukova I, Poroyko V, Birukov KG. Paxillin- $\beta$ -catenin interactions are involved in Rac/Cdc42-mediated endothelial barrier-protective response to oxidized phospholipids. *American Journal of Physiology - Lung Cellular and Molecular Physiology*. 2007;293(1). doi:10.1152/ajplung.00020.2007
190. Mackay DJG, Esch F, Furthmayr H, Hall A. Rho- and Rac-dependent assembly of focal adhesion complexes and actin filaments in permeabilized fibroblasts: An essential role for ezrin/radixin/moesin proteins. *Journal of Cell Biology*. 1997;138(4):927-938. doi:10.1083/jcb.138.4.927
191. Spiering D, Hodgson L. Dynamics of the Rho-family small GTPases in actin regulation and motility. *Cell adhesion & migration*. 2011;5(2):170-180. doi:10.4161/CAM.5.2.14403
192. Case N, Thomas J, Sen B, et al. Mechanical Regulation of Glycogen Synthase Kinase 3 (GSK3) in Mesenchymal Stem Cells Is Dependent on Akt Protein Serine 473 Phosphorylation via mTORC2 Protein \*. *THE JOURNAL OF BIOLOGICAL CHEMISTRY*. 2011;286(45):39450-39456. doi:10.1074/jbc.M111.265330
193. Thompson WR, Guilluy C, Xie Z, et al. Mechanically activated fyn utilizes mTORC2 to regulate RhoA and adipogenesis in mesenchymal stem cells. *STEM CELLS*. 2013;31(11):2528-2537. doi:10.1002/stem.1476
194. Rutkovskiy A, Stenslkken K-O, Vaage IJ. Osteoblast Differentiation at a Glance. *Medical Science Monitor Basic Research*. 2016;22:95-106. doi:10.12659/msmbr.901142
195. Prowse PDH, Elliott CG, Hutter J, Hamilton DW. Inhibition of Rac and ROCK signalling influence osteoblast adhesion, differentiation and mineralization on titanium topographies. *PloS one*. 2013;8(3):e58898. doi:10.1371/journal.pone.0058898
196. Schweikl Rainer Mller AE Carsten Englert AE Karl-Anton Hiller AE Richard Kujat AE Michael Nerlich AE Gottfried Schmalz HA. Proliferation of osteoblasts and fibroblasts on model surfaces of varying roughness and surface chemistry. Published online 2007. doi:10.1007/s10856-007-3092-8
197. Bidwell JP, Pavalko FM. Mechanosomes Carry a Loaded Message. *Science Signaling*. 2010;3(153):51-1. Accessed May 7, 2018. <http://stke.sciencemag.org/content/sigtrans/3/153/pe51.full.pdf>

198. Duan P, Bonewald LF. The role of the wnt/ $\beta$ -catenin signaling pathway in formation and maintenance of bone and teeth. *International Journal of Biochemistry and Cell Biology*. 2016;77:23-29. doi:10.1016/j.biocel.2016.05.015
199. Case N, Ma M, Sen B, Xie Z, Gross TS, Rubin J.  $\beta$ -Catenin levels influence rapid mechanical responses in osteoblasts. *Journal of Biological Chemistry*. 2008;283(43):29196-29205. doi:10.1074/jbc.M801907200
200. Castillo AB, Blundo JT, Chen JC, et al. Focal Adhesion Kinase Plays a Role in Osteoblast Mechanotransduction In Vitro but Does Not Affect Load-Induced Bone Formation In Vivo. *PLoS ONE*. 2012;7(9). doi:10.1371/journal.pone.0043291
201. Wörthmüller J, Rüegg C. The crosstalk between FAK and Wnt signaling pathways in cancer and its therapeutic implication. *International Journal of Molecular Sciences*. 2020;21(23):1-23. doi:10.3390/ijms21239107
202. Slack-Davis JK, Martin KH, Tilghman RW, et al. Cellular characterization of a novel focal adhesion kinase inhibitor. *Journal of Biological Chemistry*. 2007;282(20):14845-14852. doi:10.1074/jbc.M606695200
203. Grosso A, Burger MG, Lunger A, Schaefer DJ, Banfi A, di Maggio N. It takes two to tango: Coupling of angiogenesis and osteogenesis for bone regeneration. *Frontiers in Bioengineering and Biotechnology*. 2017;5(NOV):68. doi:10.3389/fbioe.2017.00068
204. Hori Y, Kashimoto T, Yonezawa T, et al. Matrix metalloproteinase-2 stimulates collagen-I expression through phosphorylation of focal adhesion kinase in rat cardiac fibroblasts. *American Journal of Physiology-Cell Physiology*. 2012;303(9):C947-C953. doi:10.1152/ajpcell.00401.2011
205. Kam Y, Quaranta V. Cadherin-bound  $\beta$ -catenin feeds into the Wnt pathway upon adherens junctions dissociation: Evidence for an intersection between  $\beta$ -catenin pools. *PLoS ONE*. 2009;4(2). doi:10.1371/journal.pone.0004580
206. Zhao X, Guan JL. Focal adhesion kinase and its signaling pathways in cell migration and angiogenesis. *Advanced Drug Delivery Reviews*. 2011;63(8):610-615. doi:10.1016/j.addr.2010.11.001
207. Sen B, Xie Z, Case N, et al. mTORC2 Regulates Mechanically Induced Cytoskeletal Reorganization and Lineage Selection in Marrow-Derived Mesenchymal Stem Cells. *Journal of Bone and Mineral Research*. 2014;29(1):78-89. doi:10.1002/jbmr.2031
208. Carles-Carner M, Saleh LS, Bryant SJ. The effects of hydroxyapatite nanoparticles embedded in a MMP-sensitive photoclickable PEG hydrogel on encapsulated MC3T3-E1 pre-osteoblasts. *Biomedical Materials (Bristol)*. 2018;13(4):045009. doi:10.1088/1748-605X/aabb31
209. Dhivya S, Saravanan S, Sastry TP, Selvamurugan N. Nanohydroxyapatite-reinforced chitosan composite hydrogel for bone tissue repair in vitro and in vivo. *Journal of Nanobiotechnology*. 2015;13(1):40. doi:10.1186/s12951-015-0099-z
210. Uswatta SP, Okeke IU, Jayasuriya AC. Injectable porous nanohydroxyapatite/chitosan/tripolyphosphate scaffolds with improved compressive strength for bone regeneration. *Materials Science and Engineering C*. 2016;69:505-512. doi:10.1016/j.msec.2016.06.089

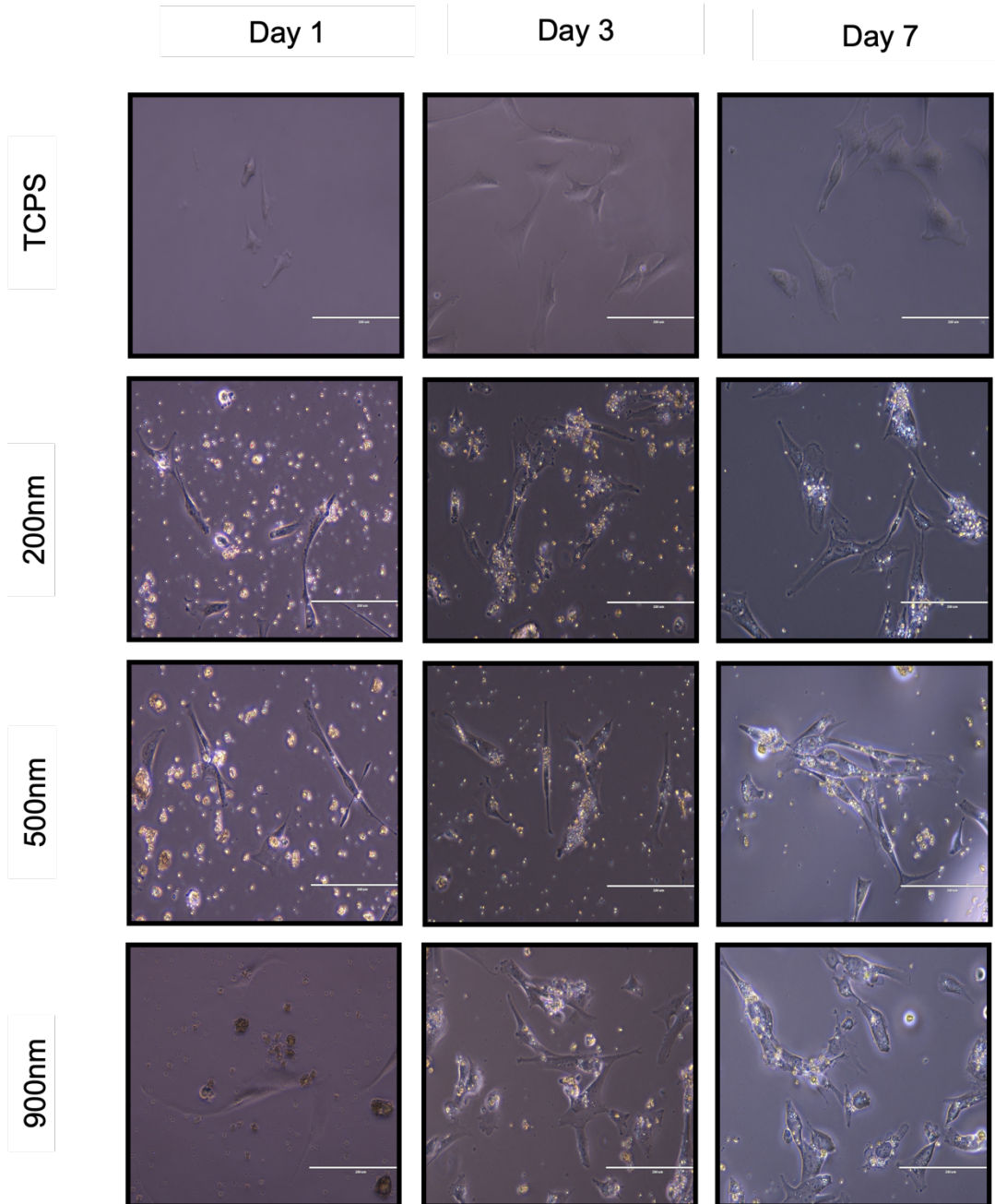
211. Kramps T, Peter O, Brunner E, et al. Wnt/Wingless signaling requires BCL9/legless-mediated recruitment of pygopus to the nuclear  $\beta$ -catenin-TCF complex. *Cell*. 2002;109(1):47-60. doi:10.1016/S0092-8674(02)00679-7
212. Gottardi CJ, Gumbiner BM. Distinct molecular forms of  $\beta$ -catenin are targeted to adhesive or transcriptional complexes. *Journal of Cell Biology*. 2004;167(2):339-349. doi:10.1083/jcb.200402153
213. Hartsock A, Nelson WJ. Adherens and tight junctions: structure, function and connections to the actin cytoskeleton. *Biochimica et biophysica acta*. 2008;1778(3):660-669. doi:10.1016/j.bbamem.2007.07.012
214. Sekar RB, Periasamy A. Fluorescence resonance energy transfer (FRET) microscopy imaging of live cell protein localizations. *Journal of Cell Biology*. 2003;160(5):629-633. doi:10.1083/jcb.200210140

# APPENDIX

## SUPPLEMENTAL INFORMATION

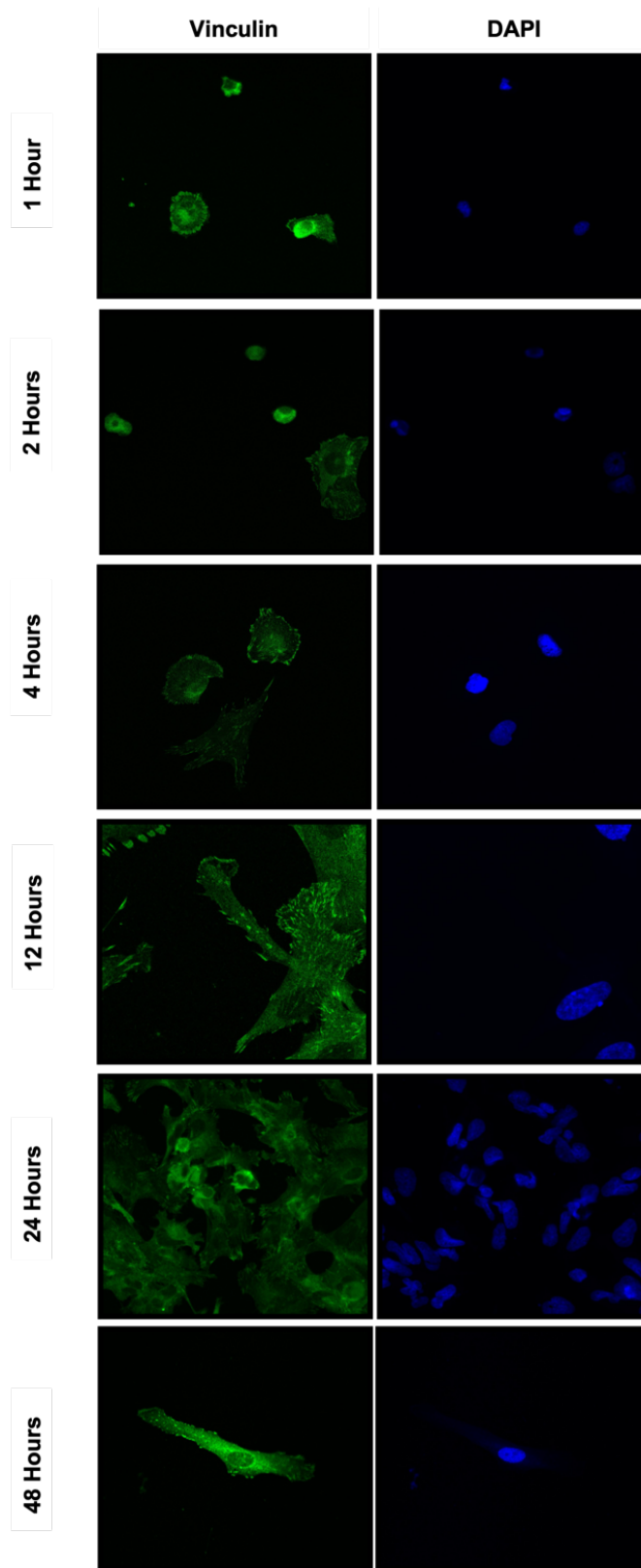


**Supplemental Figure S1.** Angiogenic evaluation of vessel density and spacing as a result of hydrogel treatment. (a,d) MicroCT analysis of vascular density (vessels/ micron) and vascular separation (micron) of the defect at 7 days post defect introduction for all intervention types (b,e) 14 days post defect introduction for all intervention types (c,f) 21 days post defect introduction for all intervention types. \* p < 0.05, \*\* p < 0.005, n ≥ 3



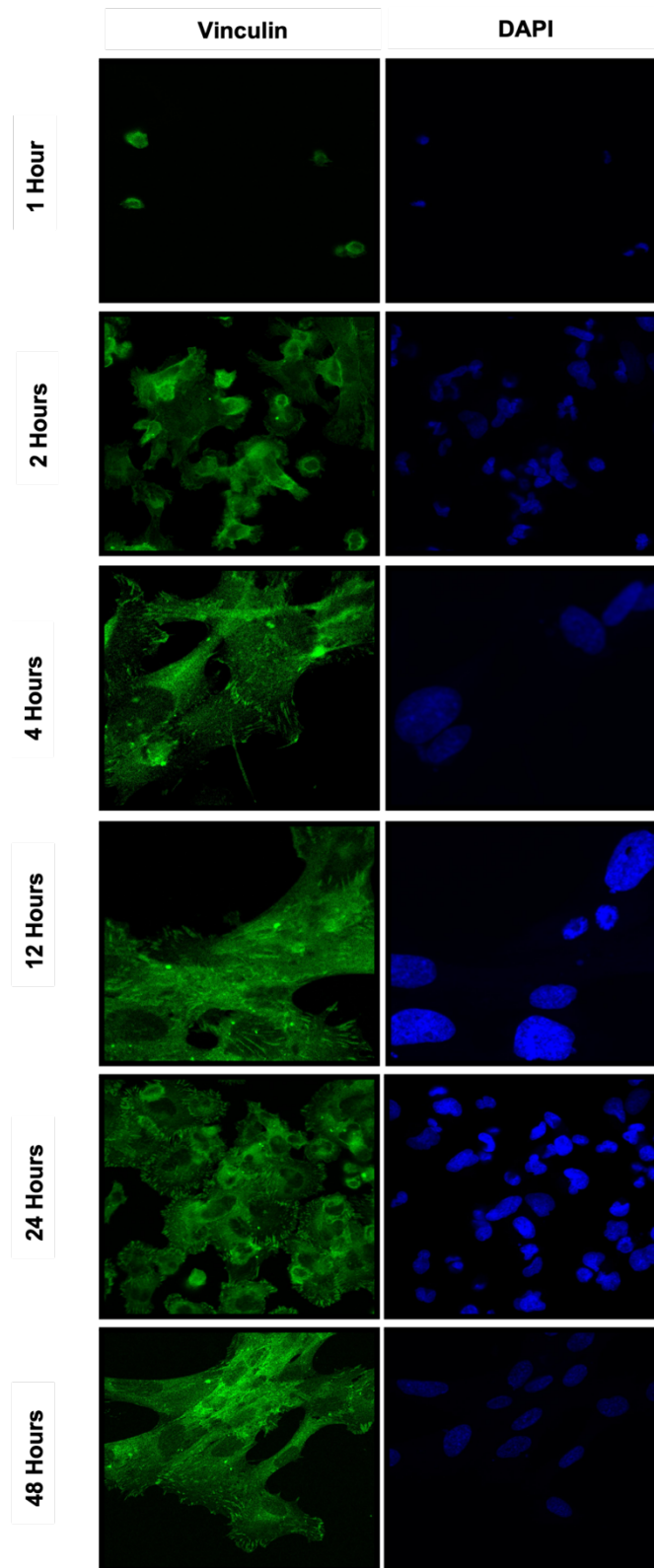
**Supplemental Figure S2.** Representative images of osteoblast cell morphology at 1, 3, and 7 days in response to various CHA particle sizes (200nm, 500nm, and 900nm) examined. No significant changes were observed in osteoblast morphology over time regardless of CHA particle size examined. With cells exhibiting a more dendritic morphology at earlier time points and becoming more cuboidal over time.

Glass Substrate



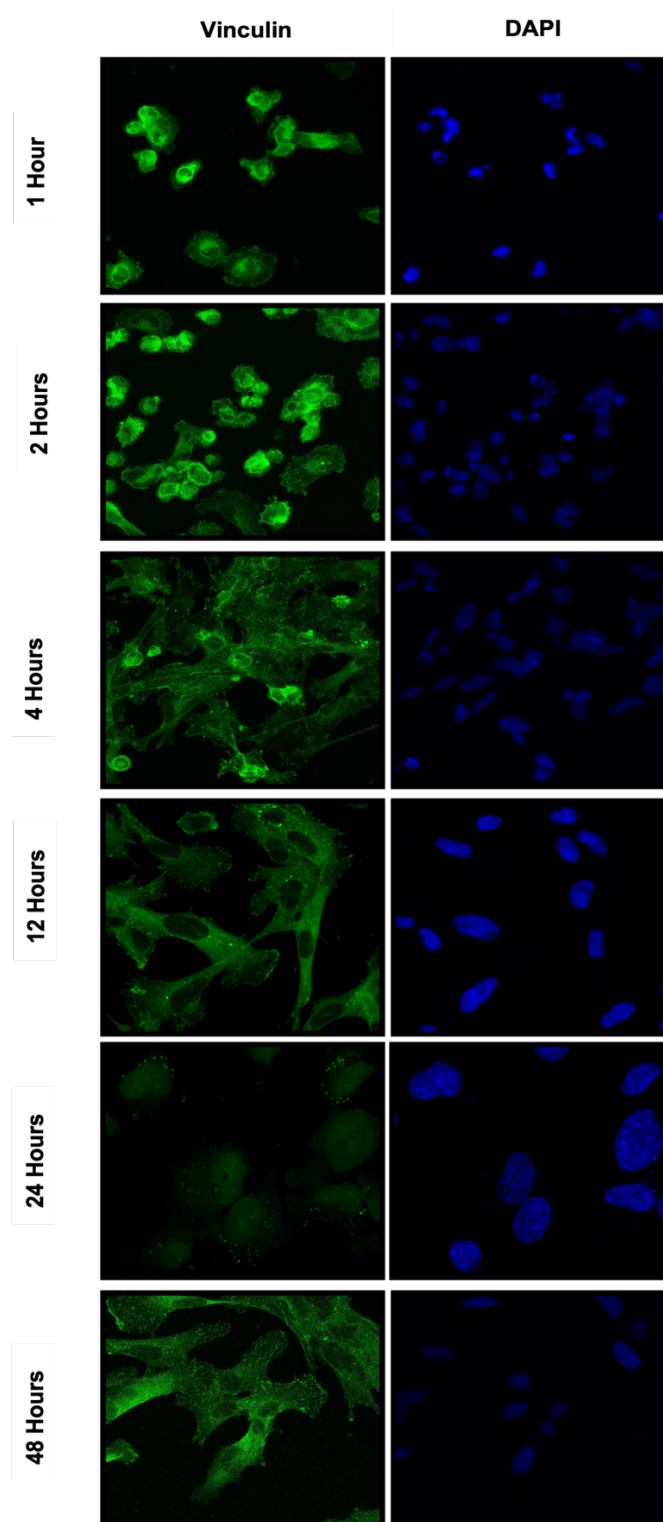


PCL Substrate

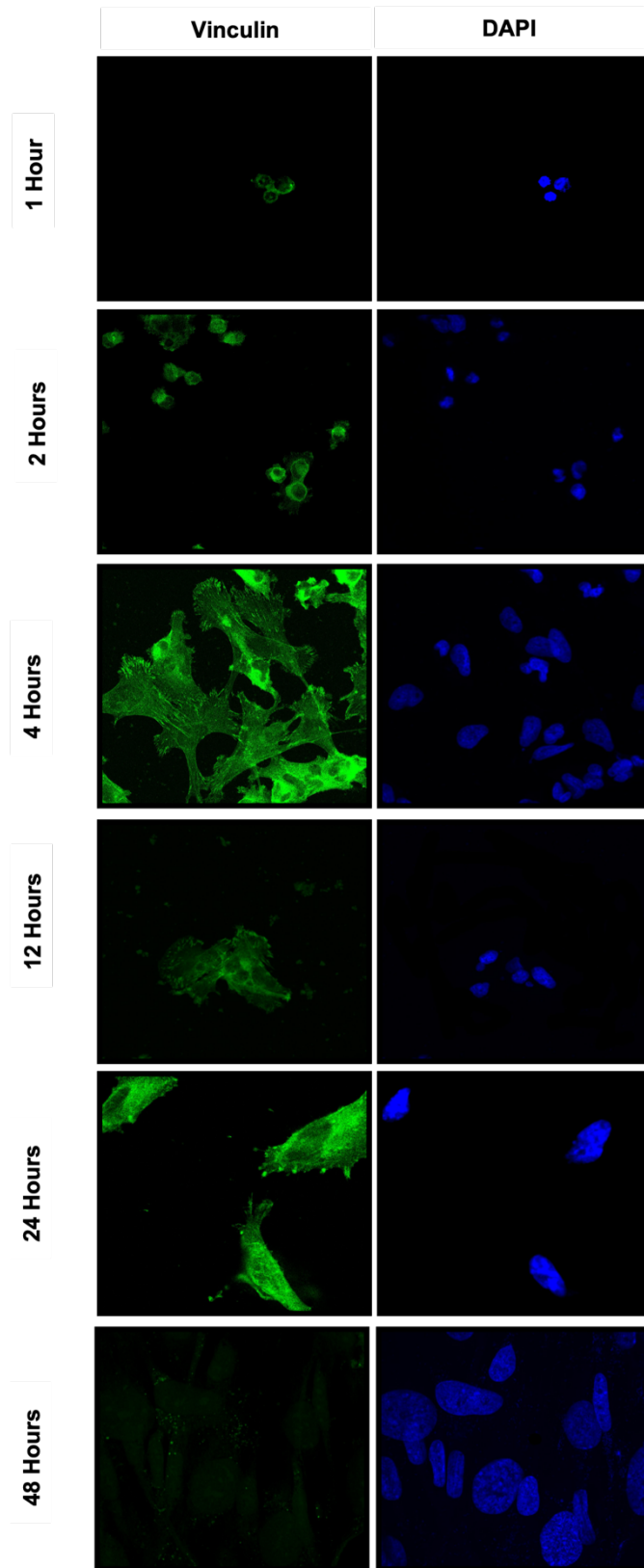




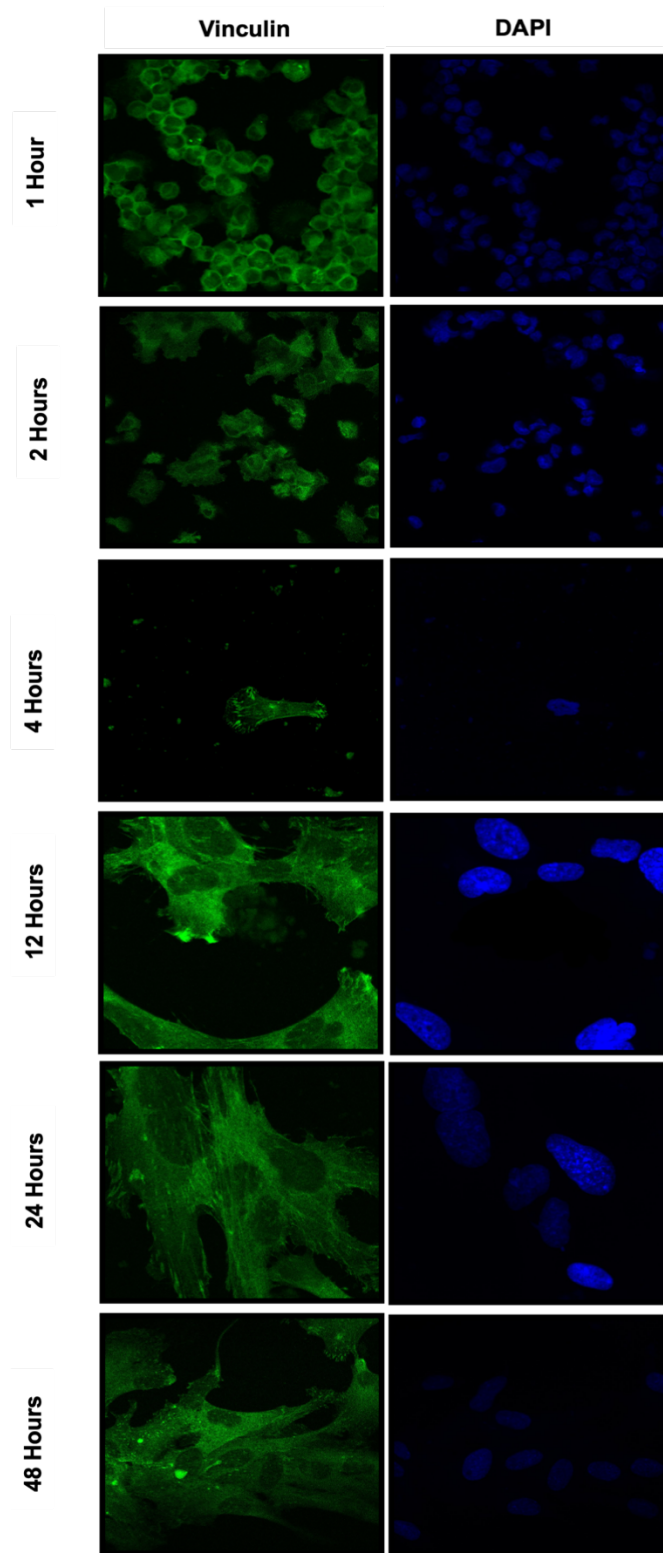
5% HA/PCL Substrate



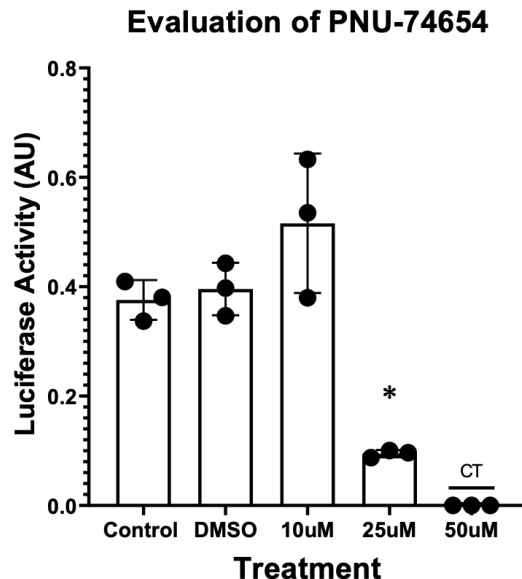
30% HA/PCL Substrate



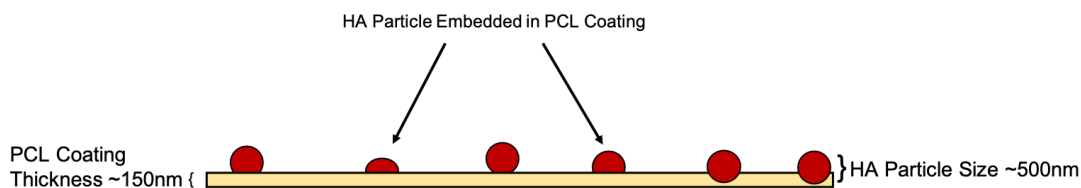
50% HA/PCL Substrate



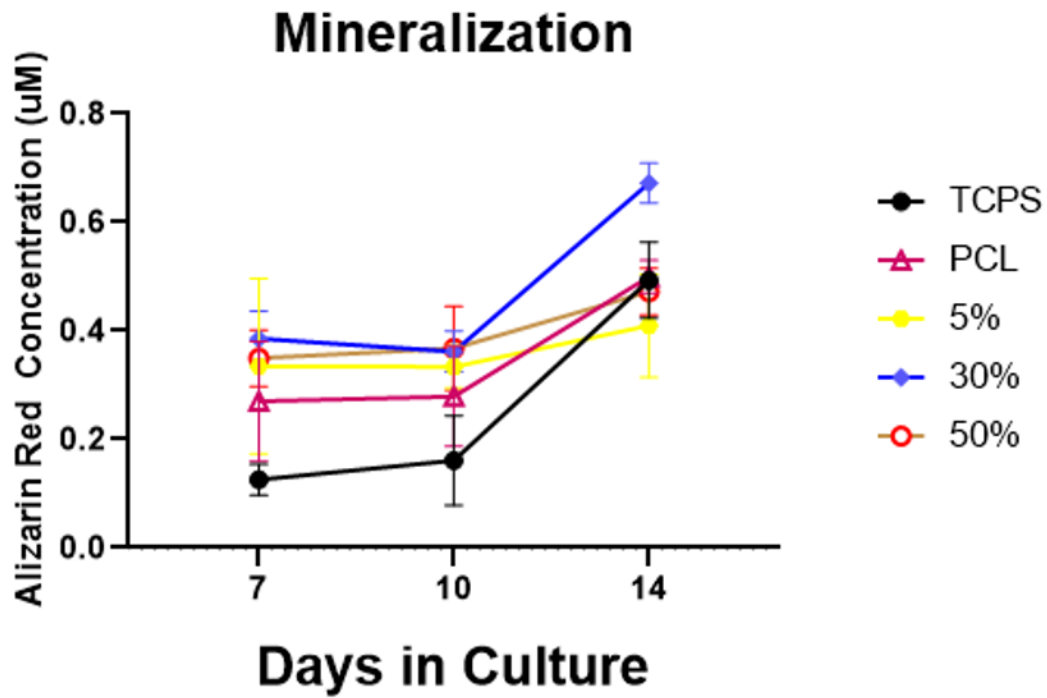
**Supplemental Figure S3.** Fluorescent staining of focal adhesion complexes (Vinculin) and the nucleus (DAPI) in cells cultured on Glass, PCL, 5%, 30% or 50% substrates over 48 hours.



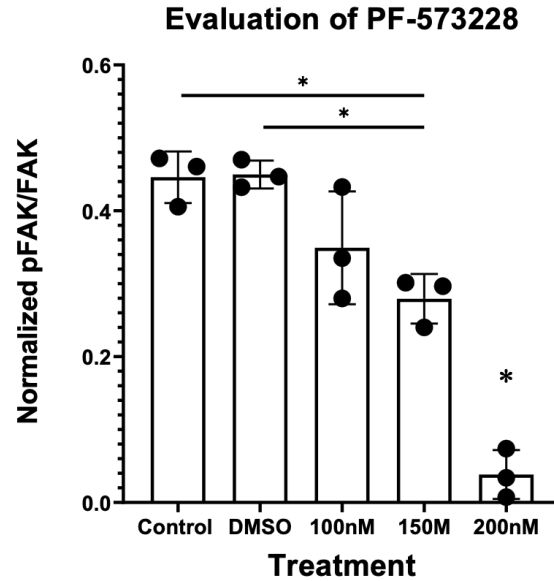
**Supplemental Figure S4.** Evaluation of the effect of PNU-74654, an inhibitor of  $\beta$ -catenin binding to TCF/LEF, on  $\beta$ -catenin nuclear activity in hFOB 1.19 cells 48 hours after the addition of the inhibitor. Inhibitor was evaluated at 10  $\mu$ M, 25  $\mu$ M, and 50 $\mu$ M with an untreated group (Control) and a group supplemented with an identical volume of DMSO (DMSO) serving as controls. Significance is considered  $p < 0.05$ , \* = significantly different than all other groups. CT = cytotoxic concentration resulting in cell death.  $n=3$  samples with each sample being the average of two replicates.



**Supplemental Figure S5.** Schematic illustration of the PCL and HAp substrate with 150nm thick PCL coating indicated at left and 500nm HA particles shown in red indicated at right.

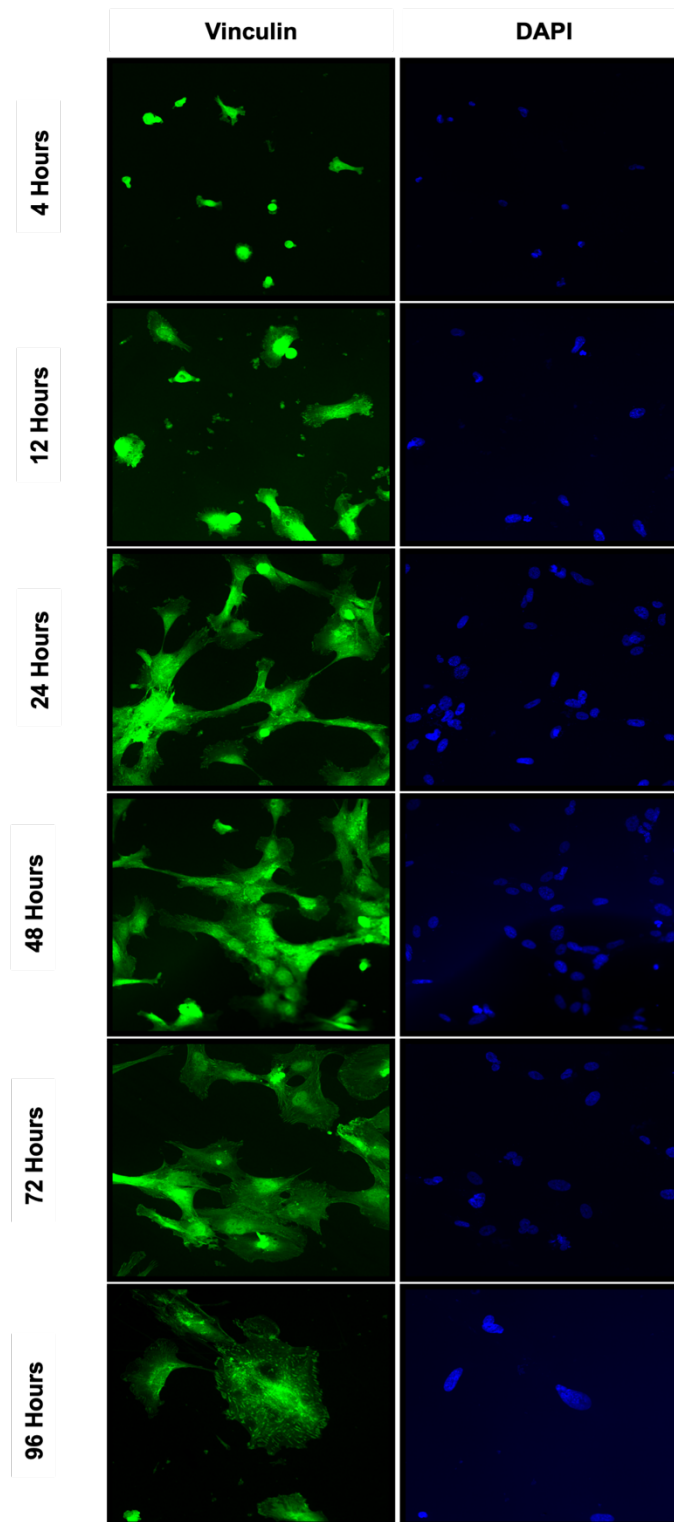


**Supplemental Figure S6.** Evaluation of mineralization in hFOB 1.19 cells in hFOB1.19 cells cultured on TCPS, PCL, 5%, 30%, and 50% HAp/PCL substrates for 7, 10 and 14 days. Significance is considered  $p < 0.05$ , \* = significantly different than all other groups.  $n=4$  samples.

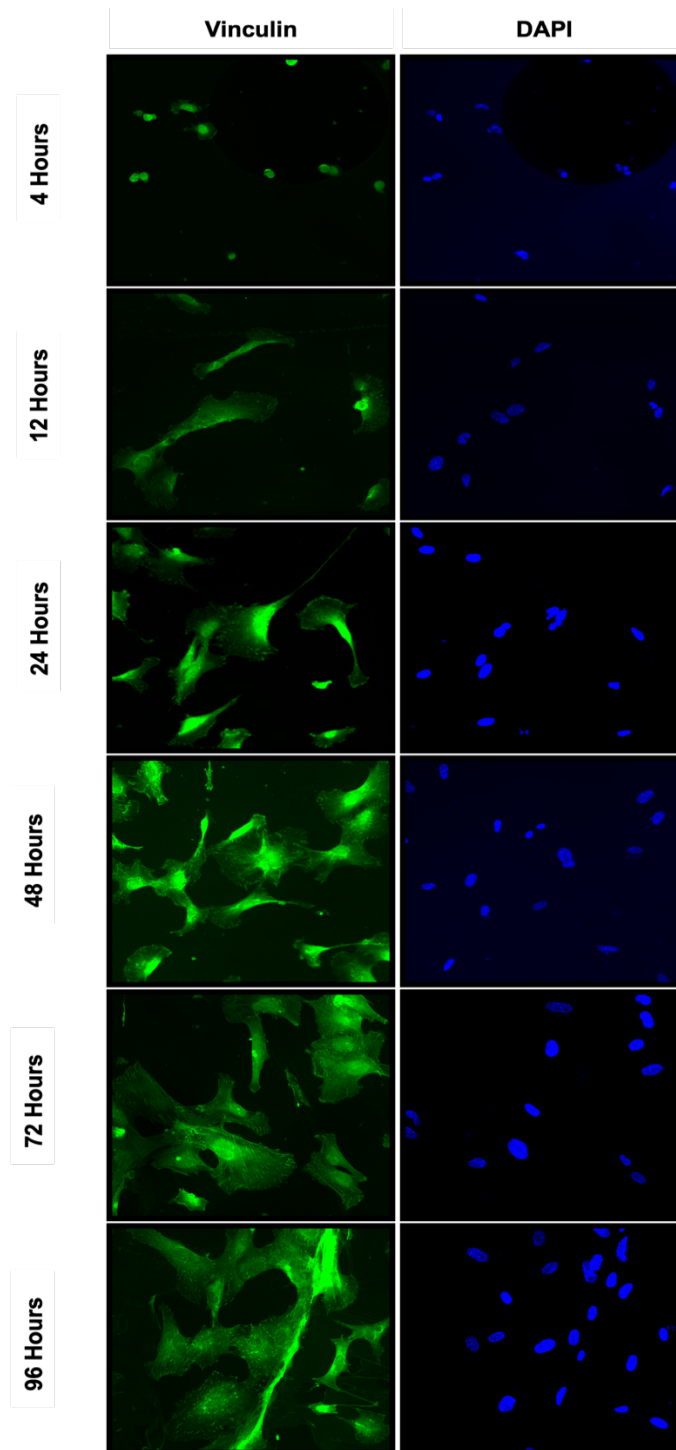


**Supplemental Figure S7.** Evaluation of the effect of PF-573228, an inhibitor of focal adhesion kinase, on normalized focal adhesion phosphorylation (phosphorylated/total) in hFOB 1.19 cells 48 hours after the addition of the inhibitor. Inhibitor was evaluated at 100nm, 150nm, and 200nM with an untreated group (Control) and a group supplemented with an identical volume of DMSO (DMSO) serving as controls. Significance is considered  $p < 0.05$ , \* = significantly different than all other groups \*. n=3 samples with each sample being the average of two replicates.

SUBSTRATE IN THE ABSENCE OF FAK INHIBITOR

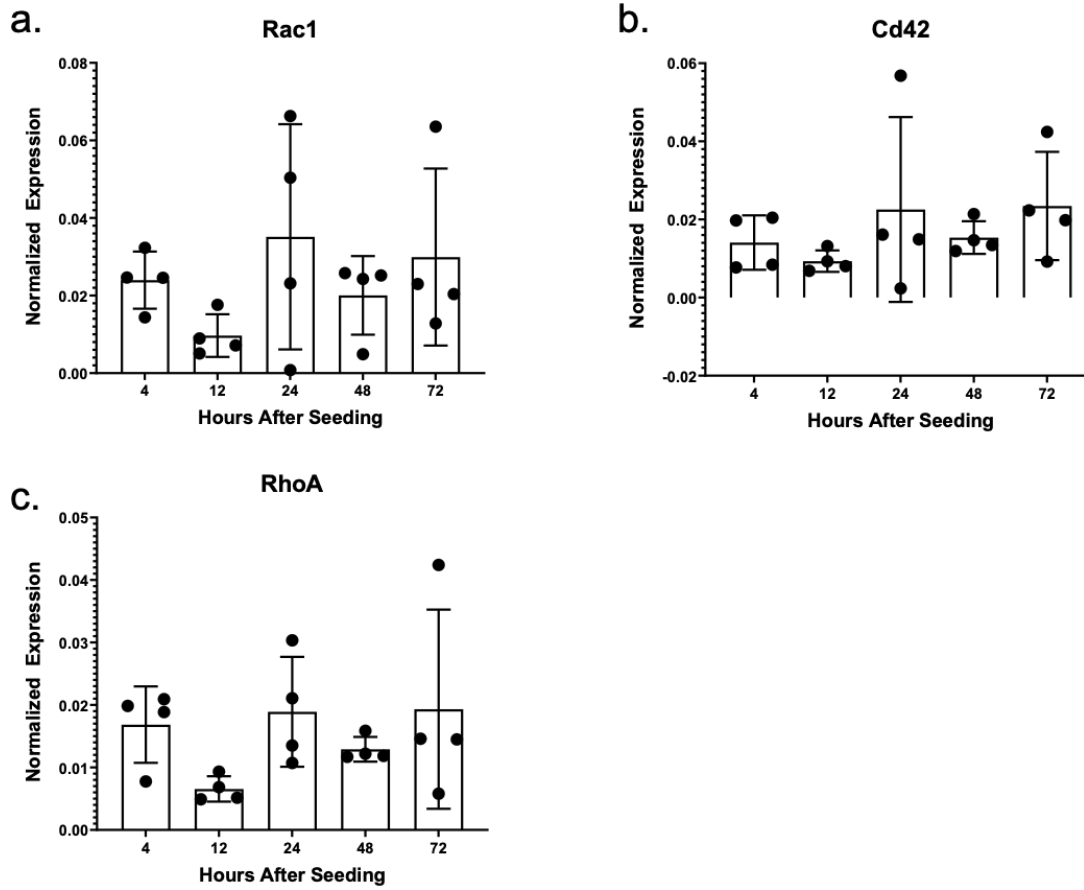


SUBSTRATE IN THE PRESENCE OF FAK INHIBITOR



**Supplemental Figure S8.** Fluorescent staining of focal adhesion complexes (vinculin) and the nucleus (DAPI) in cells cultured on pro-osteogenic substrate in the presence or absence of FAK inhibitor over 96 hours.





**Supplemental Figure S9.** Evaluation of GTPases (a) Rac1, (b) Cd42, and (c) RhoA in hFOB1.19 cells cultured on POS after 4 hours, 12 hours, 24 hours, 48 hours and 72 hours in culture. Significance is considered  $p < 0.05$ .  $n=4$  samples.